RHEOLOGICAL IMPLICATIONS OF TENSION IN LIQUIDS

A Dissertation
Presented to
The Academic Faculty

By

Peter A. Kottke

In Partial Fulfillment
Of the Requirements for the Degree
Doctor of Philosophy in Mechanical Engineering

Georgia Institute of Technology
June 2004

RHEOLOGICAL IMPLICATIONS OF TENSION IN LIQUIDS

Approved By:

Dr. Ward Winer, Adviser

Dr. Jonathan Colton

Dr. Sue Ann Bidstrup Allen

Dr. Karl Jacob

Dr. Scott Bair

Date Approved: 28 June. 2004

ACKNOWLEDGMENTS

I appreciate the great opportunity that being a graduate student in the G.W.W. School of Mechanical Engineering at Georgia Tech has been, and I am grateful for the sacrifices of my family while I have been here.

I am specifically grateful to my wife, Maggie, and our children, Jackson and Charlotte, for being great sports, and to our parents for their encouragement and support.

I would like to thank my adviser, Dr. Ward Winer, for giving me the freedom and backing to learn how to think and research, and my co-adviser, Dr. Scott Bair, for his tremendous input and for his friendship. I want to offer my gratitude to my other reading committee members, Dr. Jonathan Colton, Dr. Sue Ann Bidstrup Allen, and Dr. Karl Jacob, for their time and thoughts.

Many members of the Tech staff have helped me during the past four years. In particular, Verna Phillips, Melody Foster, the M.E. Machine Shop (John Graham and Donald Long) and the M.E. Electronics Shop (John Weitzel, Vladamir Bortkevich and Drew Davis) have been tremendous.

Many of the faculty have been great teachers to me. A few I really want to thank are Bill Wepfer, Jim Hartley, Andrei Fedorov, and Prateen Desai.

Several of my fellow students were important to my time here. I hope for continued future conversations and friendships with Beth Douglas, Vladimir Novak, and Tim Ferguson.

Financial support from a National Defense Science and Engineering Graduate Fellowship, an Achievement Rewards for College Scientists Fellowship, a Georgia

TABLE OF CONTENTS

LIST OF FIGURES

ix

LIST OF TABLES

LIST OF SYMBOLS

A	area
A	matrix for solution of linear system of equations
a	Carreau-Yasuda parameter
B	extrudate swell
BEM	Boundary Element Method
c	molar concentration
$C(t)$	Bernoulli equation "constant"
C_B	arclength of contact line
Ca_L	capillary number $\mu U/\gamma$
Ca_{CL}	contact line capillary number $\mu u_{CL}/\gamma$
Ci	cavitation index based on viscous stress
D	diffusivity, or, diameter of capillary tube
d	distance from one wall to the other normalized by the initial bubble radius
$\mathbf{f}, f_i$	traction vector
G	modulus, μ/λ
$\mathbf{G}, G_{ij}$	Unbounded Stokes flow Green's function
h	height bubble extends above wall
H	Henry's constant
$\mathcal{H}^{-1}$	inverse Hoffman function
K	shift factor or calibration factor
k	thermal conductivity, or, capillary number based on bubble radius

L	distance, either parallel walls or length of capillary
M	molecular weight
n	viscosity power law index
$\mathbf{n}$, n_i	inward pointing normal vector
$\overline{n}''$	average molar flux
N	number of moles (or moles per unit depth)
N_i	normal stress difference
Na	Nahme number
p	polygonal arclength
p	pressure
p_v	vapor pressure
PB	polybutene
Pe_L	Peclet number
PDMS	polydimethylsioxane
PNSCC	principal normal stress cavitation criterion
Q	volumetric flow rate
R	radius
R_u	universal gas constant, 8.314 J/mol K
Re_L	Reynolds number
s	arclength
S_B	length of boundary for mass transfer
t	time

T	temperature
$\mathbf{T}$, T_{ij}	stress tensor
T_{ijk}	stress associated with G_{ij}
U	boundary velocity
$\mathbf{u}$, u_i	fluid velocity
$\mathbf{u}_{\text{CL}}$	contact line velocity
u_{max}	maximum tangential velocity on bubble surface
V	volume
v	specific volume
W	crevice width
Wi	Weisenberg number
z	constant of proportionality

Greek Symbols

α	pressure viscosity coefficient
β	temperature coefficient of viscosity
δ_c	scale of concentration boundary layer thickness
$\partial\Omega_A$	boundary of liquid domain
$\partial\Omega_{AB}$	interface between liquid and gas domains
$\partial^2\Omega_{AB}$	contact line
γ	surface tension
$\dot{\gamma}$	shear rate
κ	curvature

η	generalized or apparent dynamic viscosity
λ	characteristic relaxation timee
μ	Newtonian or low shear dynamic viscosity
ν	kinematic viscosity
Π	generic non-dimensional parameter
θ	contact angle
θ_{CL}	angle between left (rear) crevice wall and vertical
θ_{CR}	angle between right (leading) crevice wall and vertical
ρ	density
σ_i	principal normal stress
σ_c	critical stress for PNSCC
τ	shear stress throughout simple shear
τ_{app}	apparent shear stress
τ_{ij}	component of the deviatoric stress tensor
τ_w	shear stress at a wall
Ω_A	liquid domain
Ω_b	gas domain
Ψ_t	Normal stress difference coefficient

Subscripts

A	advancing
act	actual
app	apparent

B	bubble
c	correction
G	gas
L	liquid
m	mean
N	Newtonian
n	normal
o	initial or denotes collocation point
R	receding
s	scale
S	solid
t	tangential, or, transducer
w	wall
∞	far field condition or property

Superscripts

C	scaled using Crowdy's scales (Crowdy 2003)
e	elastic
*	dimensional

SUMMARY

This research investigates effects of tensile stresses in liquids. Specific areas of application include bearing lubrication and polymer processing, in which liquids may be subjected to hydrostatic tension, or in which large shear stresses are generated.

The primary thrust of this research concerns the development of a criterion for liquid failure, or cavitation, based upon the general state of stress in the liquid. A variable pressure, rotating inner cylinder, Couette viscometer has been designed and used to test a hypothesized cavitation criterion. The criterion, that cavitation will occur when a principal normal stress in a liquid becomes more tensile than some critical stress, is supported by the results of experiments with the viscometer for a Newtonian liquid. Based upon experimental observation of cavitation, a model for cavitation inception from crevice stabilized gas nuclei, and gaseous, as opposed to vaporous, cavitation is hypothesized.

The cavitation inception model is investigated through numerical simulation, primarily using the boundary element method. Only Newtonian liquids are modeled, and, for simulation purposes, the model is reduced to two dimensions and the limit of negligible inertia (Stokes flow) is considered. The model includes contact line dynamics. Mass transport of dissolved gas through the liquid and in or out of the gas nucleus is considered. The numerical simulations provide important information about the probable nature of cavitation nucleation sites as well as conditions for cavitation inception.

There are several implications of shear cavitation on rheological measurements. It can cause apparent shear thinning and thixotropy. Additionally, there is evidence suggesting a possible link between shear cavitation and extrusion defects such as

sharkskin. A variable pressure capillary tube viscometer was designed and constructed to investigate a hypothesized relationship between shear cavitation and extrusion defects. Results indicate that despite the occasional coincidence of occurrence of cavitation and sharkskin defects, cavitation can not explain the onset of extrusion defects.

If nuclei are removed, then liquids can withstand tension, which, if uniform, is a negative hydrostatic pressure. A falling body viscometer has been constructed which is used to investigate the effect of negative pressures on viscosity. It is found that current pressure viscosity models can be accurately extrapolated to experimentally achievable negative pressures.

CHAPTER 1

INTRODUCTION

This work is concerned with several aspects of the ability of liquids to withstand tensile stresses. The primary concern is the investigation of a hypothesis that a liquid will fail when one of its principal normal stresses becomes sufficiently tensile. This hypothesis leads to a principal normal stress cavitation criterion, PNSCC, which predicts cavitation in simple shear flows that are often used to obtain rheological data. Such shear cavitation would invalidate the assumption of a viscometric flow and be a major source of experimental error.   This investigation into the PNSCC is both experimental and theoretical. It shows that while the PNSCC is a good predictor of shear cavitation in Newtonian liquids, it implies a degree of simplicity about the cavitation phenomenon that is misleading.

1.1   TENSION IN LIQUIDS

The state of stress in a liquid is described by a stress tensor, **T.**   For an incompressible liquid this tensor can be split into two parts, a pressure component, **p** and a deviatoric component, $\boldsymbol{\tau}$, which is the component that leads to deformation and flow of the liquid. In a Cartesian coordinate system this leads to the following stress tensor

$$\mathbf{T} = \begin{bmatrix} \tau_{xx} - p & \tau_{xy} & \tau_{xz} \\ \tau_{xy} & \tau_{yy} - p & \tau_{yz} \\ \tau_{xz} & \tau_{yz} & \tau_{zz} - p \end{bmatrix}. \tag{1.1}$$

A tensile stress exists in the liquid whenever one or more of the principal stresses becomes positive. The principal stresses, σ_1, σ_2, and σ_3, are the eigenvalues of **T**, and satisfy

$$\det\left(\mathbf{T} - \sigma\mathbf{I}\right) = 0 \tag{1.2}$$

where $\mathbf{I}$ is the identity tensor.

In simple shear the stress tensor reduces to

$$\mathbf{T} = \begin{bmatrix} \tau_{xx} - p & \tau_{xy} & 0 \\ \tau_{xy} & \tau_{yy} - p & 0 \\ 0 & 0 & \tau_{zz} - p \end{bmatrix}. \tag{1.3}$$

In simple shear the deformation of a liquid can be expressed by a scalar, $\dot{\gamma}$, called the shear rate, and the deviatoric components of the stress tensor are functions of $\dot{\gamma}$ only. The simplest case is that of a Newtonian liquid in which the shear stress and shear rate are related by the Newtonian viscosity, μ,

$$\tau_{xy} = \mu\dot{\gamma}, \tag{1.4}$$

and the normal stress components of the deviatoric are zero (Bird *et al.* 1987). In simple shear of a Newtonian liquid, the subscripts on the shear stress can be dropped. Thus, in the case of simple shear of a Newtonian liquid, the principal stresses are as follows:

$$\begin{aligned} \sigma_1 &= -p + \tau, \\ \sigma_2 &= -p \qquad \text{and} \\ \sigma_3 &= -p - \tau, \end{aligned} \tag{1.5}$$

where σ_1 is the most tensile of the principal stresses. σ_1 is tensile when

$$\mu\dot{\gamma} > p. \tag{1.6}$$

. In the case of a generalized Newtonian shear thinning liquid, the shear stress and shear rate are related by the non-Newtonian, or generalized, viscosity, $\eta(\dot{\gamma})$,

$$\tau = \eta(\dot{\gamma})\dot{\gamma}, \tag{1.7}$$

and the analysis remains the same as for a Newtonian liquid with μ replaced by $\eta(\dot{\gamma})$.

The situation becomes more complicated in the case of liquids in which simple shear results in normal stress differences,

2

$$N_1 = \tau_{xx} - \tau_{yy} \text{ and}$$
$$N_2 = \tau_{yy} - \tau_{zz}. \tag{1.8}$$

In this case the principal normal stresses depend also upon the boundary conditions for the flow. The PNSCC will be considered in the context of Couette flow. For non-Newtonian liquids, N_2 will be assumed to be negligible, and the pressure at the edge of the flow will be taken to be p. In this case, the application of Eq. (1.2) to find the principal normal stresses yields

$$\sigma_1 = -p + \frac{1}{2}\left(N_1 + \sqrt{N_1^2 + 4\tau_{xy}^2}\right)$$
$$\sigma_2 = -p + \frac{1}{2}\left(N_1 - \sqrt{N_1^2 + 4\tau_{xy}^2}\right) \tag{1.9}$$
$$\sigma_3 = -p - N_2.$$

The most tensile principal stress, σ_1, is tensile when

$$\frac{1}{2}\left(N_1 + \sqrt{N_1^2 + 4\tau_{xy}^2}\right) > p. \tag{1.10}$$

An investigation into the possibility of liquid failure, or cavitation, as a result of the most tensile principal normal stress approaching some critical value is a main thrust of this work.

When a liquid is not flowing, the principal stresses must all be the same and have magnitudes equal to the hydrostatic pressure; for tension to exist the pressure must be negative. An investigation into the rheological effect of tension due to a negative hydrostatic pressure comprises another major thrust of this research.

1.1.a Negative Pressure and Tensile Strength

It has been recognized for centuries that liquids can withstand tensions, which, if uniform, are a negative hydrostatic pressure (Kell 1983). The tensile strength of a liquid is the absolute value of the minimum negative pressure achievable, or, in other words, the

minimum pressure a liquid can withstand before failure. Failure is considered to have occurred when the liquid ceases to withstand tension. The most accepted model for predicting the maximum tensile strength of a liquid was developed by Temperley based on the Van der Waals equation of state (Trevena 1986)

$$\left(p + \frac{a}{v^2} \right)(v - b) = R_u T \qquad (1.11)$$

where a and b are the Van der Waals parameters related to intermolecular attraction and hard shell radius respectively, and v is the specific volume. The absolute value of the minimum of an isotherm of a Van der Waals fluid on a pressure – volume diagram is the theoretical tensile strength of the liquid. To understand how a liquid reaches a state of tension, consider the isotherm in Figure 1. The dotted line is along the saturation pressure for the given temperature. The states represented by the dot/dash portion of the curve between the two extrema are mechanically unstable, and the fluid will not exist at states described by this portion of the curve. The states represented by the bold portions of the curve are mechanically stable, though thermodynamically unstable. The minimum can be at a pressure less than absolute zero, and could be reached by expanding a subcooled liquid at constant temperature. When a liquid is withstanding a negative pressure, it is in a metastable state (Trevena 1986).

1.2   CAVITATION

Cavitation is defined by Young as "the formation and activity of bubbles (or cavities) in a liquid (Young 1999)." The cavity may be created by the cavitation event, or be preexisting in the liquid in some manner, and caused to grow to macroscopic size by the cavitation event. The contents of the cavity may be vapor, gas, or a mixture of the
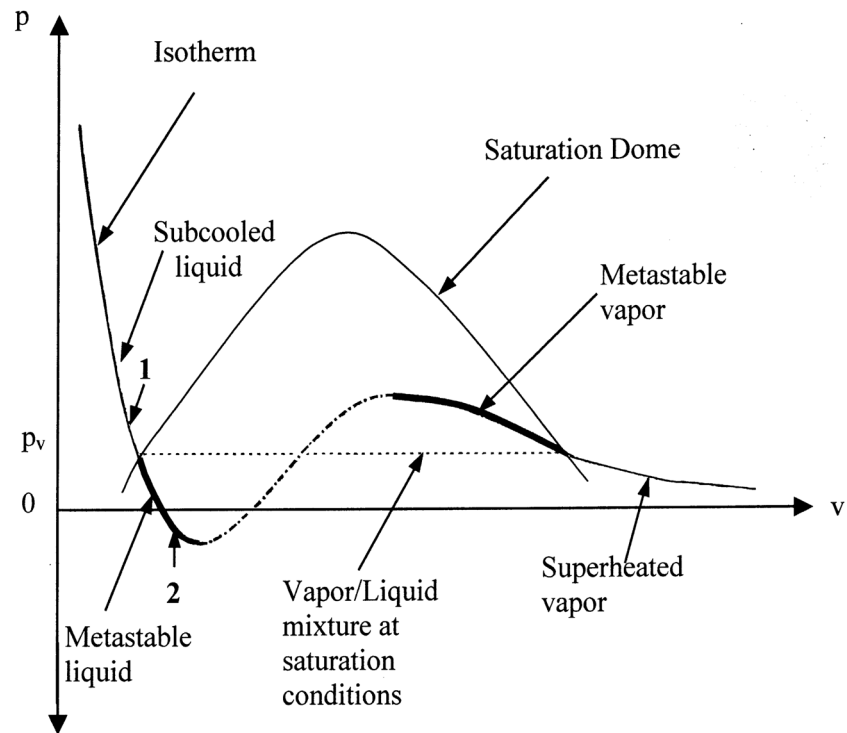
Figure 1. Van der Waals fluid isotherm. Isothermal expansion to achieve tension would follow the path (1 to 2).

result of pressure variations; the typical approach to hydrodynamic cavitation uses a cavitation index k that neglects viscous effects entirely (Young 1999):

$$k \equiv \frac{p - p_v}{\frac{1}{2}\rho u^2} \tag{1.12}$$

When viscous effects are considered important in cavitating flows, the usual explanation of cavitation still relies upon a reduction in the hydrodynamic pressure. This form of cavitation is called vortex cavitation, and it requires shear rates high enough to create vortices. If the pressure in the vortex core drops below a critical value, the liquid cavitates.

1.3   PNSCC

Bair and Winer first proposed that cavitation would occur in a liquid when the most tensile principal stress becomes tensile (Bair and Winer 1987). They demonstrated that variations of ambient pressure too small to affect viscosity had a pronounced effect on viscosity measurements in which the magnitude of the shear stress, τ_{xy}, was near that of the pressure, p. They later suggested the possibility that a lubricant could withstand a slight tension without cavitating (Bair and Winer 1992). Joseph independently proposed a similar criterion, introducing the possibility that the tensile strength, σ_c, could be positive or negative, making his criterion for cavitation $\sigma_1 > \sigma_c$ (Joseph 1998). If $\sigma_c > 0$ then the liquid has some ability to withstand a tensile principal stress; if $\sigma_c = 0$ then the criterion is that originally proposed by Winer and Bair; and if $\sigma_c < 0$ then the liquid cavitates at some stress that is still compressive. The case of $\sigma_c < 0$ is analogous to the idea of a liquid cavitating if the hydrodynamic pressure is reduced to the vapor pressure. A principal normal stress cavitation criterion predicts shear cavitation, that is, cavitation

in simple shear with no reduction of the hydrodynamic pressure, when the shear stress and the pressure are of the same order of magnitude, if $|\sigma_c| << |p|$.

Based on the knowledge that a liquid can withstand tension, it might be expected that σ_c would be a very large number. Much work in cavitation has attempted to explain why cavitation occurs at pressures above that suggested by the theoretical tensile strength of a liquid. The most accepted theory was introduced by Harvey *et al*. (Harvey *et al*. 1944) and expanded upon by Apfel and Crum (Apfel 1970; Crum 1982). They postulate that cavitation occurs in most cases through the growth of preexisting voids. These voids, called nucleation sites, are filled with gas. Surface tension increases the pressure inside a gaseous bubble in a liquid, and the smaller the radius of the bubble, the greater its internal pressure. The higher the pressure in the bubble is, the greater the concentration difference driving diffusion of the gas out of the bubble will be. Therefore, a small gas bubble in a liquid requires some mechanism of stabilization to prevent its spontaneous disappearance. Several theories have been advanced for the method of nucleation site stabilization. None has been conclusively demonstrated.

One widely accepted theory for nuclei stabilization is stabilization in a crevice on a solid impurity or bounding surface (Strasberg 1959; Winterton 1972; Plesset and Prosperetti 1977). A crevice stabilized gas nucleus can have an interface that is concave towards the liquid. Due to surface tension, the pressure of the gas in the nucleus can therefore be less than the pressure in the liquid, and if gas diffuses from the nucleus, so long as the contact line is pinned, the concavity will increase, reducing the pressure of gas. Hence such a nucleus can persist without dissolving completely into the liquid. The origin of such nuclei has been explained by considering the flow of a liquid onto a

hydrophobic surface with crevices (Atchley and Prosperetti 1989). Another explanation of the origin and persistence of nuclei is that ordering of liquid molecules adjacent to solid surfaces leads to local hydrophobicity in regions of concavity of an otherwise non-hydrophobic surface (Mørch 2000). This explanation suggests that the resulting voids have interfaces which are convex toward the liquids, and that their persistence is due to a resonant behavior forced by ambient vibrations. In this work, the terms nucleus, preexisting nucleus, and nucleation site, all refer to gas trapped between the liquid and solid surface, regardless of origin, rather than referring to the critical nucleus of classical nucleation theory (Blander, 1979).

Although agreement upon a theory of nucleation site stabilization has not been reached, it is generally accepted that stabilized gas bubbles are present in liquids and can act as nucleation sites.

1.4   SIGNIFICANCE – PNSCC

There are several implications of the principal normal stress criterion for cavitation. Some of the more obvious are in rheological measurements, where the assumption of a viscometric flow becomes invalid if cavitation has occurred. Of greater engineering significance are those real world situations about which the rheological data are supposed to provide insight. Cavitation could occur in polymer processing and lubrication applications where it has not been previously considered. A better understanding of the cavitation inception criterion will improve efforts at inhibiting cavitation when it is not desired, or ensuring cavitation when it is desirable. Cavitation can be desirable when used for mixing or degassing.

Once the possibility of cavitation due to a shear stress of the order of the imposed hydrostatic pressure (usually 0.1 MPa) is considered, numerous examples of phenomena that may be explained by shear cavitation can be found. Archer *et al.* found evidence of cavity formation at shear stresses in the range of 0.1 to 0.3 MPa for experiments performed at atmospheric pressure in low molecular weight polystyrene and α-D-glucose (Archer *et al.* 1997). Cogswell found that high-density polyethylene flow curves generated using a capillary tube viscometer show a decrease in the apparent viscosity of an order of magnitude at a shear stress of 0.2 MPa. He found a similar discontinuity in measurements obtained using a Couette viscometer at a shear stress of the order of 0.1 MPa (Cogswell 1973). In both cases it seems that shear cavitation may be explanatory. Vinogradov found that effects such as those reported by Cogswell are seen in many linear polymers; there is a critical stress in the range of 0.1 to 0.3 MPa for capillary tube viscometers, above which there is an abrupt drop in apparent viscosity. Additionally, for the same liquids in rotational devices, an abrupt drop in torque and separation of the sample from the measuring surface occurs at a critical stress about half that seen in the capillary tube viscometer (Vinogradov 1975). The drop in resistance to flow in capillary tube measurements is linked, in the literature, to wall slip within the capillary (called melt fracture) and to an irregular appearance of the extrudate leaving the capillary (called "shark skin" or "elastic turbulence"). It has been shown for a cis-polyisporene and a cis-polybutadiene that raising the hydrostatic pressure can inhibit elastic turbulence (Vinogradov 1967).

Polymer manufacturers use high temperature, low pressure processes combined with an application of a shear stress in devolatilization (Albalak 1996). Favelukis *et al.*

found that, for a low molecular weight polybutene, vacuum was insufficient to cause boiling and growth of gaseous bubble. In addition, a critical level of shear was required (Favelukis *et al*. 1997). Their findings suggest that polymer devolatilization processes sometimes rely upon shear cavitation.

CHAPTER 2

SHEAR CAVITATION – COUETTE EXPERIMENT

A principal normal stress cavitation criterion has previously been hypothesized (Bair and Winer 1987; Joseph 1998), and "circumstantial" evidence abounds (i.e., Cogswell 1973; Archer 1997). However, to date, the only attempt to test the criterion experimentally was indirect. Bair and Winer measured the torque $\mathcal{T} = FR$ due to the total wall shear force F on a wall at radius R in a Couette type device

$$F = \int_A \tau_w dA \tag{2.1}$$

They calculated the apparent viscosity $\eta(\dot{\gamma})$ as a function of apparent shear rate $\dot{\gamma} = U/L$

$$\eta(\dot{\gamma}) = \frac{\mathcal{T}/R}{U/L} \tag{2.2}$$

where the wall velocity U was controlled and the shear gap L was small to allow high shear stresses in the liquid without a reduction of viscosity due to viscous heat generation. They obtained curves of $\eta(\dot{\gamma})$ at different ambient pressures p from vacuum to 10 atmospheres and saw an effect of pressure on viscosity too great to be explained by the usual piezoviscous response. The effect was a reduction in viscosity with shear stress, apparent shear thinning, where the onset of the viscosity reduction occurred when $\tau \sim p$ (Bair and Winer 1987). In terms of testing the PNSCC, this could be considered using apparent viscosity measurement as an indirect method of detecting cavitation onset.

In this work, an experiment similar to that of Bair and Winer is performed, but the detection of cavitation onset is visual, and hence, direct.

The primary goal of the experiments was to determine at what level of shear stress, if any, cavitation occurs for various ambient pressures. The onset of cavitation was detected through visual observation; the recordings of apparent shear stress and video images of the sheared liquid were reviewed for indications of cavitation.

2.1   APPARATUS

A Couette viscometer was constructed which allows visualization of the liquid sample undergoing shear and which allows control of the ambient pressure in a range of 15 kPa to 300 kPa (Figure 2).

The viscometer is of the inner rotating cylinder type. The outer cylinder is a commercially produced Pyrex tube with an inner diameter of 1.593 cm. The inner cylinder, or bob, was produced by machining a precipitation hardened steel, lapping the bob to the desired final diameter and then polishing. The bottom of the inner cylinder is tapered to allow trapped gas bubbles to more easily escape. The outer diameter of the steel bob was 1.582 cm and upon calibration with a viscosity standard the gap between the bob and pyrex cylinder was 50 μm.

A DC stepper motor drove the bob, allowing the rate of shaft rotation to be specified. The stepper motor was connected to the drive shaft by a flexible coupling. The penetration of the pressure boundary by the shaft was sealed with a spring energized Teflon seal. An adjustable length shaft coupled the drive shaft to the bob. The adjustable shaft connected to both the drive shaft and the bob with universal joints, preventing the transmission of lateral thrust while permitting the transmission of torque. An O-Ring sealed pressure fitting also penetrated the pressure boundary, allowing connection of either a vacuum pump or pressurized gas source to the viscometer.
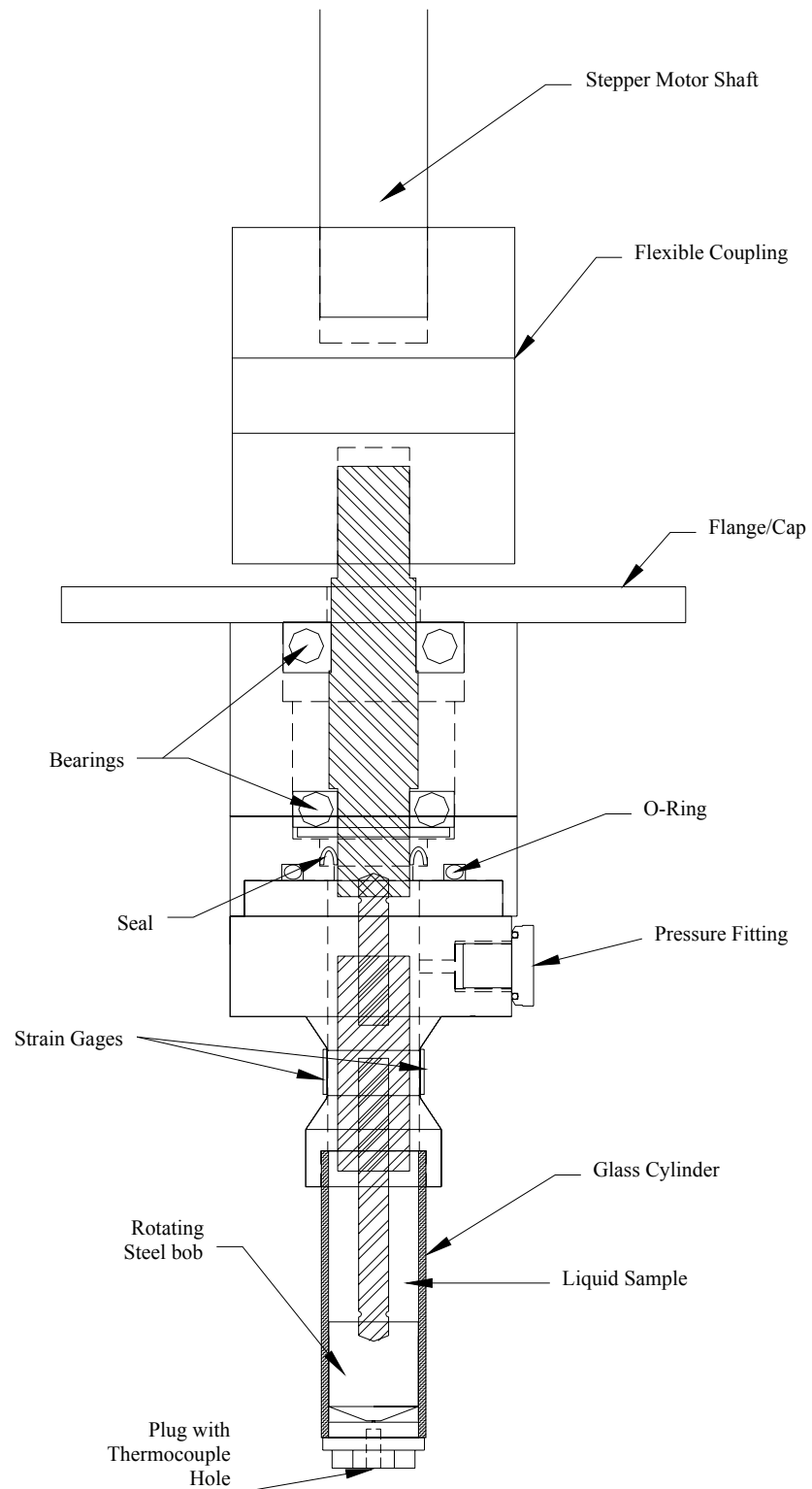
Figure 2. Variable pressure Couette viscometer and flow cell.

The determination of apparent shear stress in the liquid sample, τ_{app}, was accomplished via torque measurement using strain gages attached to a thin walled portion of the aluminum body of the viscometer. If the flow was simple shear, then the apparent shear stress was the shear stress at the glass surface. Due to the small ratios of gap to bob radius and gap to bob height, the apparent shear stress and shear stress in the gap were nearly identical provided the flow is parallel. The flow conditions in the experiments were such that there should have been no instabilities; therefore, the apparent shear stress and the shear stress in the gap were taken as the same unless cavitation occurs.

Customized Labview based video and data acquisition software provided by Ammons Engineering was configured to allow simultaneous recording of the output from a digital camera and a digital signal. The strain gage excitation was from a Measurements Group 2110A power supply, and output from the torque sensor was passed through a Measurements Group 2120A signal conditioner and Dataq DI194 A/D converter. The software was calibrated to record the signal as apparent shear stress, τ_{app}. The camera, a Basler model A 101f, is monochrome with a maximum resolution of 1300 x 1030 pixels and with programmable exposure controls. It was fitted with a Navitar Zoom 7000 lens with a focal distance of 18 to 108 mm, which could provide 6X magnification.

2.2 EXPERIMENTAL LIQUIDS

The Couette viscometer was used to study shear cavitation in a polybutene (PB), H-1900, provided by Amcco, and a polydimethylsiloxane (PDMS), DC-200-10^6, provided by Dow Corning. Both liquids have limiting zero shear viscosities of 1000 Pa s at room temperature. The PB is Newtonian to high shear stresses due to its low

molecular weight (2500 g/mol), while the PDMS is expected to show non-Newtonian behavior at shear stresses of the order of 1×10^4 Pa. The PB is relatively temperature sensitive ($\beta = 0.027$ K^{-1}) while the PDMS is not ($\beta = 0.007$ K^{-1}).

2.3   RESULTS

The effect of shear stresses up to and beyond the magnitude of the ambient pressure was investigated for the PB and PDMS in the Couette viscometer. Experiments were performed at absolute ambient pressures from 18 kPa to 300 kPa, for apparent shear stresses from 10 kPa to 270 kPa with shear rates up to 745 s^{-1}. The experiments were performed at liquid temperatures from 19 ˚C to 26 ˚C. Figure 3 shows images for different shear stresses in PB. Cavitation is clearly visible in the bottom two images. The widths of the voids in the images are between 0.01 and 0.1 cm. The data plotted in Figure 4 show the lowest shear stress, for a given pressure, for which a cavitation event was visually detected.

The hypothesis being tested in this experiment was one of zero critical stress, $\sigma_c = 0$. For PB this corresponds to cavitation occurring when the measured shear stress magnitude reaches the ambient pressure magnitude. For PDMS, nonzero normal stress differences were expected to result in cavitation at shear stresses of magnitudes less than the magnitude of ambient pressure, as predicted by Eq. (1.10).

PDMS is highly non-Newtonian. The correct cavitation criterion is Eq. (1.10), which takes into account normal stress differences. To plot this criterion, in the absence of measurements of first normal stress differences, a model must be incorporated to permit their calculation. The estimation of first normal stress difference coefficient

15
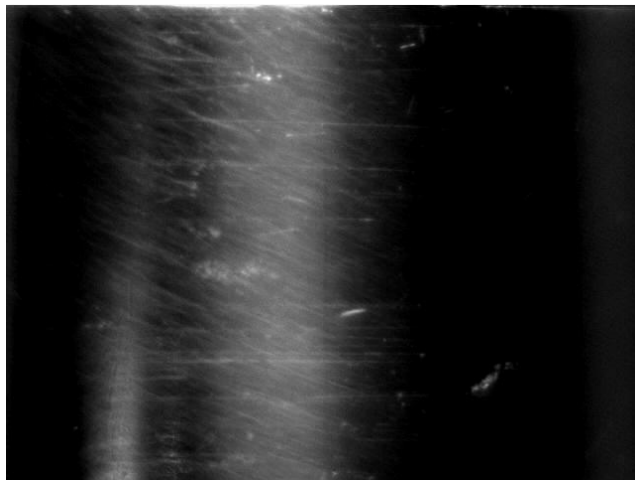
1 cm a) $\tau = 14$ kPa
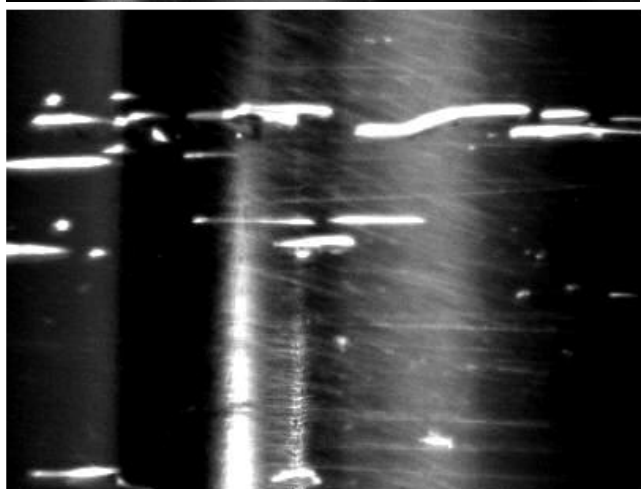
b) $\tau_{app} = 23$ kPa
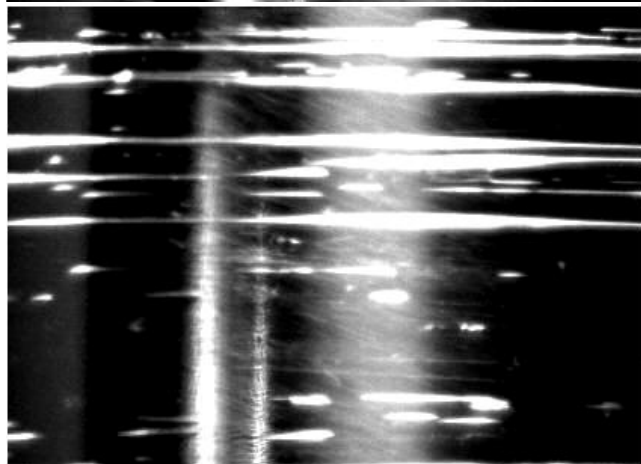
c) $\tau_{app} = 35$ kPa

Figure 3. Polybutene (H-1900) 20 ˚C, *p* = 19 kPa, sheared in 50 μm gap. Cavitation is visible when shear stress was greater than the hydrostatic pressure.
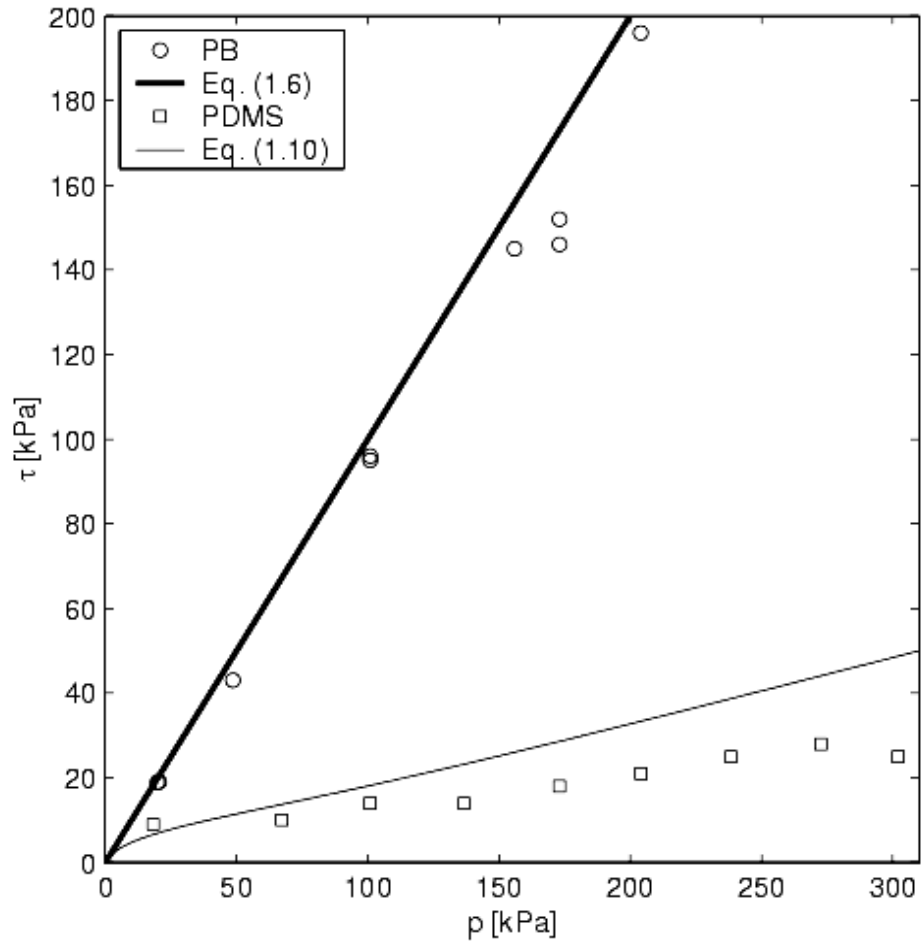
Figure 4. Shear stress at which cavitation was first observed for polybutene (H1900), and for polydimethylsiloxane (PDMS). The hypothesized $\sigma_c = 0$ criterion predicts cavitation for τ above and to the left of the solid lines.

Stastna 1986). Normal stress difference coefficients are the viscometric shear functions defined $\Psi_i(\dot{\gamma}) = N_i(\dot{\gamma})/\dot{\gamma}^2$, and are considerably more difficult to measure than the viscosity function.

De Kee and Stastna considered several relationships between the first normal stress difference coefficient Ψ_1 and the viscosity function, including those of Wagner (Wagner 1977)

$$\Psi_1(\dot{\gamma}) = -\frac{1}{z}\frac{d\eta}{d\dot{\gamma}} \tag{2.3}$$

and Gleißle (Gleißle 1982)

$$\Psi_1(K\dot{\gamma}) = -2\int_{\eta_\infty}^{\eta}\frac{d\eta}{\dot{\gamma}} \tag{2.4}$$

They noted that both Eq. (2.3) and (2.4) predict the same kind of behavior at high shear rates, namely

$$N_1 \propto \tau \quad \dot{\gamma} \gg \lambda \tag{2.5}$$

where λ is the longest characteristic relaxation time, which can be estimated using a result from molecular theory (Bird *et al.* 1987),

$$\lambda = \frac{\mu M}{\rho R_u T}, \tag{2.6}$$

M is the molecular weight, and R_u is the universal gas constant. Although Eq. (2.5) can not be assumed to be generally true (Ait-Kadi *et al.* 1989), Gleißle's data on PDMS show that it is accurate for polydimethylsiloxanes with zero shear viscosities from 200 to 20,000 Pa s. Equations (2.3) and (2.4) have several shortcomings. Namely, the parameter z and the shift factor K are not reliably predictable; furthermore, Eq. (2.3) predicts that Ψ_1 goes to zero as η becomes constant at low shear rates.

Although it is possible to implement predictions of Ψ_1 from Eqs. (2.3) or (2.4) working numerically from viscosity data, it is more convenient to have an explicit functional relationship between η and $\dot{\gamma}$. A well accepted relationship is the Carreau-Yasuda equation (Macosko 1994),

$$\eta = \frac{\mu}{\left[1+(\dot{\gamma}\lambda)^a\right]^{\frac{1-n}{a}}} . \tag{2.7}$$

which is plotted for $a = 1$ and $n = 0.3$ in Figure 5 along with vicosity data from the Couette device and a capillary viscometer. The molecular weight of PDMS, used to calculate λ, is found using an equation for polydimethylsiloxanes (Barry 1946)

$$M = \left(\frac{\log_{10}(\nu)+5}{0.0123}\right)^2 \tag{2.8}$$

where the kinematic viscosity, ν, is in SI units of m^2/s and measured at 25 ° C. This gives $M = 165000$ g/mol and $\lambda = 0.07$ s.

Upon considering Eq. (2.7) we note that the choice of $a = 1$, which indicates a very broad transition from Newtonian to non-Newtonian behavior, has the result of eliminating the biggest flaw with Wagner's model, Eq. (2.3). Recall that Wagner's model incorrectly predicts $\Psi_{1o} = 0$ at low shear rates. However, for $a = 1$, although

$$\lim_{\dot{\gamma}\to 0}\eta(\dot{\gamma}) = \mu \tag{2.9}$$

is still true, it is no longer true that

$$\lim_{\dot{\gamma}\to 0}\frac{d\eta}{d\dot{\gamma}}(\dot{\gamma}) = 0 \tag{2.10}$$

Instead, the model correctly predicts, at low shear rate, a constant first normal stress difference coefficient Ψ_{1o}
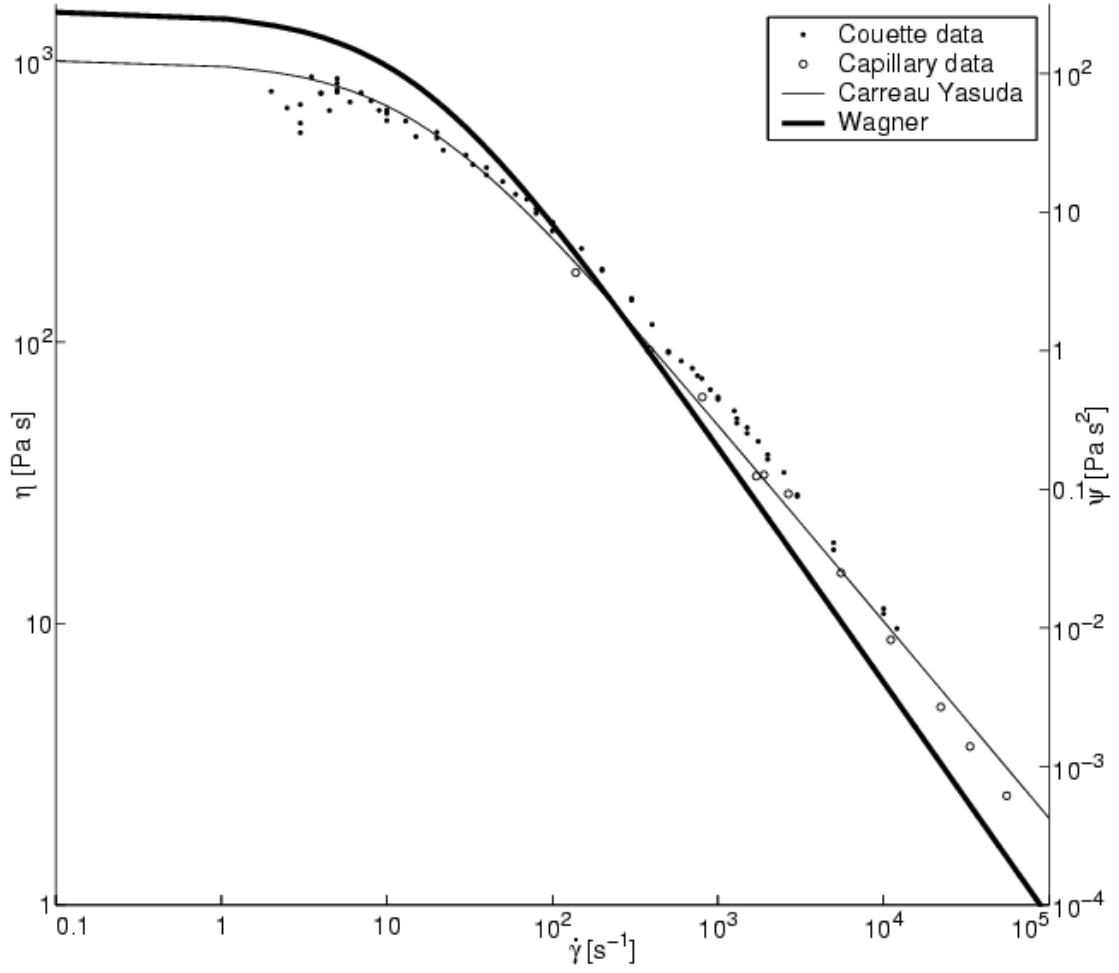
Figure 5. Viscosity η (left axis) and first normal stress difference coefficient Ψ_1 (right axis) for PDMS. The viscosity data comes from the Couette device (dots) and a capillary tube (circles). The thin line is the Carreau-Yasuda equation, Eq. (2.7), for η with μ=1000 Pa s, λ=0.07 s, a=1 and n = 0.3. The thick line is Wagner's model for Ψ_1 with the Carreau-Yasuda equation (a = 1), Eq. (2.11), with Ψ_{1o}= 280 Pa s^2, λ = 0.07 s and n = 0.3.

$$\Psi_1 = \Psi_{1o}\left[1+(\dot{\gamma}\lambda)\right]^{n-2} \qquad (2.11)$$

In general Ψ_{1o} cannot be easily predicted. But because Gleißle has measured Ψ_1 for polydimethylsiloxanes of both higher and lower viscosities than those used here, Ψ_{1o} can in this case be easily estimated in the following manner. From Gleißle's plot of $\Psi_1(\dot{\gamma})$ for polydimethylsixanes of various viscosities and hence molecular weights one finds that for $M = 145000$ g/mol, Ψ_{1o} is 170 Pa s^2 and for $M = 185000$ g/mol, Ψ_{1o} is 440 Pa s^2. Assuming a power law relationship between Ψ_{1o} and M (Tanner 2002), one finds Ψ_{1o} is 280 Pa s^2. The curve plotted as the cavitation model for PDMS in Figure 4 is τ vs. p from Eq. (1.10) where τ and N_1 are found using η and Ψ_1 from Eqs. (2.7) and (2.11) respectively.

For the Newtonian liquid PB the results in Figure 4 demonstrate good agreement with the PNSCC hypothesis; however, for PDMS, the predicted shear stress is higher than the observed shear stress at cavitation. The error increases as the shear stress exceeds the modulus $G=\mu/\lambda = 14$ kPa, a strong indicator that the deviation is due to non-Newtonian behavior.

Because it was possible to observe the cavitation event, further information about shear cavitation can be inferred. Multiple voids were frequently observed in the same horizontal band. This may be an indication of cavitation inception from wall crevice stabilized nuclei. Based upon the perseverance of voids after the removal of the shear stress, especially following shearing at reduced pressure, it is likely that the cavitation process was primarily one of gaseous cavitation; thus the void filled with gas that was in solution in the liquid, rather than vapor.

Cavitation can lead to experimental errors in rheological measurements analogous to those due to viscous heating that were exposed primarily by Gruntfest (Gruntfest 1965). The presence of gaseous voids during the application of high shear rates results in a reduction in the apparent viscosity. Experimentally this manifests as either apparent shear thinning or thixotropy. Figure 6 shows the effect of cavitation manifesting as apparent shear thinning. Apparent shear stress and shear rate data for PB was collected using the Couette device by starting at low shear rate and incrementally increasing the shear rate, for both low (19 kPa) and atmospheric pressure. The data is displayed in the figure as apparent viscosity η as a function of shear rate. PB should display Newtonian behavior to shear stresses of approximately 500 kPa; however, instead it appears to shear thin at $\tau > p$. The apparent shear thinning is due to cavitation.

After the atmospheric pressure flow curve was generated, the apparent viscosity was again measured at a shear rate of 80 s^{-1} and found to be 75% of its previous value. PB is not thixotropic; this apparent loss of viscosity is due to cavitation.

2.4 CONCLUSIONS

In this chapter we have presented the results of an experiment designed to test the PNSCC directly through visual detection of cavitation of liquids sheared under controlled pressure. Two polymeric liquids were used, PB and PDMS. Both have the same low shear viscosity at room temperature. PB is Newtonian to very high shear stresses and has a relatively low molecular weight. For PB the experimental results of shear stress τ at cavitation onset agree well (within 16%) with the predictions of the PNSCC with $\sigma_c = 0$. PDMS has a much higher molecular weight, and its behavior is consequently non-Newtonian at lower shear stresses. Therefore, predicting the onset of cavitation with the
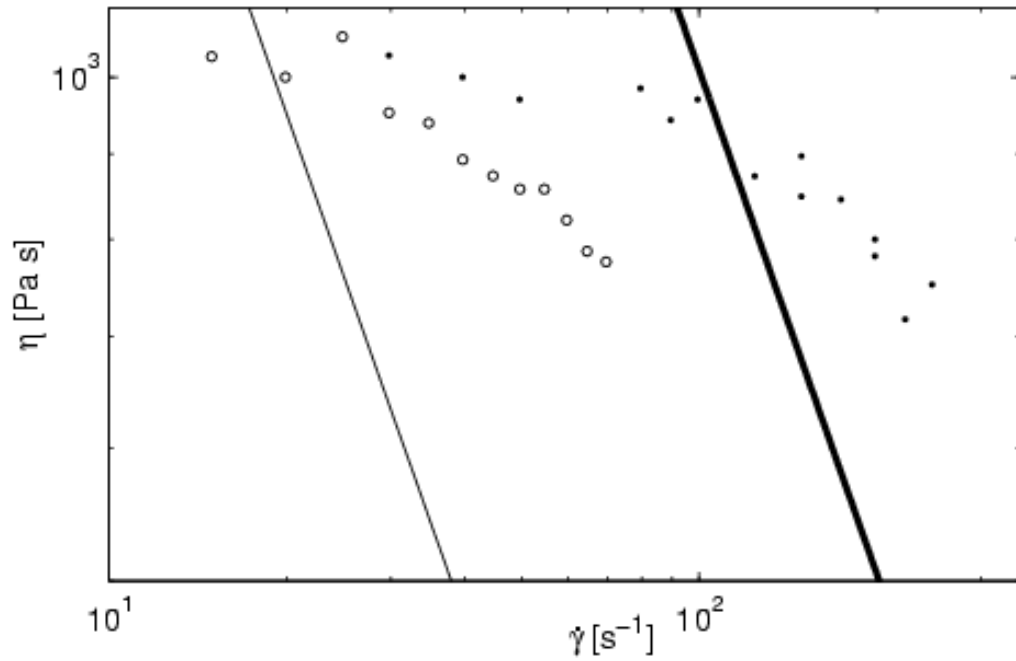
Figure 6. Apparent viscosity vs. shear rate at room temperature for PB at $p = 19$ kPa (open circles) and $p = 101$ kPa (dots). The lines are of constant shear stress equal to the applied pressures, ie. the thin line is a line of constant 19 kPa and the thick line is a line of constant 101 kPa . Based on constitutive behavior, η should be a constant of 10^3 Pa s for all shear rates shown. The apparent shear thinning at shear stresses greater than the applied pressure is due to cavitation.

PNSCC requires knowledge of normal stress differences. First normal stress differences were estimated using predictions incorporating the non-Newtonian shear viscosity. The validity of the estimated values of N_1 are supported by results presented in Chapter 4. The PNSCC is not as effective at predicting cavitation onset in the PDMS as it is for PB. At higher pressures, the predicted stress for cavitation onset is nearly twice the observed value. For the PNSCC to be accurate, the critical stress σ_c, would have to be considered a function of pressure p, or, possibly, also a function of some measure of the importance of non-Newtonian effects, such as the Weisenberg number.

CHAPTER 3

SHEAR CAVITATION – MODEL AND SIMULATION

The experiments in Chapter 2 show that for a Newtonian liquid (PB) in simple shear, cavities grow visible when the shear stress equals the ambient pressure. This is predicted by a principal normal stress cavitation criterion with a critical stress of zero. However, one can also show experimentally (Kottke *et al.* 2003) that liquids can withstand tension when the liquid is first pressurized to eliminate preexisting voids. Therefore, a critical stress of zero suggests that the cavitation originates from preexisting voids. Stabilization of voids in a liquid can be explained by void formation in a crevice on some solid surface (Plesset and Prosperetti 1977). A reasonable hypothesis is that shear cavitation occurs when the shear flow causes the growth of such preexisting voids to macroscopic size. The observation that multiple voids are frequently observed in the same horizontal band provides further support to the concept of inception from wall crevice stabilized nuclei. Based upon the perseverance of voids after the removal of the shear stress, it is likely that the cavitation process is primarily one of gaseous cavitation. Thus the void fills with gas that was in solution in the liquid, rather than vapor.

The model for cavitation from a crevice stabilized gas nucleus consists of two systems, the liquid with dissolved gas, Ω_A (Figure 7), and the void, or gas bubble, Ω_B (Figure 8). The two systems interact at the interface surface $\partial\Omega_{AB}$. The liquid system, Ω_A, is semi-infinite; it is bounded by parallel solid walls, $\partial\Omega_A$, above and below (x_2^* equals L and 0 respectively), and unbounded in the x_1^* and x_3^* directions. The upper portion of $\partial\Omega_A$, at $x_2^* = L$, is translating in the x_1^* direction at a constant speed, U. Note
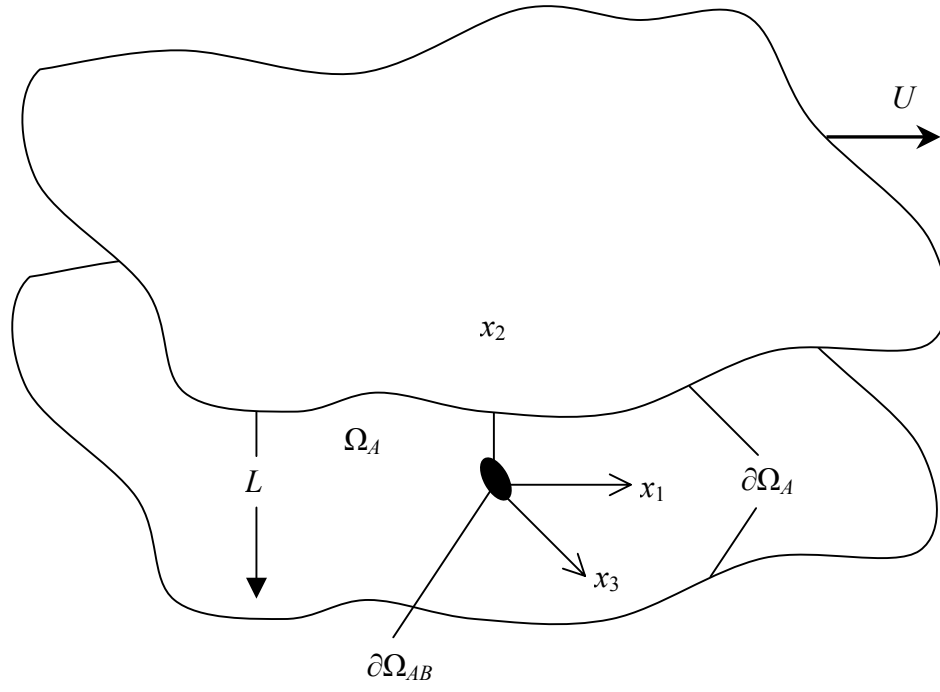
Figure 7. Liquid domain (Ω_A) for the model for inception of shear cavitation.
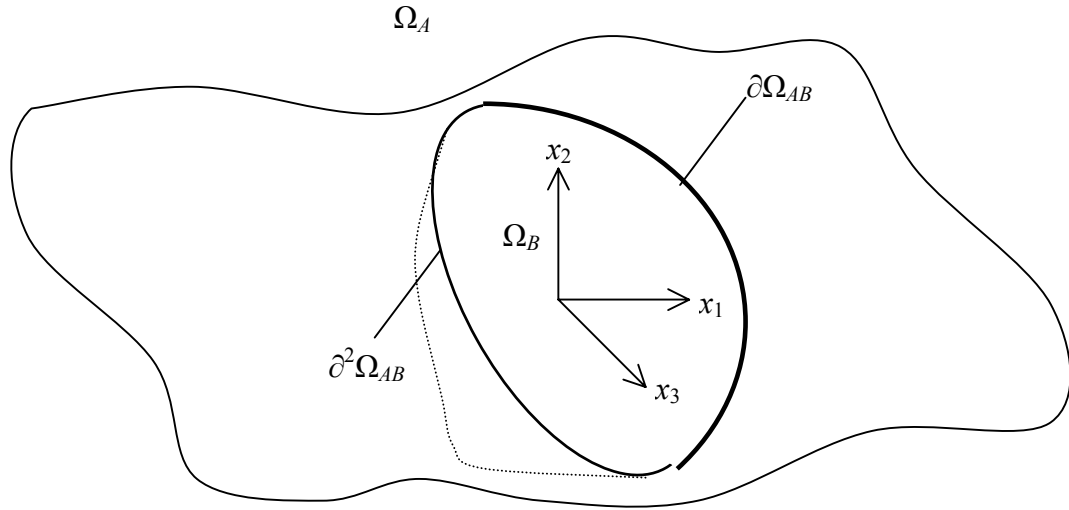
Figure 8. Gas domain (Ω_B) for the model for inception of shear cavitation.

26

that throughout the remainder of this chapter asterisks (*) denote the dimensional form of the variable. The gas system, Ω_B, is finite. It is bounded above by the gas liquid interface, $\partial\Omega_{AB}$, and below by the solid, unmoving crevice. The intersection of the gas liquid interface, $\partial\Omega_{AB}$, with the lower solid surface, $\partial\Omega_A$, is the contact line, $\partial^2\Omega_{AB}$.

The purpose of the model is the simulation of void deformation and growth from a crevice stabilized gas nucleus in Couette flow. The experimental results, which support the principal normal stress cavitation criterion with a critical stress of zero, when combined with a hypothesis of gaseous cavitation from a crevice stabilized nucleus, lead to several questions. Namely, does the critical stress depend upon surface tension, the diffusion coefficient of the gas in the liquid, the gas initial and boundary conditions, and the contact line dynamics?

3.1   MATHEMATICAL MODEL OF INCEPTION

3.1.a Dimensional Governing Equations

In Ω_A the liquid is assumed to be Newtonian and the flow is incompressible. The model is isothermal and the properties are assumed to be uniform. Body forces are neglected. Therefore the flow in Ω_A is governed by the Navier-Stokes Equations,

$$\rho\left\{\frac{\partial\mathbf{u}^*}{\partial t^*}+\mathbf{u}^*\cdot\nabla^*\mathbf{u}^*\right\}=-\nabla^*p^*+\mu\nabla^{*2}\mathbf{u}^*$$
$$\nabla^*\cdot\mathbf{u}^*=0$$

(3.1)

Assuming Fickian diffusion and a constant binary mass diffusivity of gas in the liquid, D, the molar concentration of dissolved gas in the liquid, c, is governed by the advection $-$ diffusion equation

$$\frac{\partial c^*}{\partial t^*} + \mathbf{u}^* \cdot \nabla^* c^* = D \nabla^{*2} c^* \tag{3.2}$$

The gas in the void, Ω_B, is assumed to be isothermal and to obey the ideal gas equation of state

$$p_B^* = c_B^* R_u T \tag{3.3}$$

Conservation of mass for the void requires

$$\frac{dN_B^*}{dt^*} = -D \int_{\partial\Omega_{AB}} \frac{\partial c^*}{\partial n^*}\bigg|_{\partial\Omega_{AB}} dA^* \tag{3.4}$$

where N_B is the total moles of gas in the void, and the spatial derivative is the normal gradient of the concentration at the bubble surface

3.1.b Dimensional Boundary Conditions

On the solid surfaces, $\partial\Omega_A$, the no slip, no penetration condition is applied:

$$\begin{aligned} u_2^* &= 0 \text{ at } x_2^* = 0 \\ u_1^* &= U^* \text{ at } x_2^* = L \end{aligned} \tag{3.5}$$

Far from the void, the void no longer disturbs the flow,

$$\begin{rcases} u_2^* \to 0 \\ p^* \to p_\infty^* \end{rcases} \text{ as } x_2^*, x_3^* \to \infty . \tag{3.6}$$

The air in Ω_B is treated as inviscid; therefore, on the gas liquid interface, $\delta\Omega_{AB}$,

$$f_t^* = 0 \text{ on } \partial\Omega_{AB} \tag{3.7}$$

where f_t^* represents both tangential components of the traction vector, $\mathbf{f}$.

The interface is assumed to have an isotropic surface tension, γ, and therefore

$$f_n^* = 2\kappa_m^* \gamma - p_B^* \text{ on } \partial\Omega_{AB} \tag{3.8}$$

where f_n^* is the normal component of the traction vector, κ_m^* is the mean curvature of the interface, and p_B^* is the pressure in Ω_B.

28

The appropriate boundary condition for the contact line, $\partial^2\Omega_{AB}$, is a matter of considerable ongoing research and will be addressed in more detail later. In general, it will provide some relationship between contact line velocity, $\mathbf{u}^*_{CL}$, and apparent contact angle, θ. The contact line velocity will be zero wherever the contact angle is between the receding and advancing contact angles, $\theta_R < \theta < \theta_A$.

The kinematic condition on the gas liquid interface, $\partial\Omega_{AB}$, requires the position of the interface, $\mathbf{x}^*_{\partial\Omega_{AB}}$, to be advected with the local velocity, $\mathbf{u}^*$:

$$\frac{d\mathbf{x}^*_{\partial\Omega_{AB}}}{dt^*} = \mathbf{u}^* \text{ on } \partial\Omega_{AB} \tag{3.9}$$

The boundary conditions for the concentration of dissolved gas in Ω_A are that the concentration far from the void is unaffected by the mass transfer to or from the void

$$c^* \rightarrow c^*_\infty \text{ as } x^*_1, x^*_3 \rightarrow \infty; \tag{3.10}$$

the normal gradient of dissolved gas concentration is zero on the solid boundaries,

$$\frac{\partial c^*}{\partial x^*_2} = 0 \text{ at } x^*_2 = 0 \text{ and } x^*_2 = L; \tag{3.11}$$

and, at the gas liquid interface, the concentration of dissolved gas in the liquid is proportional to the pressure of the gas in the void in accordance with Henry's law

$$c^* = Hp^*_B \text{ on } \partial\Omega_{AB}. \tag{3.12}$$

Equation (3.12) should be a good approximation so long as the gas pressure does not exceed $O(10^6 \text{ kPa})$ and the solubility of the gas in the liquid does not exceed $O(1 \text{ mol } \%)$ (Prausnitz et al. 1999).

3.1.c Scaling

The natural length and velocity scales are L and U. A reasonable alternative would be a length scale based on the initial void size and the associated velocity scale,

the product of the length scale and U/L. There are several other possible velocity scales, based on the contact line dynamics model (Smith 1995) or the ratio of the surface tension γ to the dynamic viscosity μ (Crowdy 2003). However, for comparison with experiment, the scales chosen are best, as they are most easily known. Given the length and velocity scales, the kinematic boundary condition, Eq. (3.9), yields the time scale, L/U. Based upon the cavitation criterion, the pressure scaling is chosen to be a viscous scale: $\mu U/L$. The scaled Navier-Stokes equation and species conservation equation in terms of now dimensionless variables are

$$\mathrm{Re}_L\left\{\frac{\partial \mathbf{u}}{\partial t}+\mathbf{u}\bullet\nabla\mathbf{u}\right\}=-\nabla p+\nabla^2\mathbf{u}$$

$$\nabla\bullet\mathbf{u}=0$$

(3.13)

and

$$\mathrm{Pe}_L\left[\frac{\partial c}{\partial t}+\mathbf{u}\bullet\nabla c\right]=\nabla^2 c$$

(3.14)

Re_L is the Reynolds number, $\rho UL/\mu$ and Pe_L is the Peclet number for diffusion, UL/D.

In the Couette experiments using polybutene,

$$L\sim10^{-5}\,\mathrm{m},\ \mu\sim10^3\ \mathrm{Pa\ s},\ \rho\sim10^3\ \mathrm{kg\ m^3},\ U\sim10^{-3}\ \mathrm{m\ s^{-1}},\ D\sim10^{-10}\ \mathrm{m^2\ s^{-1}} \quad (3.15)$$

These values give a Reynolds' number, $\mathrm{Re}_L=\rho UL/\mu$, of order 10^{-8}, and Peclet number,

$\mathrm{Pe}_L=UL/D$, of order 10^2 for PB.

In the Couette experiments using polydimethylsiloxane,

$$L\sim10^{-5}\,\mathrm{m},\ \mu\sim10^2-10^3\ \mathrm{Pa\ s},\ \rho\sim10^3\ \mathrm{kg\ m^3},\ U\sim10^{-2}\ \mathrm{m\ s^{-1}},\ D\sim10^{-9}\ \mathrm{m^2s^{-1}} \quad (3.16)$$

(The low shear viscosity for PDMS is 10^3 Pa s but the experiments show cavitation at a shear stress for which shear thinning has reduced the viscosity by about an order of magnitude.) The values in Eq. (3.16) give a Reynolds' number, $\mathrm{Re}_L\sim10^{-6}$, and Peclet

number, $\mathrm{Pe}_L \sim 10^2$ for PDMS.

Based on the very small Reynolds numbers, consideration is limited to the Stokes approximation, in which inertial effects are neglected and the equations governing the flow in Ω_A are quasi-steady. Therefore Eq. (3.13) is rewritten as

$$\nabla^2 \mathbf{u} = \nabla p$$
$$\nabla \cdot \mathbf{u} = 0 \tag{3.17}$$

The moderate Peclet numbers preclude applying such a simplification to Eq. (3.14) at this point.

The scale for the dissolved gas concentration is based on Henry's law and saturated gas conditions,

$$c_s = H p_\infty \tag{3.18}$$

which results in the scaled equation of state for the gas:

$$p_B = CiHR_u T c_B \tag{3.19}$$

Equation (3.4), becomes

$$\frac{dN_B}{dt} = -\left(\mathrm{Pe}_L\right)^{-1} \int_{\partial\Omega_{AB}} \frac{\partial c}{\partial n} dA . \tag{3.20}$$

The scaled boundary conditions are

$$u_2 = 0 \text{ at } x_2 = 0$$
$$u_1 = 1 \text{ at } x_2 = 1; \tag{3.21}$$

$$\left.\begin{array}{l} u_2 \to 0 \\ \dfrac{\partial u_1}{\partial x_2} \to 0 \\ p \to Ci \end{array}\right\} \text{ as } x_1, x_3 \to \infty \tag{3.22}$$

$$f_t = 0 \text{ on } \partial\Omega_{AB} \tag{3.23}$$

$$f_n = \frac{2}{Ca_L} \kappa_m + p_B \text{ on } \partial\Omega_{AB} \tag{3.24}$$

31

$$\frac{d\mathbf{x}_{\partial\Omega_{AB}}}{dt} = \mathbf{u} \text{ on } \partial\Omega_{AB} \tag{3.25}$$

$$c \to c_\infty \text{ as } x_1, x_3 \to \infty \tag{3.26}$$

$$\frac{\partial c}{\partial x_2} = 0 \text{ at } x_2 = 0 \text{ and } x_2 = 1 \tag{3.27}$$

and,

$$c = \frac{p_B}{Ci} \text{ on } \partial\Omega_{AB} \tag{3.28}$$

The traction has been scaled with a viscous scale, $\mu U/L$, to be consistent with the pressure scale, and the curvature is scaled with the inverse of the length scale, L. Ci is the cavitation index,

$$Ci \equiv \frac{p}{\sigma_1 + p} = \frac{p}{\mu \dfrac{U}{L}}. \tag{3.29}$$

Ci is unity when the shear stress equals the pressure far from the void. A principal normal stress cavitation criterion with zero critical stress predicts cavitation for $Ci < 1$. Ca_L is the capillary number

$$Ca_L \equiv \frac{\mu U}{\gamma}; \tag{3.30}$$

it is a measure of the strength of the viscous stress relative to surface tension. The degree of gas saturation of the liquid is given by c_∞, which is unity if the liquid is saturated with gas due to the presence of an interface with gas as pressure p_∞.

An examination of the above equations and boundary conditions reveals six parameters: Pe_L, Ca_L, Ci, HR_uT, θ_R, and θ_A. Additional parameters may appear in the contact line model, and the shape of the crevice can be considered at least one additional parameter, making the minimum number of parameters seven. Varying initial conditions could lead to further complication, some of which can be eliminated by considering only those initial conditions for which the system would be in mechanical equilibrium in the absence of any flow.

Solution of the three dimensional model to investigate the effect of the seven parameters would be extremely time consuming. Also, the extraction of meaningful information, and gaining insight into the important trends, is made difficult with so many parameters. The model could be used in an attempt to match the experimental results, but, due to the lack of information about several important components of the parameters, especially contact angles and crevice geometry; any such process would be questionable. Therefore, further simplification is both necessary and desirable.

3.1.d Further Simplifications

In the experiments, the distance which corresponds to L in Figure 7 was 50 μm, while the voids generally had a width of about 500 μm. Therefore it seems likely that variations in the x_3 direction are considerably smaller than those in the x_1 and x_2 directions, and a two-dimensional model for bubble growth may be appropriate (Figure 9). Indeed, previous investigations of bubble and droplet deformations have found that two-dimensional models yield pertinent and valuable information to the three dimensional case (Tanveer and Vasconcelos 1995). Therefore a two-dimensional model will be used as a simplified the cavitation model.

There are two limiting cases for which the solution of Eq. (3.14) becomes unnecessary. One is the case of an impermeable liquid, for which there is no mass transport from the liquid to the void and hence the number of moles of gas in the void, N_B, remains constant. The other is the case of infinitely fast diffusion, for which the gas concentration in the void, c_B, remains constant. Although neither limiting case is a close approximation of the experimentally examined cases, they provided two very different vantages from which to consider the model for cavitation, and they considerably simplify
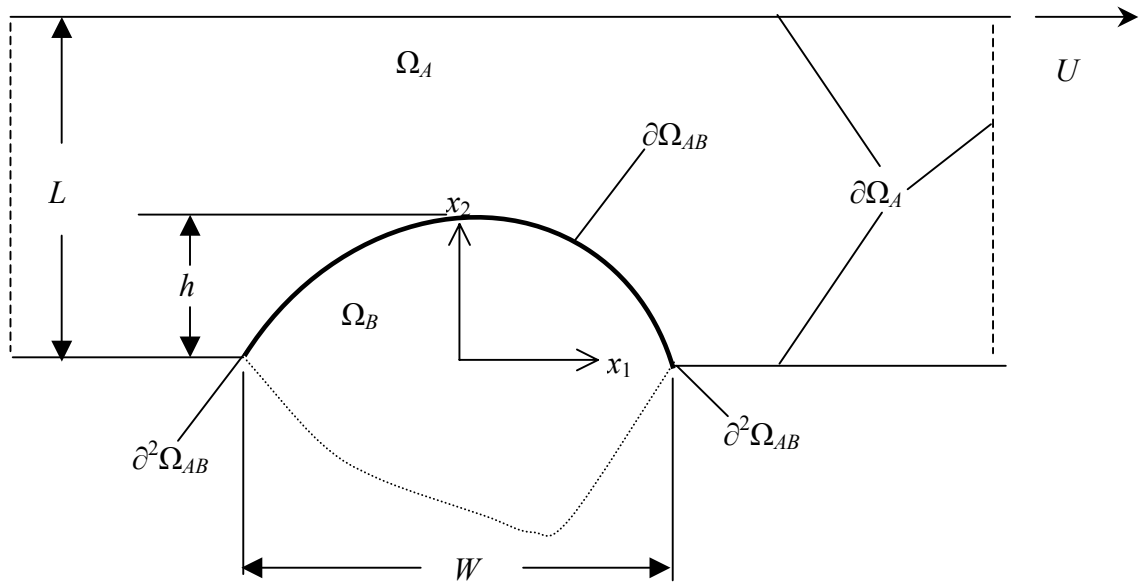
Figure 9. Two-dimensional model for inception of shear cavitation.

the solution. Also, they are close approximations whenever the time scale for bubble growth is much faster (impermeable liquid) or slower (infinite diffusion) than the time scale for diffusion of gas through the system and in or out of the bubble. These two, opposite, limiting cases will be considered.

In order to obtain some information about the role of diffusion for conditions such as those in the experiments, a third diffusion model is incorporated. This model, accurate for mass transfer from a bubble only if the system has a sufficiently high Peclet number, is the "penetration model," in which the mass transfer is calculated based upon the assumption that a quasisteady concentration boundary layer surrounds the bubble (Bird *et al*., 2002). For such a case, in dimensional variables

$$\frac{dN_B^*}{dt^*} = FD \frac{c_\infty^* - Hp_B^*}{\delta_c} S_B^*$$

(3.31)

with

$$\delta_c = S_B^* \mathrm{Pe}_{S_B^*}^{-\frac{1}{2}}$$

(3.32)

S_B^* is typically the bubble circumference, δ_c is the scale of the concentration boundary layer thickness, $\mathrm{Pe}_{S_B^*}$ is the Peclet number based on S_B^* and the maximum tangential velocity on the bubble surface u_{max}^*, and F is an order one factor that depends on the flow geometry.

When scaled, Eq. (3.31) becomes

$$\frac{dN_B}{dt} \approx \left(c_\infty - \frac{p_B}{Ci} \right) \mathrm{Pe}_L^{-\frac{1}{2}} \left(u_{max} S_B \right)^{\frac{1}{2}}$$

(3.33)

Although F generally changes with the flow geometry, it will remain order one; therefore, F is set equal to unity for calculations. Models such as Eq. (3.33) are typically

applied when the flow over the bubble is unidirectional (Bird *et al*. 2002) or symmetric (Favelukis *et al*. 1999). The situation in these simulations is more complicated as areas of recirculation can form near the trailing edge of the bubble making the boundary layer model clearly inappropriate. Therefore, the length S_B is defined as the arclength along the bubble surface from the rear contact line to the point where the tangential component of the surface velocity is zero. The dimensionless parameter c_∞ is a measure of gas saturation based on p_∞: when the liquid is saturated with gas at pressure p_∞ then c_∞ is unity. The value of c_∞ can be greater or less than one when the pressure p_∞ is not controlled by gas pressurization, or when there has been insufficient time for changes in gas pressure p_∞ to affect the amount of dissolved gas in the liquid in the vicinity of the void. The latter possibility would be the case if the time since a change in pressure, t_p, is much less than the characteristic diffusion time based on the distance from the gas liquid interface to the void L_D, i.e.,

$$t_p \ll \frac{L_D^2}{D} \tag{3.34}$$

For the experiments performed in the Couette device, the characteristic time would be approximately 10^5 s.

Figure 10 is a plot of velocity vectors in the vicinity of a deforming void from simulation, used to illustrate the penetration model. The thick portion of the bubble surface is the portion whose arclength is S_B. The dashed line shows the boundary layercorresponding to Eq. (3.32). Mass transfer from the thin line segment of the bubble's surface is neglected; it is to a region of very slowly circulating liquid and would be primarily due to diffusion.
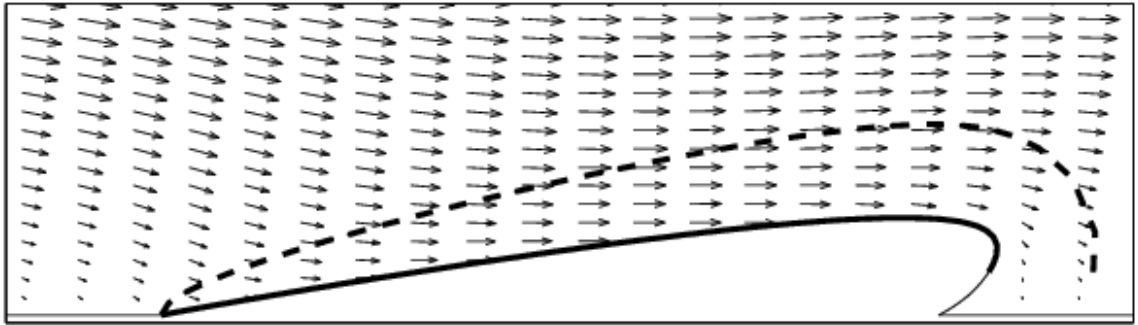
Figure 10. Velocity vectors in the vicinity of a deforming void from simulation, used to illustrate the penetration model. The arclength of the thick line is S_B. The dashed line shows the boundary layer corresponding to Eq. (3.32). Mass transfer from the thin line segment of the bubble's surface is neglected.

3.1.e Contact Line Dynamics

A contact line exists at the interface of three different phases: in the case of this work a solid, liquid, and gas phase. In the two-dimensional model, reference to the contact line is actually a reference to one of two points. DeGennes has reviewed contact line dynamics and provides a common nomenclature (deGennes 1985).   The contact angle is defined as the angle measured in the liquid at the contact line between the solid-liquid boundary ($\partial\Omega_A$) and the gas-liquid boundary ($\partial\Omega_{AB}$). The contact line is said to be advancing when the motion would cause the area of contact between the liquid and solid to increase and receding when the motion would cause the area of contact between the liquid and solid to decrease. In this work, the contact line velocity, $\mathbf{u}^*_{\mathrm{CL}}$, will always have a positive value when the contact line is advancing and a negative value when the contact line is receding.   The contact angle for a stationary contact line, $\mathbf{u}^*_{\mathrm{CL}} = 0$, can be theoretically predicted using thermodynamic arguments (deGennes 1985). Each interface has associated with it an interfacial energy per unit area, or surface tension, γ_{ij}, where the subscripts indicate the phases separated by the interface: gas G, liquid L, or solid S. At equilibrium an infinitesimally small shift (dx) in contact line position should not change the overall energy. Assuming that the contact angle is measured outside of a very small region where interfacial energies may not be constant, and that this region translates with the shift dx, i.e., its energy is unchanged, then the change in energy due to the contact line shift is

$$\gamma_{LS}dx - \gamma_{GS}dx + \gamma_{LG}dx\cos\theta = 0 \qquad (3.35)$$

or upon rearrangement,

$$\cos\theta = \frac{\gamma_{GS} - \gamma_{LS}}{\gamma_{LG}} \qquad (3.36)$$

The contact angle should only deviate from the theoretical value expressed in Eq. (3.36) when the system is not in equilibrium, i.e., is in motion. However, chemical heterogeneities and surface roughness allow the contact angle to achieve apparent equilibrium at a range of values, leading to the phenomenon of contact angle hysteresis or contact line pinning. In such cases, the contact line advances when the contact angle exceeds a certain value, the advancing contact angle, θ_A, and recedes when the contact angle falls below the receding contact angle, θ_R.

In the two dimensional model there are two contact lines: the point at the interface of the gas, liquid and solid boundary located initially at positive x_1 is called the front or leading contact line, and the other is called the rear contact line. When the contact line is located at a point where the solid surface experiences a discontinuity in slope there are two possible contact angles. Which is relevant depends upon whether the contact angle will be compared with the advancing or receding contact angle. For a contact line located at either corner between the wall and crevice, the contact angle that should be compared with the advancing contact angle is the angle between the gas-liquid interface and the crevice wall at the contact line, while the contact angle that should be compared with the receding contact angle is the angle between the gas-liquid interface and the horizontal wall surface.

The no slip assumption, Eq. (3.21), results in a non-integrable (and non-physical) singularity at the contact line due to a discontinuous velocity (Huh and Scriven 1971). Proper resolution of the contact line singularity and the development of a contact line model for incorporation into a hydrodynamic model is a continuing subject of research.

When the bulk flow is of primary interest, and details of the flow very near the contact line are not important, a successful, although ad hoc, approach is to assume that some relationship exists between the apparent dynamic contact angle and the contact line velocity (Smith 1995). Many such relationships have been proposed, based on experimental data or analyses (Blake and Haynes 1969, Hoffman 1975, Cox 1986). In the absence of experimental data specific to the geometry, materials, and flow of interest, the choice of model is somewhat arbitrary. The model developed by Hoffman was later recast in an explicit form that has been successfully used by other researchers and forms the basis of this thesis' contact line model (Jiang *et al.* 1979):

$$\frac{\cos\theta - \cos\theta_s}{\cos\theta_s + 1} = \tanh\left(4.96\, Ca_{CL}^{0.702}\right) \tag{3.37}$$

where the contact line capillary number, Ca_{CL}, is based on the contact line velocity

$$Ca_{CL} = \frac{\mu\left|\mathbf{u}_{CL}^*\right|}{\gamma} \tag{3.38}$$

Replacing the static contact angle with the appropriate choice of advancing or receding contact angle, and rewriting Eq. (3.37) for Ca_{CL} as an explicit function of the contact angle yields the model used for this work

$$Ca_{CL} = \begin{cases} -0.1018\left[\tanh^{-1}\left(\dfrac{\cos\theta_R - \cos\theta}{1 - \cos\theta_R}\right)\right]^{1.425} & \theta < \theta_R \\ 0 & \theta_R \leq \theta \leq \theta_A \\ 0.1018\left[\tanh^{-1}\left(\dfrac{\cos\theta - \cos\theta_A}{\cos\theta_A + 1}\right)\right]^{1.425} & \theta > \theta_A \end{cases} = \mathcal{H}^{-1}\left(\theta; \theta_A, \theta_R\right) \tag{3.39}$$

3.1.f Simplified Inception Model

The mathematical model that is solved in an attempt to gain insight into cavitation inception from crevice stabilized gas nuclei in a simple shear flow is a two-dimensional

model in which a liquid system and gas system are coupled. The liquid system is governed by the Stokes equations for fluid flow, Eq. (3.17), and the gas system obeys the ideal gas equation of state. The limits of infinitely fast diffusion and an impermeable liquid are considered. Alternatively, a quasisteady boundary layer model is used to approximate mass transfer. This simplified two-dimensional model is quasistatic:

$$\nabla^2 \mathbf{u} = \nabla p$$
$$\nabla \cdot \mathbf{u} = 0 \tag{3.40}$$

$$u_2 = 0 \text{ at } x_2 = 0$$
$$u_1 = 1 \text{ at } x_2 = 1 \tag{3.41}$$

$$\left. \begin{array}{l} u_2 \to 0 \\ f_n \to -Ci \end{array} \right\} \text{ as } x_1 \to \pm\infty \tag{3.42}$$

$$u_{CL} = \mathrm{Ca}_L \, \mathcal{H}^{-1}\left(\theta; \theta_A, \theta_R\right) \text{ at } \partial^2 \Omega_{AB} \tag{3.43}$$

$$f_t = 0 \text{ on } \partial\Omega_{AB} \tag{3.44}$$

$$f_n = \frac{\kappa}{\mathrm{Ca}_L} + p_B \text{ on } \partial\Omega_{AB} \tag{3.45}$$

$$p_0 = p_B\left(t = 0\right) = Ci + \frac{\kappa_o}{\mathrm{Ca}_L} \tag{3.46}$$

$$p_B = p_0 \tag{3.47}$$

or

$$p_B = \frac{A_B\left(t = 0\right)}{A_B\left(t\right)} p_0 \tag{3.48}$$

or

$$p_B = \frac{N_B(t)}{A_B\left(t\right)} \frac{A_B\left(t = 0\right)}{N_B(t = 0)} p_0 \tag{3.49}$$

The initial bubble pressure p_0 is set in Eq. (3.46) based on the initial curvature κ_0 so that the system is in mechanical equilibrium in the absence of flow.

The equation for p_B is Eq. (3.47) in the case of infinitely fast diffusion. For an impermeable liquid, the bubble pressure depends only upon the variation of the bubble

area A_B, with time, and so Eq. (3.48) applies, while Eq. (3.49) is used along with Eq. (3.33) for the penetration model. The crevice geometry is simplified to that of a triangle or trapezoid and specified using a crevice area, A_C, which is the area between the crevice walls and a horizontal line drawn across the crevice mouth, and crevice angles θ_{CL} and θ_{CR}, which are the angles between the left or right walls of the crevice and vertical.

3.2   NUMERICAL SOLUTION OF THE INCEPTION MODEL

Equations (3.40) to (3.49) are an ideal system of equations for solution via the boundary element method (BEM). The BEM is based upon an integral formulation of the governing equations and has been applied to problems involving moving interfaces in Stokes flows with considerable success (Pozrikidis 2001a). The BEM has a number of advantages, the greatest being that, for a linear, quasisteady problem such as here (with homogeneous governing equations), it reduces the dimensionality of the problem, eliminating the need to discretize the interior of domain Ω_A. This implementation of the BEM draws heavily on the published experience of researchers who used it for similar problems. Pozrikidis used the BEM to study two-dimensional bubbles in infinite shear flows (Pozrikidis 2001b and 2003). First Dimitrakopoulos and Higdon (Dimitrakopoulos and Higdon 1997) and later Schleizer and Bonnecaze (Schleizer and Bonnecaze 1999) used the BEM to look at the displacement of two-dimensional incompressible droplets from walls in shear flows.

3.2.a Theoretical Background for BEM

Fan has recently applied the BEM to difficult problems of moving interfaces in Stokes flow with advection and diffusion of species of interest (Fan 2003). He provides

an excellent and clear review of the fundamentals of the derivation of the boundary integral equation for solution of Stokes systems. To obtain this formulation, an integral representation is sought by starting with the linear differential equation system, Eq. (3.40) written more generally as

$$\mathcal{L}\mathbf{u} = 0 \tag{3.50}$$

where $\mathcal{L}$ denotes a linear differential operator with associated boundary conditions. An inverse operator is sought which is an integral operator

$$\left(\mathcal{L}^{-1}\mathbf{u}\right)(x) = \int G(x,s)u(s)ds \tag{3.51}$$

Operating on both sides of Eq. (3.51) with $\mathcal{L}$ we find that

$$\mathbf{u}(x) = \int \mathcal{L}G(x,s)u(s)ds \tag{3.52}$$

which implies

$$\mathcal{L}G(x,s) = \delta(x-s) \tag{3.53}$$

where δ is the Dirac delta function. Equation (3.53) is termed the singularly forced differential equation. The kernel function G that satisfies Eq. (3.53) is called the Green's function of the operator $\mathcal{L}$; if the operator is associated with an infinite domain, then the Green's function is called the free space Green's function, or fundamental solution.

To obtain the boundary integral representation for a two-dimensional Stokes system (Pozrikidis 1992), a form of Green's second identity known as the Lorentz reciprocal identity is used,

$$\frac{\partial}{\partial x_i}\left(u_j'\sigma_{ij} - u_i\sigma_{ij}'\right) = 0 \tag{3.54}$$

where u_i and σ_{ij} are the components of the velocity and Newtonian stress tensor for an arbitrary Stokes flow, the prime indicates any other arbitrary Stokes flow, and the normal index rules apply.

Integrating Eq. (3.54) over domain Ω and applying the divergence theorem to convert the areal integral into a line integral over $\partial\Omega$

$$\int_{\Omega} \frac{\partial}{\partial x_i}\left(u'_j\sigma_{ij} - u_i\sigma'_{ij}\right)dA = \int_{\partial\Omega}\left(u'_j\sigma_{ij} - u_i\sigma'_{ij}\right)n_i dS = 0 \tag{3.55}$$

where n_i is an inward pointing normal.

Now u' is specified in terms of the arbitrarily weighted free space Green's function for two-dimensional Stokes flow

$$u'_i(\mathbf{x}) = \frac{1}{4\pi\mu}G_{ij}(\mathbf{x},\mathbf{x}_0)b_j \tag{3.56}$$

and σ' in terms of the associated stress tensor $\mathbf{T}$

$$\sigma'_{ij} = \frac{1}{4\pi}T_{ijk}(\mathbf{x},\mathbf{x}_o)b_j \tag{3.57}$$

so that Eq. (3.55) becomes

$$\int_{\partial\Omega}\left(G_{ij}(\mathbf{x},\mathbf{x}_0)f_i(\mathbf{x}) - \mu u_i(\mathbf{x})T_{ijk}(\mathbf{x},\mathbf{x}_o)n_i(\mathbf{x})\right)dS(\mathbf{x}) = 0 \tag{3.58}$$

In Eq. (3.58) $\mathbf{f}$ is the surface traction vector, $\boldsymbol{\sigma}\cdot\mathbf{n}$. The two-dimensional free space Greens function and associated stress tensor are given by

$$\begin{aligned}
G_{ij}(\mathbf{x},\mathbf{x}_o) &= -\delta_{ij}\ln(r) + \frac{\hat{x}_i\hat{x}_j}{r^2}\\
T_{ijk}(\mathbf{x},\mathbf{x}_o) &= -4\frac{\hat{x}_i\hat{x}_j\hat{x}_k}{r^4}\\
\hat{x}_i &= x_i - x_{oi}\\
r &= \sqrt{\hat{x}_1^2 + \hat{x}_2^2}
\end{aligned} \tag{3.59}$$

Considering a domain Ω excluding only the singular point $\mathbf{x}_o$,

$$u_j(\mathbf{x}_o) = -\frac{1}{4\pi} \int_{\partial\Omega} f_i(\mathbf{x}) G_{ij}(\mathbf{x}, \mathbf{x}_o) dS(\mathbf{x}) + \frac{1}{4\pi} \int_{\partial\Omega} u_i(\mathbf{x}) T_{ijk}(\mathbf{x}, \mathbf{x}_o) n_k(\mathbf{x}) dS(\mathbf{x}) \qquad (3.60)$$

for $\mathbf{x}_0$ in the interior of Ω, and

$$u_j(\mathbf{x}_o) = -\frac{1}{2\pi} \int_{\partial\Omega} f_i(\mathbf{x}) G_{ij}(\mathbf{x}, \mathbf{x}_o) dS(\mathbf{x}) + \frac{1}{2\pi} \int_{\partial\Omega} u_i(\mathbf{x}) T_{ijk}(\mathbf{x}, \mathbf{x}_o) n_k(\mathbf{x}) dS(\mathbf{x}) \qquad (3.61)$$

for $\mathbf{x}_o$ on $\partial\Omega$ (Pozrikidis 1992). The second integral in Eq. (3.61) is interpreted in terms of the Cauchy principal value due to the presence of a singularity at $\mathbf{x} = \mathbf{x}_o$.

Equation (3.61) serves as the basis for the numerical solution of the two-dimensional Stokes flow problem via BEM. One way of conceptualizing Eq. (3.61) is that the solution is sought by finding a boundary distribution of fundamental solutions, which satisfy the governing partial differential equations. The fundamental solutions are the flows due to a point source and a stresslet. The distribution density of fundamental solutions is found that satisfies the boundary conditions. Practically speaking, the boundary is discretized and the unknown velocities and tractions are approximated as constants on each element. The boundary integral equation thus becomes a linear system of equations that is solved for the unknown velocities and tractions.

With the boundary conditions for the crevice stabilized gas nuclei problem Eq. (3.60) is a Fredholm integral equation of mixed kind, and there is no theory that allows the determination of uniqueness or existence of solution (Powers and Wrobel 1995). Uniqueness of solution is an important question because the related problem of a free, compressible, inviscid bubble in a shear flow, if solved using Eq. (3.60), does not have a unique solution (Pozrikidis 2001b). Practically speaking, non-uniqueness results in an ill conditioned matrix when the integral equation is discretized, and the condition number will become larger as the number of elements is increased. This suggests a non-rigorous

method to check the uniqueness of solution via monitoring matrix condition number. For the problem of the deformation of an inviscid bubble attached to a wall, the matrices do not have the ill conditioned nature indicative of a non-unique solution (Figure 11). However, non-uniqueness of solution precludes the use of the BEM simulation program to investigate the fate of any bubbles shed from the nucleation site.

3.2.b Discretization for BEM

The boundary integral equation, Eq. (3.61) is used to construct the boundary element formulation. The boundary is separated into segments based on the boundary conditions. For this model, there are four combinations of boundary conditions:

a) velocities specified as zero (lower solid boundaries).

b) velocities specified, $u_1 = 1$, $u_2 = 0$, (upper solid boundary),

c) tractions specified (interface), and

d) one velocity (u_2) and one traction (f_1) specified (inlet and outlet).

The boundary integrals are split into a sum of integrals over the three different types of boundaries, so that Eq. (3.61) is rewritten as
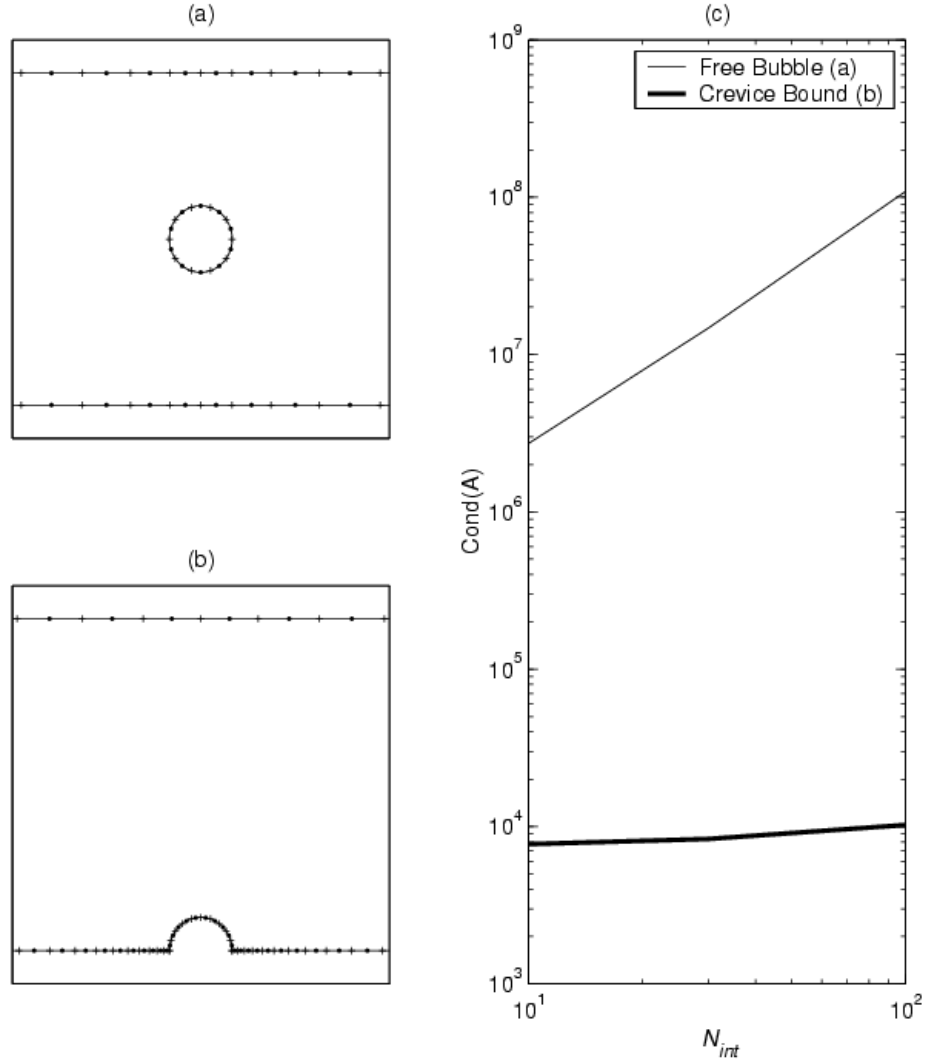
Figure 11. Plots demonstrating the numerical check on uniqueness of solution of the integral equation representation Eq. (3.61) for a 2-D inviscid compressible bubble attached to a wall (b). The condition number of the matrix A resulting from discretization of Eq. (3.61) is compared to the condition number for the case of a 2-D free compressible bubble (a). The plots (a) and (b) show only the central portion of the domains, and demonstrate typical locations of collocation points (dots). For the non-unique free bubble case, the condition number increases as the number of elements in the interface N_{int} is increased.

$$-\int_a f_1(\mathbf{x})G_{1j}(\mathbf{x},\mathbf{x}_o)dS(\mathbf{x})-\int_a f_2(\mathbf{x})G_{2j}(\mathbf{x},\mathbf{x}_o)dS(\mathbf{x})$$

$$-\int_b f_1(\mathbf{x})G_{1j}(\mathbf{x},\mathbf{x}_o)dS(\mathbf{x})-\int_b f_2(\mathbf{x})G_{2j}(\mathbf{x},\mathbf{x}_o)dS(\mathbf{x})$$

$$+\int_c u_1(\mathbf{x})T_{1j1}(\mathbf{x},\mathbf{x}_o)n_1(\mathbf{x})dS(\mathbf{x})+\int_c u_2(\mathbf{x})T_{2j1}(\mathbf{x},\mathbf{x}_o)n_1(\mathbf{x})dS(\mathbf{x})$$

$$+\int_c u_1(\mathbf{x})T_{1j2}(\mathbf{x},\mathbf{x}_o)n_2(\mathbf{x})dS(\mathbf{x})+\int_c u_2(\mathbf{x})T_{2j2}(\mathbf{x},\mathbf{x}_o)n_2(\mathbf{x})dS(\mathbf{x})$$

$$+\int_d u_1(\mathbf{x})T_{1jk}(\mathbf{x},\mathbf{x}_o)n_k(\mathbf{x})dS(\mathbf{x})-\int_d f_2(\mathbf{x})G_{2j}(\mathbf{x},\mathbf{x}_o)dS(\mathbf{x})$$

$$=2\pi u_j(\mathbf{x}_o)+\int_b T_{1j2}(\mathbf{x},\mathbf{x}_o)n_2(\mathbf{x})dS(\mathbf{x})$$

$$+\int_c f_1(\mathbf{x})G_{1j}(\mathbf{x},\mathbf{x}_o)dS(\mathbf{x})+\int_c f_2(\mathbf{x})G_{2j}(\mathbf{x},\mathbf{x}_o)dS(\mathbf{x})$$

$$-\int_d CiG_{1j}(\mathbf{x},\mathbf{x}_o)dS(\mathbf{x})$$

(3.62)

where the integrals are over the segments with boundary conditions specified as above, which have been inserted where convenient. The terms on the left hand side of Eq. (3.62) are unknown, the first term on the right hand side will be known or unknown depending upon the location of the collocation point $\mathbf{x}_o$, and the remaining terms on the right hand side are known. Note that Eq. (3.62) is really two equations, one each for j equal to one or to two. Next each segment of the boundaries is discretized and the unknowns are approximated as constants over each discrete interval

48

$$-\sum_{n=1}^{N_a}\left\{f_1^{a,n}\int_{a_n}G_{1j}\left(\mathbf{x},\mathbf{x}_o\right)dS\left(\mathbf{x}\right)-f_2^{a,n}\int_{a_n}G_{2j}\left(\mathbf{x},\mathbf{x}_o\right)dS\left(\mathbf{x}\right)\right\}$$

$$-\sum_{n=1}^{N_b}\left\{f_1^{b,n}\int_{b_n}G_{1j}\left(\mathbf{x},\mathbf{x}_o\right)dS\left(\mathbf{x}\right)-f_2^{b,n}\int_{b_n}G_{2j}\left(\mathbf{x},\mathbf{x}_o\right)dS\left(\mathbf{x}\right)\right\}$$

$$+\sum_{n=1}^{N_c}\left\{u_1^{c,n}\left[\int_{c_n}T_{1j1}\left(\mathbf{x},\mathbf{x}_o\right)n_1\left(\mathbf{x}\right)dS\left(\mathbf{x}\right)+\int_{c_n}T_{1j2}\left(\mathbf{x},\mathbf{x}_o\right)n_2\left(\mathbf{x}\right)dS\left(\mathbf{x}\right)\right]\right\}$$

$$+\sum_{n=1}^{N_c}\left\{u_2^{c,n}\left[\int_{c_n}T_{2j1}\left(\mathbf{x},\mathbf{x}_o\right)n_1\left(\mathbf{x}\right)dS\left(\mathbf{x}\right)+\int_{c_n}T_{2j2}\left(\mathbf{x},\mathbf{x}_o\right)n_2\left(\mathbf{x}\right)dS\left(\mathbf{x}\right)\right]\right\}$$

$$+\sum_{n=1}^{N_d}\left\{u_1^{d,n}\int_{d_n}T_{1jk}\left(\mathbf{x},\mathbf{x}_o\right)n_k\left(\mathbf{x}\right)dS\left(\mathbf{x}\right)-f_2^{d,n}\int_{d_n}G_{2j}\left(\mathbf{x},\mathbf{x}_o\right)dS\left(\mathbf{x}\right)\right\}$$

$$=2\pi u_j\left(\mathbf{x}_o\right)+\int_b T_{1j2}\left(\mathbf{x},\mathbf{x}_o\right)n_2\left(\mathbf{x}\right)dS\left(\mathbf{x}\right)$$

$$+\sum_{n=1}^{N_c}\left\{f_1^{c,n}\int_{c_n}G_{1j}\left(\mathbf{x},\mathbf{x}_o\right)dS\left(\mathbf{x}\right)+f_2^{c,n}\int_{c_n}G_{2j}\left(\mathbf{x},\mathbf{x}_o\right)dS\left(\mathbf{x}\right)\right\}$$

$$-Ci\int_d G_{1j}\left(\mathbf{x},\mathbf{x}_o\right)dS\left(\mathbf{x}\right)$$

(3.63)

The known tractions on the interface, segment *c*, are split up due to the description of the interface as a cubic spline to be described later; the other integrals involving known quantities can be evaluated analytically.

Equation (3.63) is evaluated twice, once for each direction *j*, at collocation points $\mathbf{x}_o$ selected as the midpoints of each discrete interval. This yields the same number of equations as there are unknowns; the system is linear and can be written simply as

$$A\mathbf{y}=\mathbf{d} \tag{3.64}$$

where A is a full 2N by 2N matrix, $N = N_a + N_b + N_c + N_d$. The solution of Eq. (3.64) is found by LU decomposition, except when the condition number of A is sought during investigations of uniqueness of solution; in those cases, singular value decomposition is used.

3.2.c Discrete interval integrations

Several issues must be considered for construction of the matrix A in Eq. (3.64) from Eq. (3.63). They are divided into the areas of mathematical description of the interface and integrations near singular points.

The interface, $\partial\Omega_{AB}$, or segment c, is described parametrically. Each discrete interval is described using cubic parametric equations, where the variable of parameterization is the polygonal arclength p along the interval; for each interval coefficients are found for

$$x = b_1\mathrm{p}^3 + b_2\mathrm{p}^2 + b_3\mathrm{p} + b_4$$
$$y = c_1\mathrm{p}^3 + c_2\mathrm{p}^2 + c_3\mathrm{p} + c_4$$

(3.65)

The coefficients are found so that the description of the interface is a cubic spline. At each interval endpoint, the first and second derivatives of $x(\mathrm{p})$ and $y(\mathrm{p})$ with respect to p are therefore continuous. Because the interface is not closed, two more conditions are required. The "not-a-knot" spline gives the most naturally varying curvatures. Therefore, at the first interior points from the contact lines the third derivatives are also forced to be continuous.

The collocation points $\mathbf{x}_o$ on the interface are the midpoints based on true arclength s

$$s_o = s\left(\mathrm{p}_o\right) = \int_0^{\mathrm{p}_o} \sqrt{\left(\frac{dx}{d\mathrm{p}}\right)^2 + \left(\frac{dy}{d\mathrm{p}}\right)^2}\, d\mathrm{p} = \frac{1}{2}\int_0^{\mathrm{p}_n} \sqrt{\left(\frac{dx}{d\mathrm{p}}\right)^2 + \left(\frac{dy}{d\mathrm{p}}\right)^2}\, d\mathrm{p}$$

(3.66)

where p_n is the polygonal arclength of the interval and $\mathbf{x}_o = [x(\mathrm{p}_o), y(\mathrm{p}_o)]$.

The "known" tractions on the right hand side of Eq. (3.63) are calculated using Eq. (3.45) with the curvature calculated at $\mathbf{x}_o$, where the curvature κ is calculated using

$$\kappa = \frac{\dfrac{dy}{d\mathrm{p}}\dfrac{d^2x}{d\mathrm{p}^2} - \dfrac{dx}{d\mathrm{p}}\dfrac{d^2y}{d\mathrm{p}^2}}{\left[\left(\dfrac{dx}{d\mathrm{p}}\right)^2 + \left(\dfrac{dy}{d\mathrm{p}}\right)^2\right]^{\frac{3}{2}}}\Bigg|_{\mathrm{p}=\mathrm{p}_o} \tag{3.67}$$

Also needed are the components of the unit normal vector **n** at arbitrary p

$$n_1(\mathrm{p}) = -\frac{\dfrac{dy}{d\mathrm{p}}}{\sqrt{\left(\dfrac{dx}{d\mathrm{p}}\right)^2 + \left(\dfrac{dy}{d\mathrm{p}}\right)^2}}, n_2(\mathrm{p}) = \frac{\dfrac{dx}{d\mathrm{p}}}{\sqrt{\left(\dfrac{dx}{d\mathrm{p}}\right)^2 + \left(\dfrac{dy}{d\mathrm{p}}\right)^2}} \tag{3.68}$$

The integrals in Eq. (3.63) along section c are evaluated numerically. The integrals are in terms of the variable of parameterization p

$$\int_{c_n} g(\mathbf{x},\mathbf{x}_o)dS(\mathbf{x}) = \int_0^{\mathrm{p}_n} g(x(\mathrm{p}),y(\mathrm{p}),\mathbf{x}_o)\sqrt{\left(\frac{dx}{d\mathrm{p}}\right)^2 + \left(\frac{dy}{d\mathrm{p}}\right)^2}\,d\mathrm{p} \tag{3.69}$$

where $g(\mathbf{x},\mathbf{x}_o)$ can be either G_{ij} or $T_{ijk}\,n_k$. When the interval being integrated over does not contain, nor is it near, point $\mathbf{x}_o$, this integral is evaluated using Gauss-Legendre quadrature with 12 points. This straightforward numerical integration can also be used for calculating the Cauchy principal value when $\mathbf{x}_o$ lies on the interval of integration for $g(\mathbf{x},\mathbf{x}_o) = T_{ijk}\,n_k$ (Pozrikidis 2002). This is due to fact that as the integration point $\mathbf{x}$ approaches the collocation point $\mathbf{x}_o$, the orthogonality of $\mathbf{x}$-$\mathbf{x}_o$ and **n** prevents the appearance of a singularity.

When $g(\mathbf{x},\mathbf{x}_o) = G_{jj}$ and $\mathbf{x}_o$ lies on the interval of integration then a logarithmic singularity exists that must be dealt with correctly (Pozrikidis 2002). The second term in the integral does not have a singularity and can be handled normally. For the straight intervals a, b and d the singular integral can be analytically evaluated. For the interface, the integration of the singular term is performed as follows:

51

$$\int_0^{p_n} \ln \sqrt{(x(p)-x(p_o))^2 + (y(p)-y(p_o))^2} \left[\left(\frac{dx}{dp}\right)^2 + \left(\frac{dy}{dp}\right)^2\right]^{\frac{1}{2}} dp$$

$$= \int_0^{p_n} \ln|\mathbf{x}(p)-\mathbf{x}(p_o)|h(p)\,dp \tag{3.70}$$

$$= \int_0^{p_n} \ln\left[\frac{|\mathbf{x}(p)-\mathbf{x}(p_o)|}{|p-p_o|}\right]h(p)\,dp + \int_0^{p_n} \ln|p-p_o|h(p)\,dp$$

The first integral in the last line is non-singular and can be integrated with Gauss-Legendre quadrature. The second integral is computed as follows:

$$\int_0^{p_n} \ln|p-p_o|h(p)\,dp = \int_0^{p_o} \ln|p-p_o|h(p)\,dp + \int_{p_o}^{p_n} \ln|p-p_o|h(p)\,dp$$

$$= \int_0^{p_o} \ln(\eta)h(p_o-\eta)\,d\eta + \int_0^{p_n-p_o} \ln(\eta)h(p_o+\eta)\,d\eta \tag{3.71}$$

Each integral now has the singularity at one end and they are handled similarly:

$$\int_0^{p_o} \ln(\eta)h(p_o-\eta)\,d\eta = p_o \int_0^1 \ln(\xi p_0)h(p_o-\xi p_0)\,d\xi$$

$$= p_o \ln(p_0)\int_0^1 h(p_o-\xi p_0)\,d\xi + p_o \int_0^1 \ln(\xi)h(p_o-\xi p_0)\,d\xi \tag{3.72}$$

Again, the first integral is non-singular and is integrated with Gauss-Legendre quadrature. The second integral is now of the form

$$\int_0^1 \ln(\xi)\varphi(\xi) \tag{3.73}$$

for which an accurate Gauss quadrature has been developed (Stroud 1966).

When the interface has deformed considerably, it is possible for portions of the interval over which integration is being performed to come close to point $\mathbf{x}_o$ even though $\mathbf{x}_o$ does not lie on the interval; in such cases, the integral is non-singular but more points are needed for accurate quadrature (Schleizer and Bonnecaze 1999). The number of points needed depends upon the nearness of the interval to the singular point. The

inaccuracy is avoided by using an adaptive trapezoidal integration for any non-singular element which contains a point **x**:

$$\left| \mathbf{x} - \mathbf{x}_o \right| < s\left(\mathrm{p}_n \right) \tag{3.74}$$

The velocities on the interface are used to advance the interface position in time, using an adaptive second order Runge-Kutta time integration method (Stoer and Bulirsch 1991). For the impermeable liquid and penetration model, the pressure in the bubble is updated as the interface position changes. The velocities at the contact lines during the time stepping are determined from the contact angles and Eq. (3.43), and therefore do not appear explicitly in the integral formulation.

For the impermeable liquid model and penetration model for mass transfer, the pressure in the bubble must be computed at each time step based on the new bubble cross sectional area, and, for the penetration model, based on the number of moles of gas in the bubble. The area is found by explicit integration, using the parametric description of the interface.

3.2.d Further interface discretization, advection and stability issues

The interface location evolves in time according to Eq. (3.25). Tangential motion of a point in the interface does not alter the interface shape. But using Eq. (3.25) to advect the Lagrangan marker points that define the interface will lead to clustering of the points. Because the interface is assumed to be massless and have uniform properties (i.e., surfactant free), Eq. (3.25) can be replaced by

$$\frac{d\mathbf{x}_{\partial\Omega_{AB}}}{dt} = \left(\mathbf{u} \cdot \mathbf{n} \right)\mathbf{n} \text{ on } \partial\Omega_{AB} \tag{3.75}$$

In other words, the interface can be advected using only the normal component of velocity. Using Eq. (3.75) in place of Eq. (3.25) reduces the tendency of points to cluster

but does not eliminate it. Eventually there will be regions of interface dense with short segments and others sparsely populated with long segments. This tendency of the interface marker points to cluster is eliminated by redistribution after each time step.

A choice must be made when redistributing interface points. There are two logical criteria: the points can be redistributed so that the arclength of each segment is the same, or the points can be redistributed so that the angle α subtended by each segment is the same. Each has its advantages. Initially the second choice seems preferable. It leads to clustering in areas of high curvature, which is desirable due to the need for accurate calculations of curvature in these areas. However, experience with boundary element methods has shown that for interfaces discretized with unequal segment lengths, a sawtooth instability appears (Kropinski 2001). The sawtooth instability is typically countered through the application of a smoothing algorithm (Longuet-Higgins and Cokelet 1976). It would be preferable to avoid smoothing because it essentially adds a small amount of artificial surface tension; in this regard, it is analogous to the use of artificial dissipation (viscosity) in computational fluid dynamics to combat odd-even decoupling.

For these simulations a compromise approach was used. Initially, as the interface deforms, points are added and then the endpoints are redistributed so that equal arclengths are maintained without allowing the largest subtended angle to exceed some threshold value, typically 0.3 radians:

$$\alpha_n = \kappa_n\left(p_o\right)s_n \leq \alpha_{\max} \tag{3.76}$$

For many simulations this approach could be used throughout; however, for simulations with large deformations or formation of cusp-like (extremely high curvature) regions, this

approach eventually requires an inordinate number of points in the interface, resulting in inordinately slow simulations. So another threshold value was chosen, this time for the maximum number of elements allowed in the interface. Good resolution of high curvature regions and acceptable simulation speed were obtained by making the maximum number of elements 150. Once this threshold is reached, the redistribution strategy switches. The arclength of the element with the highest curvature is set so that the subtended angle of that element is α_{max}. Then redistribution is performed so that the arclength of each element is χ times the arclength of the element before it, moving away from the highest curvature element. The numbers of elements to either side of the highest curvature element are selected so that the arclengths of the longest element on each side are nearly equal and the total number of elements used for the interface is the threshold value.

Once the redistribution strategy switches, the element arclengths in the interface are no longer uniform and smoothing must be incorporated to avoid sawtooth instability. The smoothing algorithm is based on one used in BEM simulations of breaking waves (Longuet-Higgins and Cokelet 1976). Figure 12 demonstrates the stretched (non-uniform) discretization for a representative simulation as well as the effect of neglecting to use a smoothing algorithm when the stretched discretization is used.

3.3   INCEPTION SIMULATION RESULTS

The results of simulations allowed to progress to steady state conditions are compared to those of Feng and Basaran, who used a finite element method to find steady solutions for bubbles with a specified final cross sectional area (Feng and Basaran 1994).
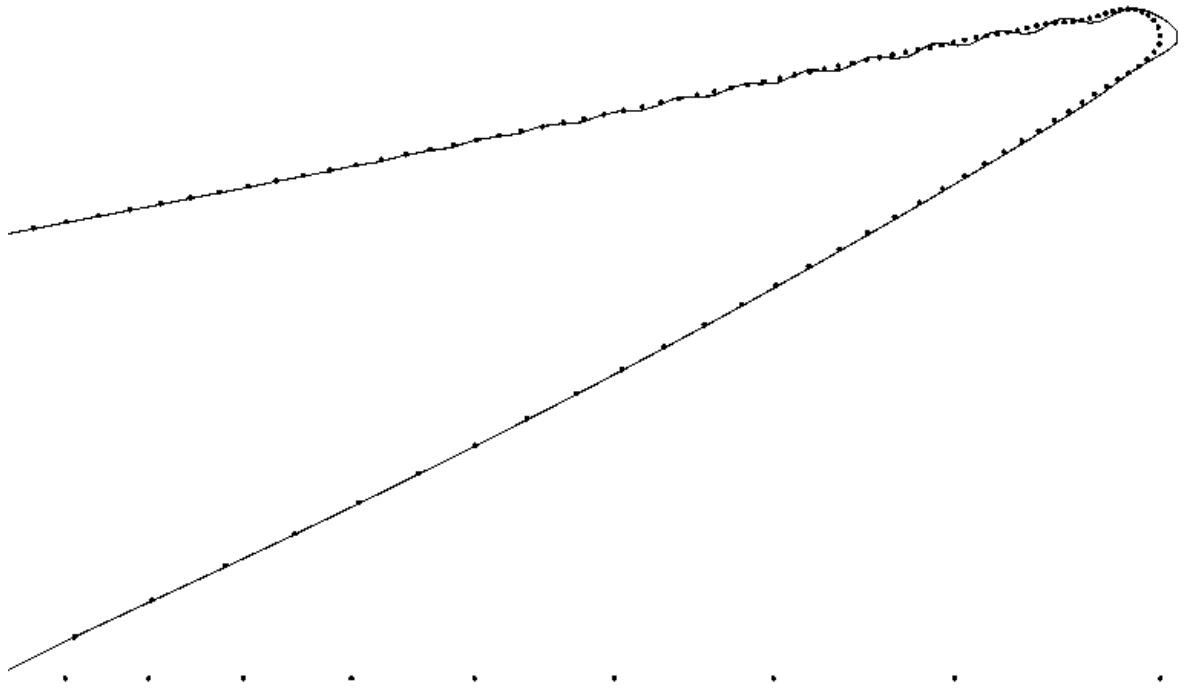
Figure 12. Demonstration of non-uniform discretization once the maximum number of interface elements has been reached. The figure shows the tip of the bubble during a representative simulation, as well as a portion of the boundary. The dots are segment endpoints from a simulation for which smoothing was used once non-uniform length elements were allowed. The line shows the effect of the sawtooth instability; it is the interface position if no smoothing were incorporated.

The interface shapes are shown in Figure 13 for comparison with their Figure 5, and the close agreement is used to validate the BEM computer code.

To determine whether a two dimensional model of inception from wall stabilized nuclei agrees with the experimental results, simulations are performed in the range of Ca_L corresponding to experimental conditions ($Ca_L \sim 30$–300 for PB), for Ci near unity. Because no gas nuclei could be observed in the experiments prior to shearing, the dimensionless crevice width, W, is limited to a maximum of 0.2 (10 μm crevices). For the magnification and resolution of the lens and camera used in the experiments, 10 μm corresponds to 5 pixels, which was assumed to be the maximum sized void that would not be detected.

3.3.a Representative simulations

For the case of infinitely fast diffusion, if the liquid is saturated then the initial curvature κ_o of the interface will be zero. Simulations with zero initial curvature for an interface with contact lines on the crevice corners show that the interface is stable to shear for any Ca_L, Ci and W; the normal component of the velocity is zero everywhere on the interface. The mass transfer model does not matter in this case provided the liquid is saturated; the interface does not deform if $\kappa_o = 0$.

If the liquid is undersaturated, simulations incorporating mass transfer have an initially negative curvature. If the liquid is supersaturated, simulations incorporating mass transfer have an initially positive curvature. Impermeable liquid case can have anyinitial curvature. Figure 14 shows interface positions for various times for two simulations, one of infinitely fasr diffusion with $\kappa_o < 0$ (undersaturated), and one for a case of no diffusion with $\kappa_o < 0$. The main result in Figure 14 is general for all permutations of
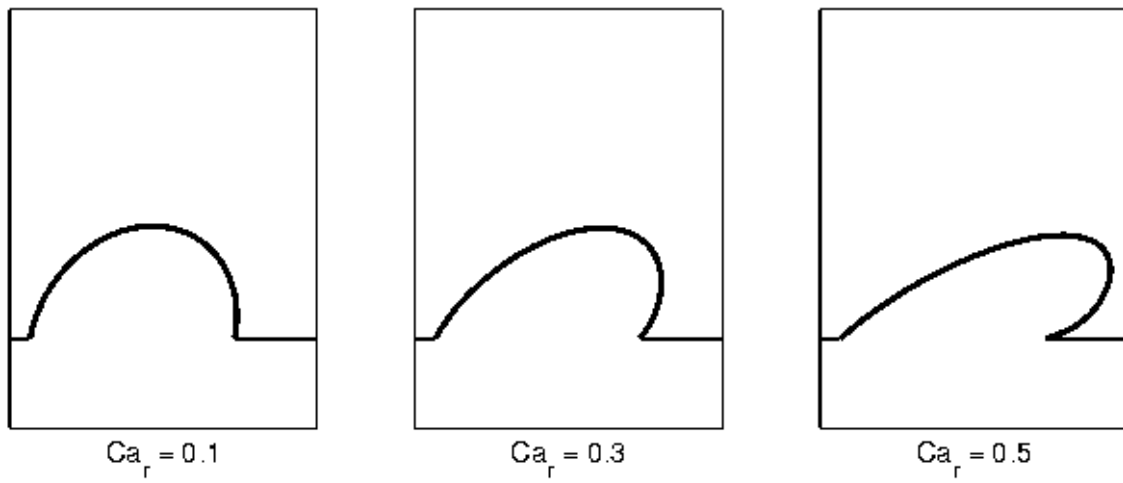
Figure 13. Steady state shapes for initially semicircular bubbles. With $Ci = 1000$ the bubble area stays nearly constant; hence the shapes can be compared with the results of Feng and Basarn (Feng and Basaran 1994). $Ca_r = Ca\ (W/2)$ is the capillary number based on the initial bubble radius.

the other parameters investigated with $\kappa_o<0$; a bubble with an initially negatively curved interface will not escape the crevice. This is a very important result. The crevice model for nuclei stabilization typically uses the fact that a crevice can cause a bubble to achieve a negative curvature to explain nuclei persistence. If all crevice stabilized gas nuclei interfaces have negative curvatures, then the most obvious conclusion must be that either the cavitation observed in the experiments does not originate from wall-crevice stabilized nuclei, or the two dimensional model can not capture the relevant physics. There is, however, another reasonable conclusion, which is that the experimentally observed cavitation together with the results in Figure 14 suggests that gas nuclei in wall-crevices can persist for long periods of time with a positive interface curvature. This agrees with the nucleation site stabilization model proposed by Mørch (Mørch 2000). We present an alternate explanation in a following section (3.4) for the persistence of nuclei with positive curvature. The remainder of this work assumes that such nuclei are present.

Figure 15 shows interface positions for various times for the case of infinitely fast diffusion with $\kappa_o>0$ (supersaturated), Figure 16 shows interface positions for an impermeable liquid with $\kappa_o>0$, and Figure 17 shows interface positions for a penetration model with supersaturated liquid conditions, $\kappa_o>0$. All three simulation results exhibit common characteristics. Initially, the bubbles are compressed and the bubble area decreases. This is similar to the behavior exhibited by a free two-dimensional bubble in an infinite shear flow (Pozrikidis 2001b). For the case of infinitely fast diffusion, the pressure does not increase during this period of compression; therefore, there is less resistance to compression and the reduction in area is greater. Furthermore, for the case of infinitely fast diffusion, the bubble exhibits a cusp or near cusp at later times ($t>1$).
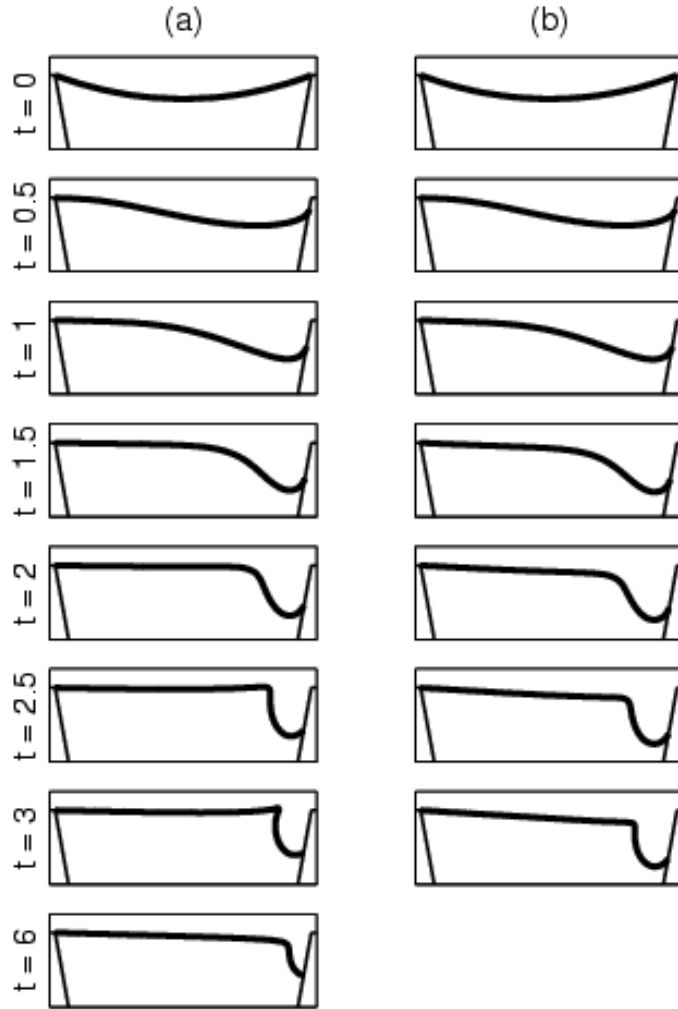
Figure 14. Simulations of interface deformation from initially negative curvature for infinitely fast diffusion (a) and impermeable liquid (b). For both (a) and (b) κ_o = -5, Ca$_L$ = 150, Ci = 1, W = 0.1, θ_{CL} = $\pi/12$, θ_{CR} = $\pi/12$, A_C = 1.87 x 10^{-3}, θ_A = 2$\pi/3$, and θ_R = $\pi/2$. No combination of these parameters was found for which an initially negatively curved interface escaped the crevice.
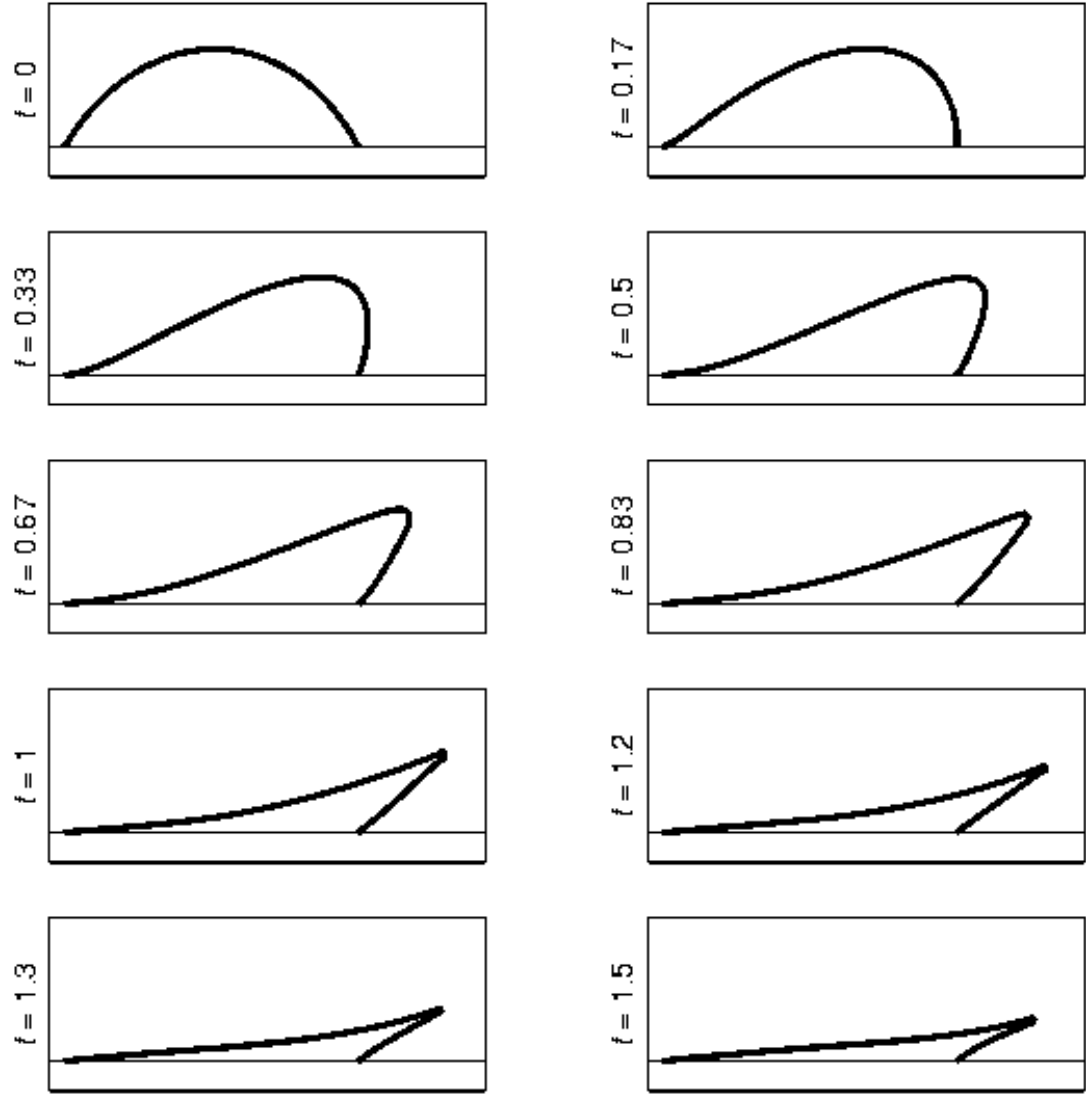
Figure 15. Interface positions at intervals of $t = 1/6$ for a simulation with $Ca_L = 100$, $Ci = 1$, $W = 0.1$ and $\kappa_0 = 16$. The mass transfer model is infinitely fast diffusion and the contact lines are pinned.

Such cusps may have a role in production of tip streaming bubbles (Rallison 1984; de Bruijn 1993). Tip streaming is not a well-understood phenomenon. As will be seen shortly, the impermeable liquid case, for the same conditions, will lead to a prediction of bubble shedding due to pinch-off. Diffusion can therefore play one of two roles in the shedding of bubbles from nucleation sites in shear: either it inhibits it, or it shifts the mechanism from pinch-off to tip streaming, leading to smaller shed bubbles.

Examination of the interface shapes for the impermeable liquid case, Figure 16, shows that by $t = 4.3$ the bubble has deformed considerably and two opposing sides have come into contact at a "pinch-off" point. It can be assumed that by this time a portion of the bubble downstream of the pinch-off point will have detached, becoming a free bubble. Absent any diffusion, the portion of the bubble that remains will achieve a steady state shape. Only one bubble will be shed. Even when the impermeable liquid model is appropriate for simulating the shedding of a bubble, diffusion may still be important in later bubble growth, as the time scale for the subsequent bubble growth could be considerably longer than the time scale for the shedding process. The BEM simulation in this thesis cannot be used to investigate the fate of shed bubbles due to previously mentioned problems with non-uniqueness of solution for free bubbles. The fate of shed bubbles is discussed in the section on bubble migration and growth (3.5).

Several of the parameters for the simulation in Figure 16 are set to their baseline or standard values so that the effect of varying these parameters on inception can be investigated. The standard value for the cavitation index, Ci, is one, for the crevice width, W, is 0.1, and for the crevice cross sectional area, A_C, is zero. The baseline model for mass transfer is the impermeable liquid model, and the baseline contact line
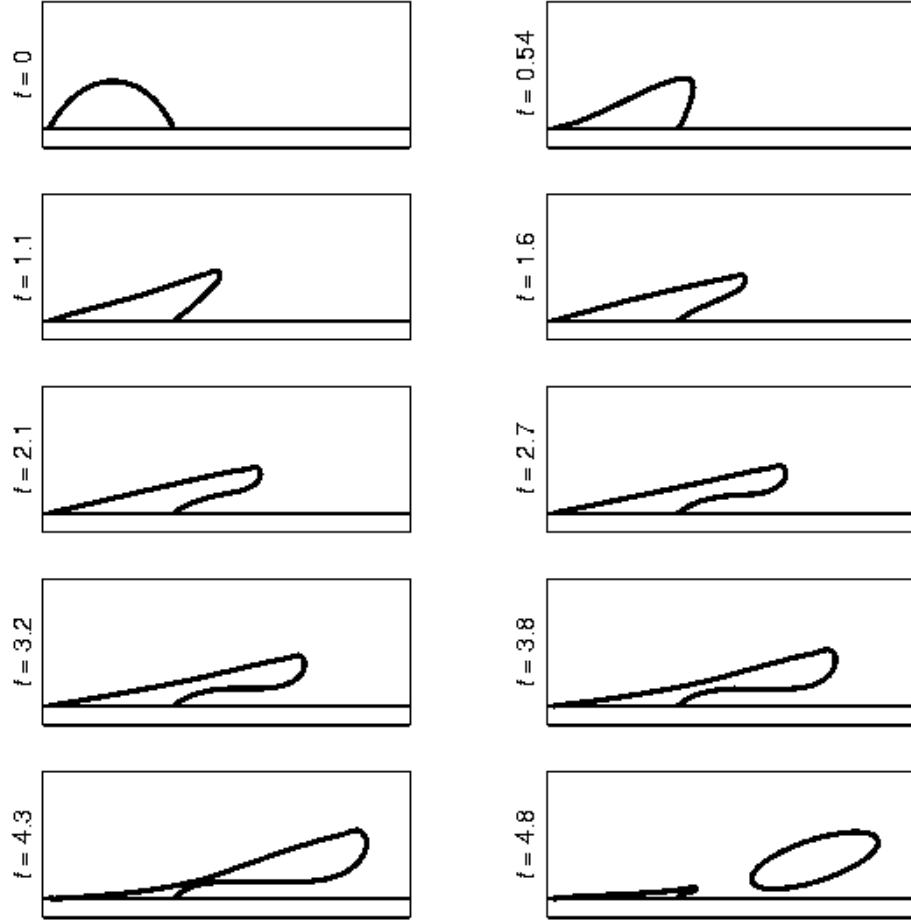
Figure 16. Interface positions at successive times *t* for a simulation with Ca$_L$ = 100, *Ci* = 1, *W* = 0.1 and κ_0 = 16 for the case of an impermeable liquid (no diffusion). The contact lines are pinned and the crevice cross sectional area A_c is zero. At *t* = 4.3 the interface touches itself and the bubble is assumed to "pinch off" at the point of contact. The shed portion of the bubble is not included in later times for the inception simulations using the BEM. The elliptical shed bubble in the last frame is included for illustration for the section on bubble migration and growth.

parameters are pinned contact lines ($\theta_A = \pi$, $\theta_R = 0$).

Figure 17 shows interface shapes for a case in which mass transport is simulated using the penetration model. For this simulation, the initial conditions and parameters not related to mass transport are the same as those for the simulations depicted in the previous two simulations (infinitely fast diffusion and impermeable liquid models, respectively). The parameter that describes the level of saturation of dissolved gas in the liquid c_∞ is chosen for this simulation so that the initial curvature is stable

$$c_\infty = 1 + \frac{\kappa_o}{Ci\mathrm{Ca}_L} \tag{3.77}$$

The Peclet number Pe_L is related to the capillary number Ca_L

$$\mathrm{Pe}_L = \mathrm{Ca}_L \frac{L\gamma}{\mu D} \tag{3.78}$$

For the simulation in Figure 17 the Pe_L is 1000, which is at the high end of its range for the experiments with the Couette viscometer.

For the times shown in Figure 17 the deformation of the interface is very similar to that in Figure 16. Pinch-off occurs slightly later and the shed bubble is a little smaller, in keeping with the inhibiting effect of diffusion on pinch-off. The same simulation is depicted in Figure 18 over a longer range of times. Whereas for the impermeable liquid model case depicted in Figure 16, only a single shedding event occurs, and for the infinitely fast diffusion case in Figure 15 no bubble is shed, Figure 18 shows that for boundary layer type mass transfer in a supersaturated gas-liquid solution, multiple bubbles may be shed. Mass transfer generally increases the level of shear necessary for shedding to occur; however, it is necessary for continual repeated shedding to occur.
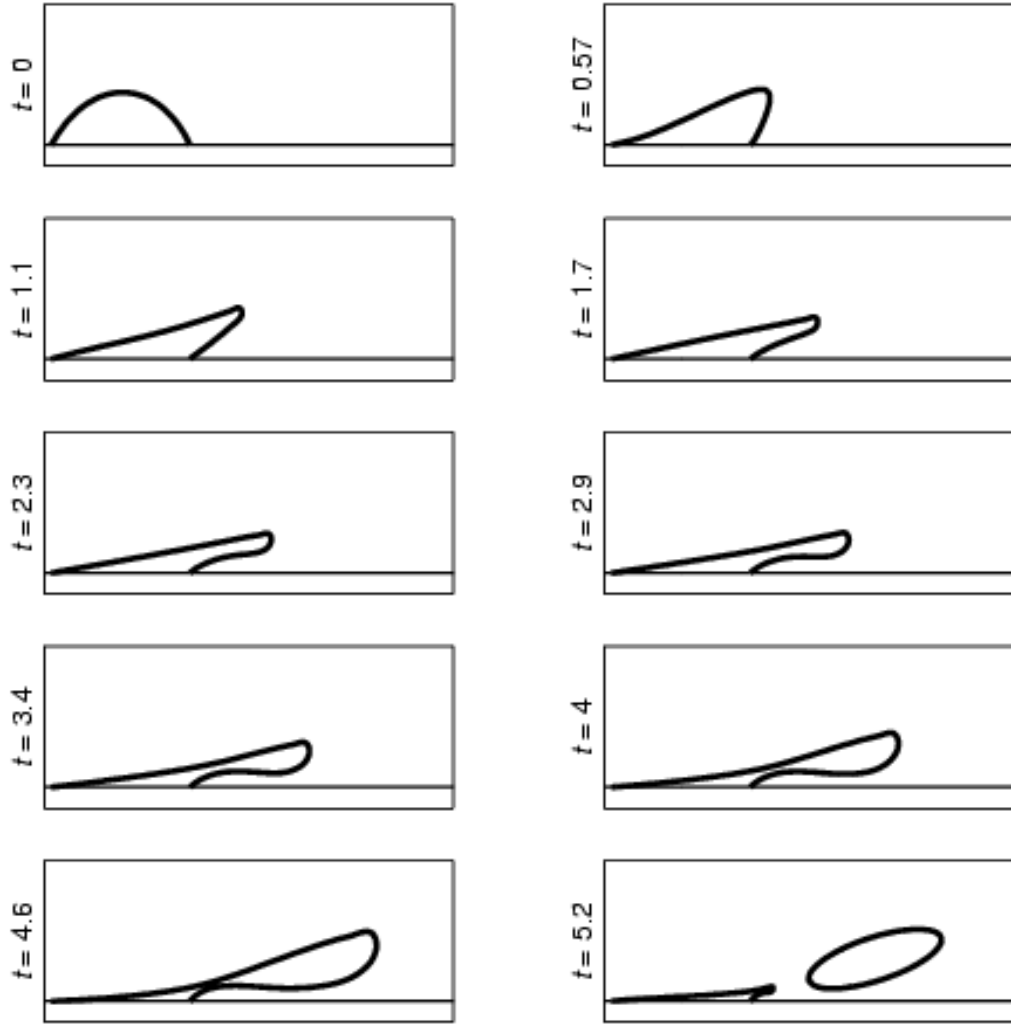
Figure 17. Interface positions at successive times *t* for a simulation with Ca_{*L*} = 100, *Ci* = 1, *W* = 0.1 and κ_o = 16 using the penetration model for mass transfer, c_∞ = 1.16 and Pe_{*L*} = 1000. The contact lines are pinned and the crevice cross sectional area A_C is zero. At *t* = 4.6 the interface touches itself and the bubble is assumed to "pinch off" at the point of contact. The shed portion of the bubble is not included in later times for the inception simulations using the BEM. The elliptical shed bubble in the last frame is included for illustration for the section on bubble migration and growth.
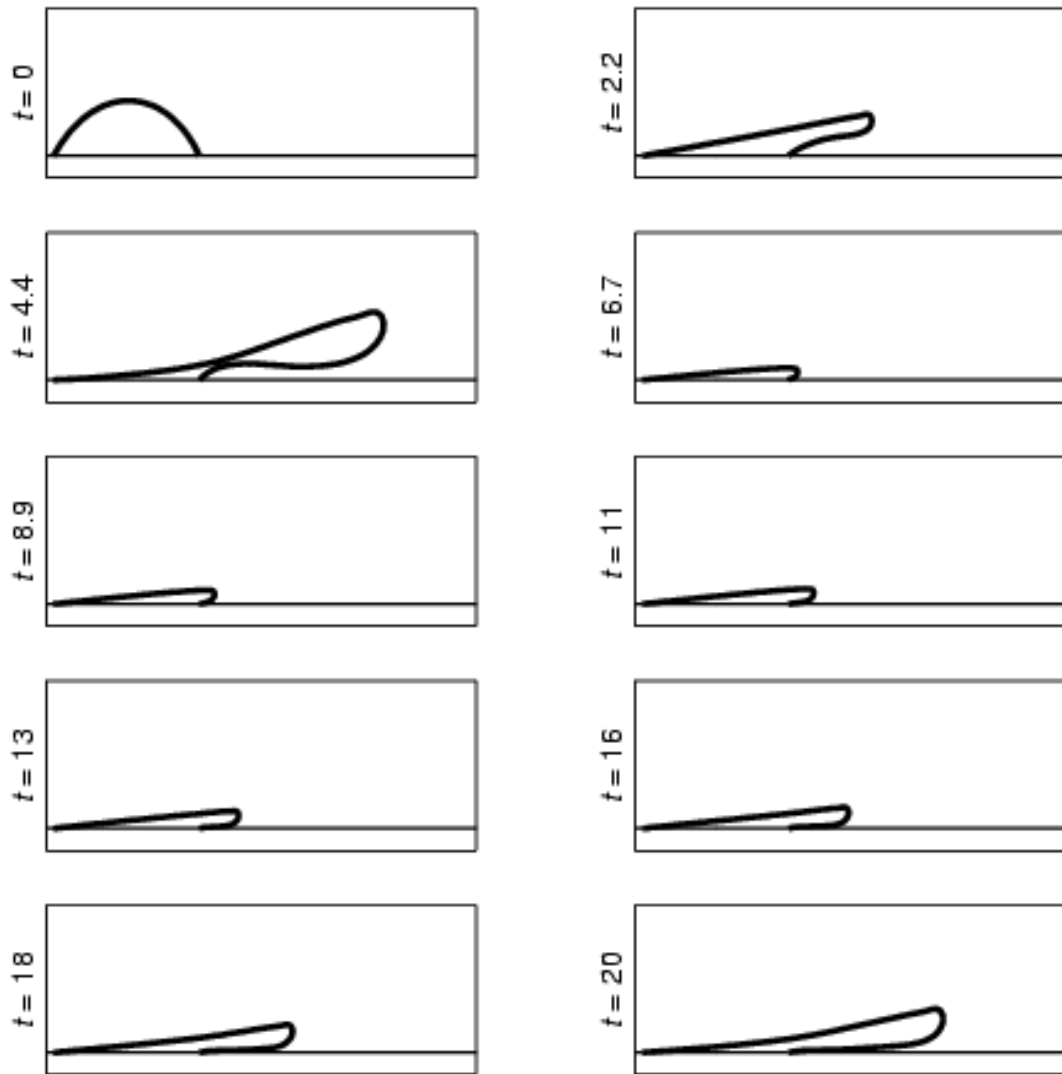
Figure 18. Interface positions at successive times _t_ for the case depicted in Figure 17, demonstrating how a nucleation site could shed multiple bubbles when the liquid is gas supersaturated.

3.3.b Effects of varying parameters on inception

Figure 19 shows the variation of the bubble pressure with time for the baseline case to study inception ($Ci = 1$, $W = 0.1$, $A_C = 0$, impermeable liquid model, and pinned contact lines) for several cases with the same initial shape, $\kappa_o = 10$, but different capillary numbers $Ca_L = 40$, 45, 47.5, 50, and 55. InFigure 19 these correspond to values of Ca_Lh = 0.54, 0.6, 0.64, 0.67, and 0.74, where h is the distance from the plane in which the crevice mouth liesto the furthest point on the bubble. The behavior depicted in Figure 16 is not universal for all cases; pinch-off does not always occur. For the simulations used to produce Figure 19, pinch-off occurred only in the two cases of highest capillary number. A steady state shape was quickly reached for the lowest capillary number case. For the two other cases, the bubble growth continues to slow; although a steady shape was not reached for the time span simulated, the growth is not vigorous enough to be considered cavitation inception. The transition between the quick achievement of steady state to low growth occurs with increasing Ca when the steady state contact angle at the leading edge goes to zero, as can be seen in the insert in Figure 19. For an impermeable liquid, whether a nucleation site bubble will deform to the point that it will pinch-off depends upon crevice cross sectional area A_C, as well as Ci, Ca_L and h, and also upon the advancing and receding contact angles, crevice shape, and the relative nearness of the far wall W. For the baseline case, pinch-off will occur when Ca_Lh exceeds 0.64. In this section the trends of how variation from the baseline conditions affects the critical Ca_Lh above which pinch-off occurs are reported. Results are primarily presented as plots of p_B–Ci versus t. For the impermeable liquid model this plot is closely related to a plot of bubble area vs. t, so rapid expansion is easily recognized as a quick reduction in $p_B - Ci$.
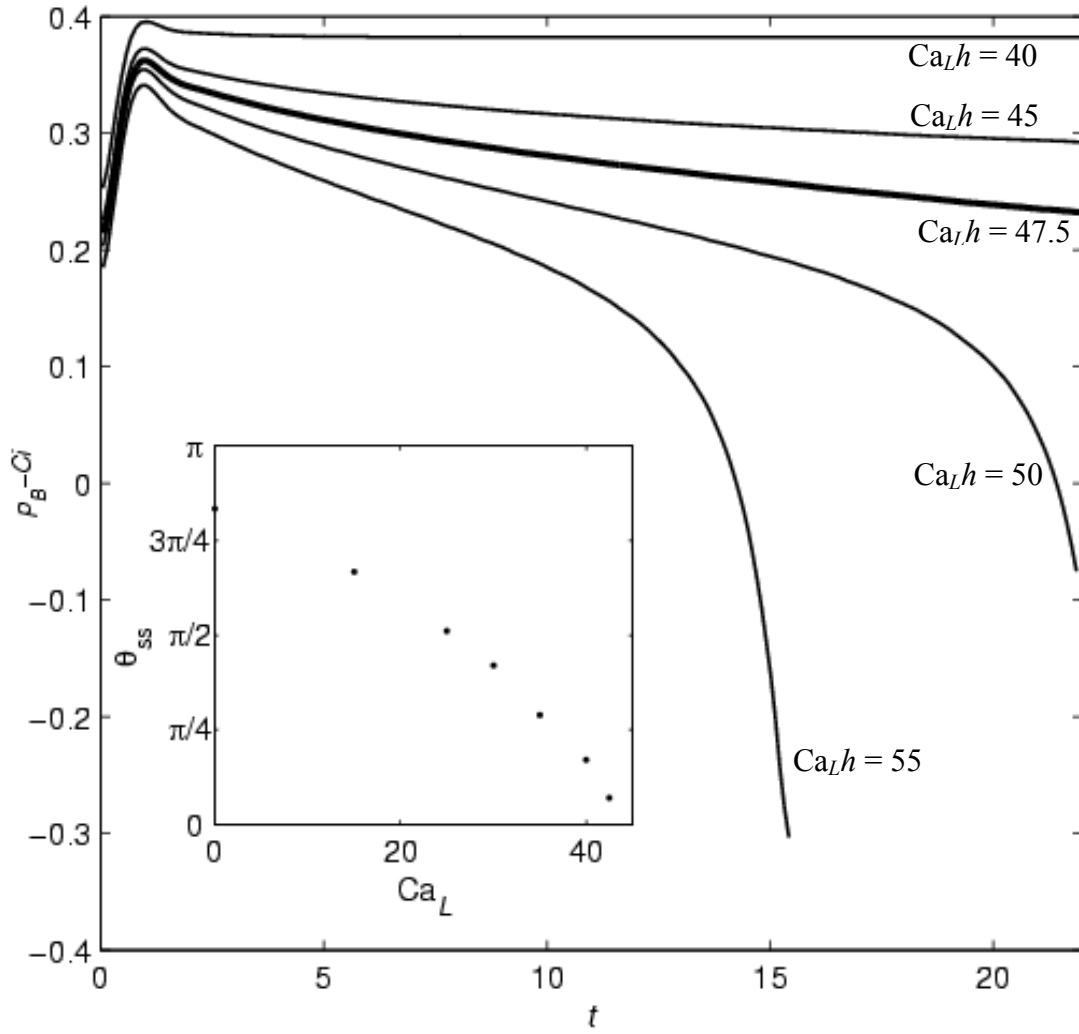
Figure 19. Variation of excess pressure in the bubble vs. time for five cases of different capillary number. For all cases, the baseline conditions are used, and κ_o=10 (giving $h = 0.0134$). Results are plotted for Ca_L of 40 and 45 (top two thin lines), 47.5 (thick line) and 50 and 55 (bottom two thin lines). For $Ca_L > 47.5$ ($Ca_L h > 0.64$) pinch-off occurs. The insert shows the variation of final (steady state) contact angle θ_{ss} at the leading contact line as a function of Ca_L. θ_{ss}=0 for $Ca_L = 42$. For $Ca_L > 42$ steady conditions were not achieved, although the growth rate decreased monotonically with t following the pressure maximum for $Ca_L <$ 47.5.

Further, this method of presentation has the advantage of providing a quick method of assessing, for a given level of gas saturation, the direction (in or out of the void) of mass transport if it were incorporated into the model.

All of the simulations in Figure 19 are for bubbles with the same initial shape. Although it is clear that for a given set of condition there will be a critical capillary number

$$\mathrm{Ca} = \frac{\mu}{\gamma}\left(\frac{U}{L}\right)L_s \tag{3.79}$$

above which pinch-off occurs, it is not immediately obvious that the best choice for L_s is the distance that the bubble extends above boundary wall. The first hint that this is the case is the previously reported observation that interfaces with negative curvature and their endpoints at the crevice corners are stable to all shear. These are interfaces with $\mathrm{Ca}_L h$ less than or equal to zero; however, this observation does not rule out the use of $\mathrm{Ca}_L \kappa_o$ or perhaps $\mathrm{Ca}_L \kappa_z W$ for predicting pinch-off. Neither do physical considerations reveal clearly which of these is the more appropriate choice. By comparing the results of two simulations, the superiority of the grouping $\mathrm{Ca}_L h$ becomes evident. Both simulations are for $Ci = 1$, $\mathrm{Ca}_L = 50$, $A_C = 0$ and pinned contact lines. In one simulation (a) $W = 0.1$ and $\kappa_o = 10$, and for the other (b) $W = 0.2$ and $\kappa_o = 2.63$:

(a) $\mathrm{Ca}_L h = 0.64$; $\mathrm{Ca}_L \kappa_o = 500$; and, $\mathrm{Ca}_L \kappa_z W = 50$

(b) $\mathrm{Ca}_L h = 0.64$; $\mathrm{Ca}_L \kappa_o = 131.5$; and, $\mathrm{Ca}_L \kappa_z W = 26.3$.

Note that (a) is the same as the lower Ca curve in Figure 19 for which pinch-off occurs. The results are displayed in Figure 20 and it is clear that the two are similar. For either $\mathrm{Ca}_L \kappa_o$ or $\mathrm{Ca}_L \kappa_z W$ to be a good choice for correlating pinch-off data, then it would be
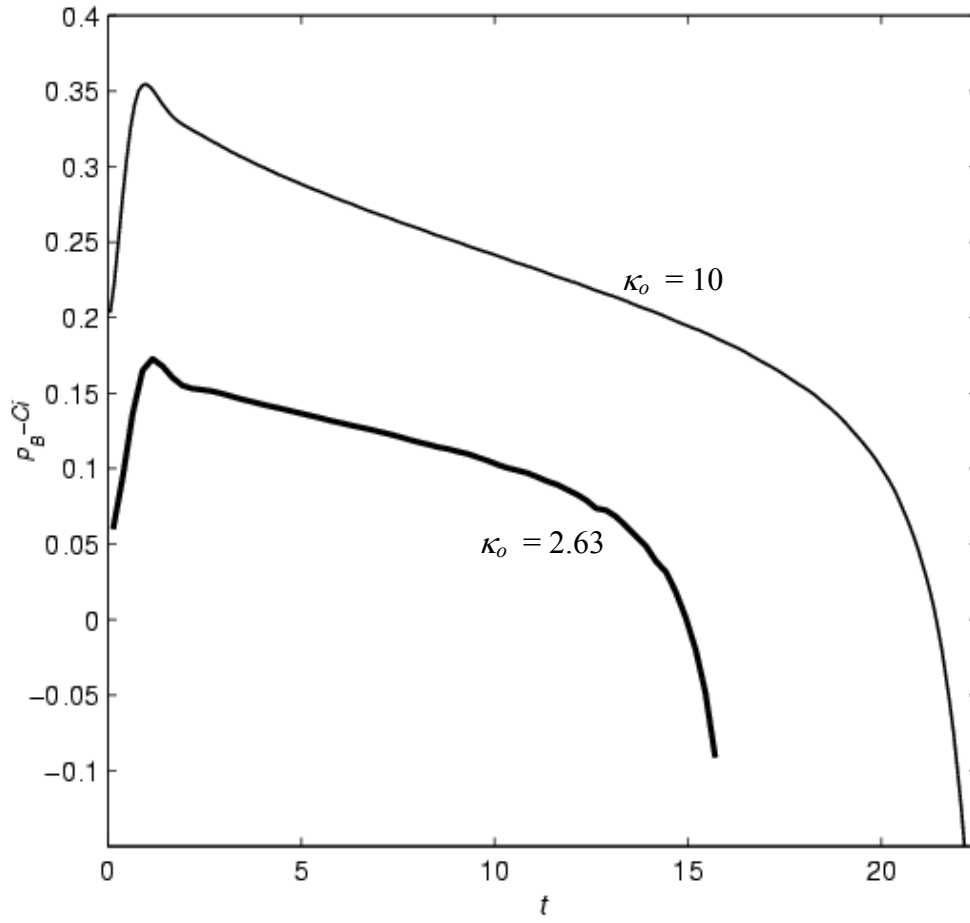
Figure 20. Plot used to demonstrate that the grouping Ca$_L$h is indeed useful for correlating pinch-off data. Both curves were generated in simulations using the baseline conditions except the thick line data used $W = 0.2$. For both simulations Ca$_L$h = 0.67: Ca$_L$ = 50 for both, but for the (top) thin line data $\kappa_o = 10$ and for the (bottom) thick line data $\kappa_o = 2.63$ (b).

necessary for pinch-off to be inhibited in (b) as compared to (a), which is clearly not the case.

Based on the PNSCC it might be expected that Ci should have a large effect on the critical $Ca_L h$ above which pinch-off occurs. This is not the case, and, in fact, the effect of Ci on critical $Ca_L h$ is opposite what the PNSCC would apparently suggest. Recall that the PNSCC with $\sigma_c = 0$ predicts cavitation when Ci is reduced to unity or below. This might suggest that the critical $Ca_L h$ increases with increasing Ci, while, actually, for Ci from 0.1 to 10 the critical $Ca_L h$ decreases with increasing Ci, as can be seen in Figure 21. The effect is more dramatic for $Ci < 1$. For Ci of 0.1 pinch-off does not occur for $Ca_L h$ less than 0.8, while for Ci of 10 the critical value of $Ca_L h$ has not changed to two significant figures. That the trend of decreasing critical $Ca_L h$ with increasing Ci does not irrevocably bring the inception model and the PNSCC into complete contradiction is due to the fact that for a given nucleation site, if Ci varies but Ca_L is kept constant, then h must change. The importance of this effect is expanded upon in section 3.6.

In general increasing crevice cross sectional area, A_C, should have an effect somewhat similar to that of increasing mass transfer, as a large volume below the bubble will weaken the effect of interface deformation on bubble pressure. This conjecture is borne out by simulations, which indicate that a lower crevice volume promotes pinch-off (Figure 22).

The presence of an opposing wall has a confining effect on the flow that will alter the deformation of the bubble. It is not obvious whether this effect will be to promote or hinder bubble pinch off. Either argument could be made: the confined flow will resist

71
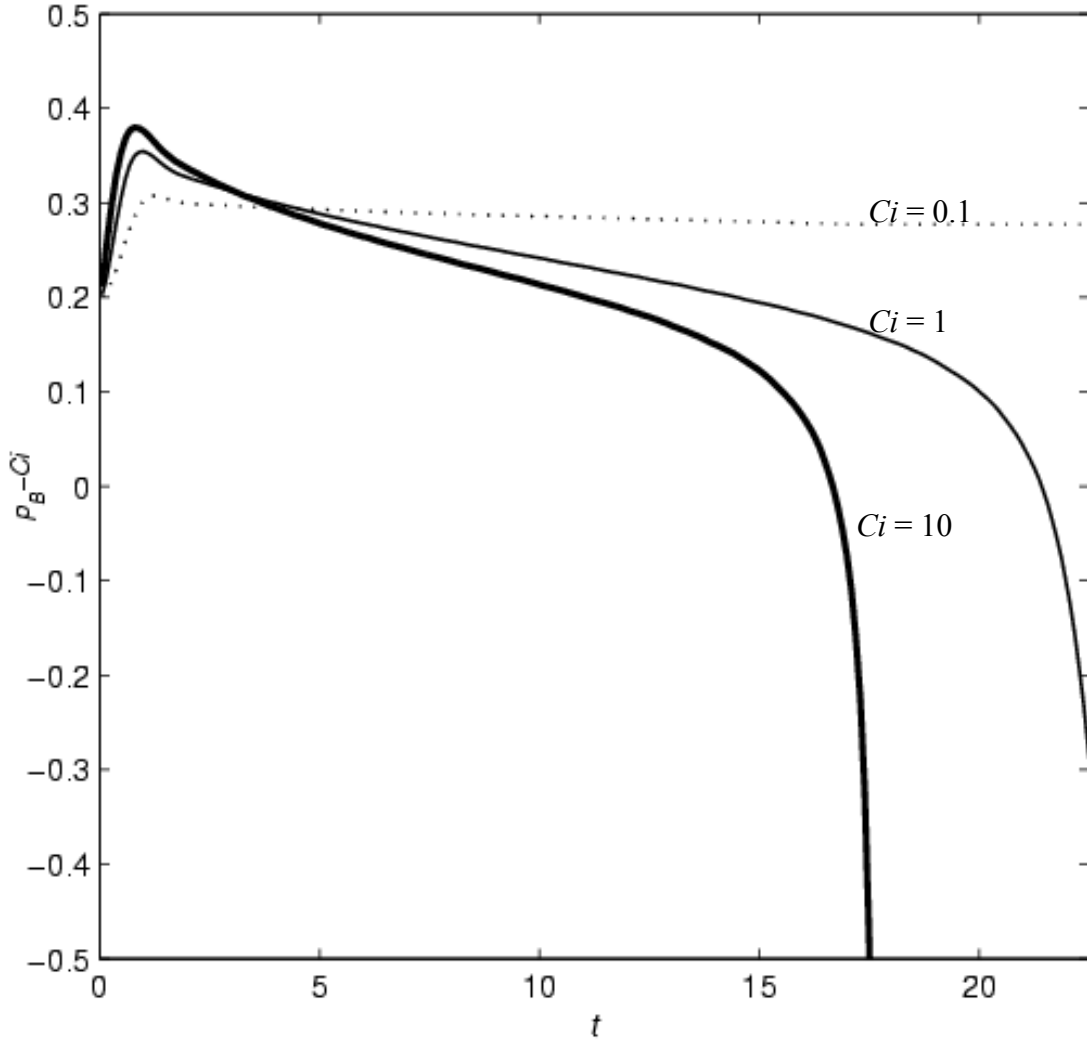
Figure 21. Variation of bubble pressure above *Ci* showing effect of *Ci* on pinch-off for baseline conditions (except for *Ci*) and Ca$_L$ = 50, κ_o = 10 (Ca$_L$h = 0.67). The thick line is the result of a simulation with *Ci* = 10, the thin line for *Ci* = 1, and the dotted line for *Ci* = 0.1. As *Ci* decreases, pinch-off is inhibited.
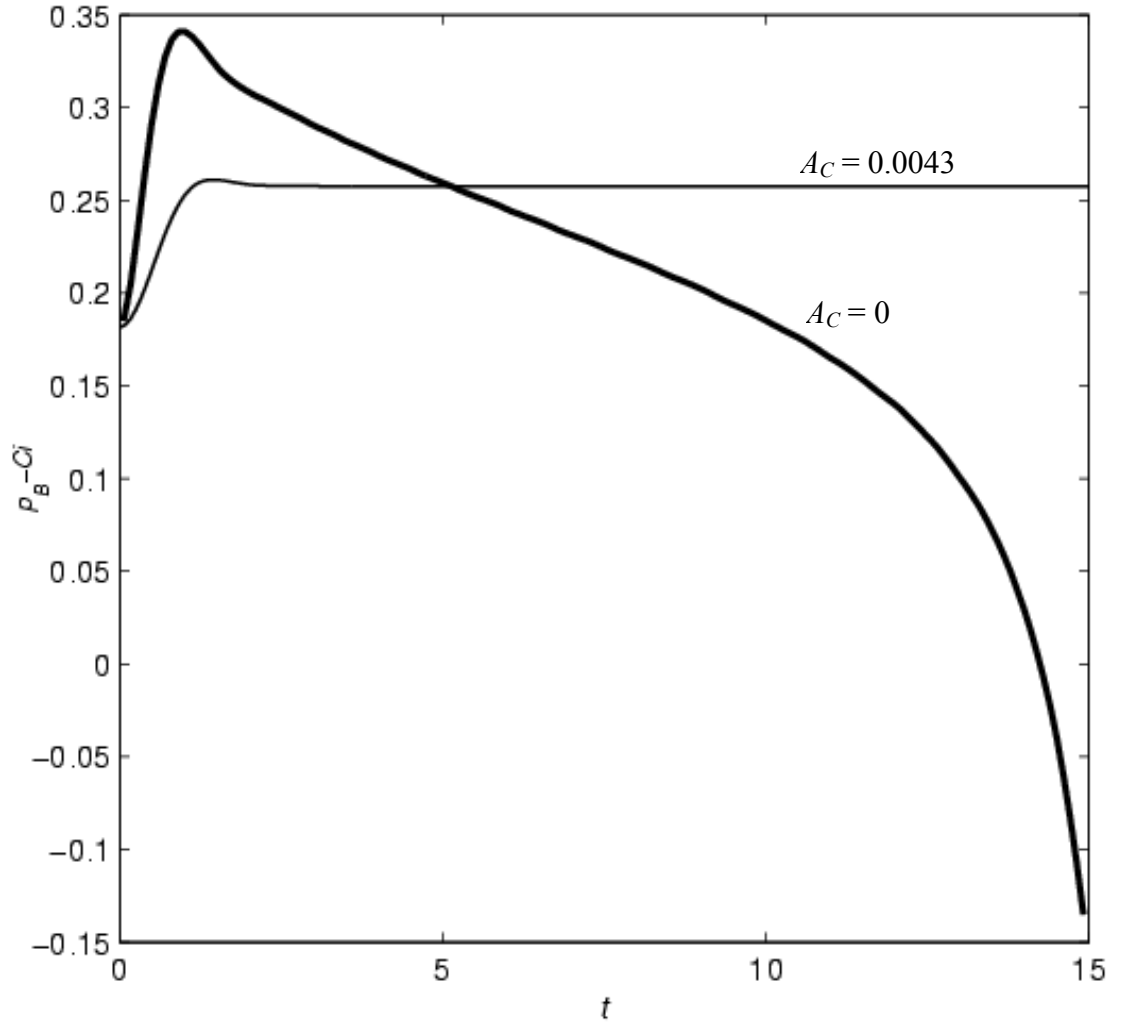
Figure 22. Effect of crevice cross sectional area on response of identically shaped preexisting nuclei to the same shearing simulation conditions. For both cases, $Ci =$ 1, $Ca_L = 55$, $\kappa_o = 10$, $W = 0.1$ ($Ca_L h = 0.74$), the liquid is impermeable to gas and the contact lines are pinned. For the case for which pinch-off occurs, $A_C = 0$, while for the case in which a steady pressure is achieved, $A_C = 0.0043$.

bubble growth or it will increase the early compression and drive the bubble deformation to a higher curvature, therefore allowing the conditions for bubble pinch-off to occur at a lower capillary number.   The effect of the relative nearness can be investigated by reducing or increasing W while doing the opposite to Ca_L so that Ca_Lh does not change. Simulations were performed for W above and below the baseline value of 0.1, with all other conditions at baseline, and $Ca_Lh = 0.67$.   The results are shown in Figure 23.   For $W=0.05$ and $W = 0.1$, ($Ca_L = 100$ and 50 respectively) the behavior was nearly identical, except that after the initial compression, the timescale for the expansion seems to vary inversely with W. This role of W in the expansion time scale also is evident in Figure 20. The results for $W = 0.2$ ($Ca_L = 25$) indicate that as the opposing wall is brought closer, pinch-off is made less likely.   Note that for $W = 0.2$ and the initial curvature that was used, $\kappa_o = 1/W$, $h = 0.027$.   The distance to the opposing wall is nearly forty times the distance the bubble extends out of the crevice, and yet the far wall has a dramatic effect. This is typical in two-dimensional Stokes flows, where disturbances extend distances usually two orders of magnitude greater than the disturbance size.

To this point, little has been said about the role of contact line dynamics in inception. For examining the effects of other parameters on pinch-off, the contact lines have been kept pinned. Contact line motion was needed to successfully simulate voids with initially negative curvature such as those in Figure 14, but recall that these never lead to pinch-off. Based on an examination of the baseline case, for which contact lines are pinned, it seems that a wetting liquid will be more likely to pinch-off, as the rear contact line will move into the crevice, making it more likely that the interface will close off.   This conjecture is tested, and the role of contact line dynamics investigated by

74
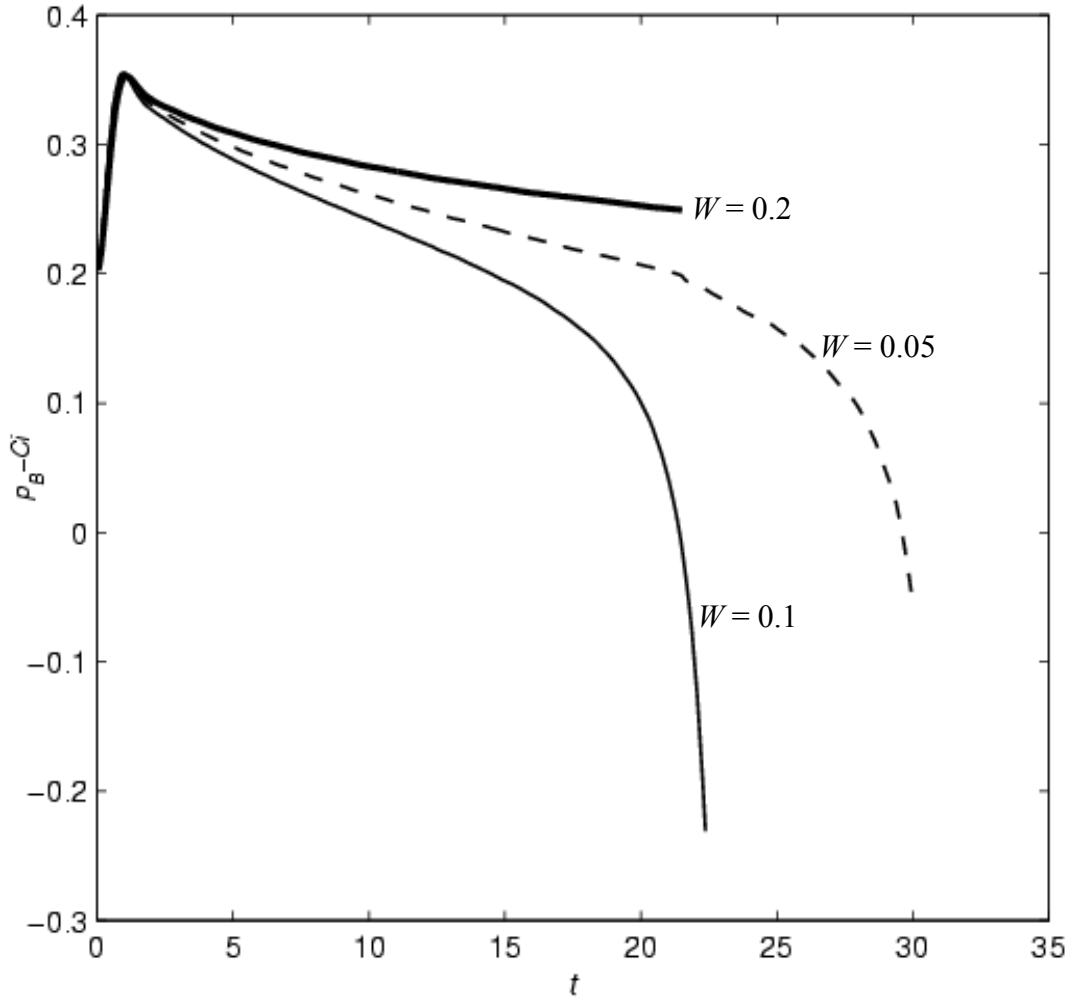
Figure 23. Plots of p_B - Ci vs. t to demonstrate the effect of the relative distance to the far wall. The simulations used the impermeable liquid model with pinned contact lines. Three simulations were run, with W of 0.1 (thin line), 0.05 (dashed line) and 0.2 (thick line). The initial curvatures κ_o and the capillary numbers Ca_L were specified so that the simulations would be for identical conditions with the exception of the distance to the far wall: $\kappa_o = 1/W$, and $Ca_L = 5/W$; therefore, for all simulations $Ca_L h = 0.67$. For $W \leq 0.1$ the only effect of distance to the far wall is to change the time scale of the expansion, while for $W > 0.1$, bringing the far wall closer inhibits expansion and subsequent pinch-off.

75

considering a series of four simulations that differ only in their contact line behavior. For all four simulations, the baseline conditions of $W = 0.1$ and the impermeable liquid model are used. The crevice is a trapezoid with $\theta_{CL} = \theta_{CR} = \pi/6$ and $A_C = 4.33\text{x}10^{-4}$. The initial curvature is $\kappa_o = 10$, and the capillary number is $\text{Ca}_L = 80$, giving $\text{Ca}_L h = 1.07$. This choice of capillary number is sufficiently high to result in pinch-off for the pinned contact line case despite the nonzero crevice area. One simulation has pinned contact lines (a), one has no hysteresis, $\theta_A = \theta_R = \pi/3$ (b), one will have leading contact line motion, $\theta_A = \pi$, $\theta_R = \pi/3$ (c), and the last will have the rear contact line move into the crevice, $\theta_A = \pi/3$, $\theta_R = 0$ (d). Based on the conjecture about the effect of contact line dynamics, it is expected that in the wetting case (d) pinch-off will occur earlier than for the pinned case (a), while in the more hydrophobic case (c), pinch-off should be inhibited. The result in the no-hysteresis case (b) cannot be readily predicted. The simulation results are presented, again as $p_B - Ci$ vs. t, in Figure 24. Based on the choice of advancing/ receding contact angles of $\pi/3$ and the initial curvature, the rear contact line begins moving almost immediately in cases (b) and (d), while, in (b) and (c) the leading contact line does not start moving until $t = 0.5$. The increase in the compression due to rear contact line motion is greater than might have been supposed, and the subsequent expansion prior to pinch-off is more rapid. Alone, rear contact line motion into the crevice promotes pinch-off. Similarly, leading contact line motion away from the crevice, with no rear contact line motion, inhibits pinch-off. The surprising result is that combined motion of both (which can be viewed as translation of the bubble in the flow direction) has a greater effect on reducing the stress needed for pinch-off than rear contact line motion alone.
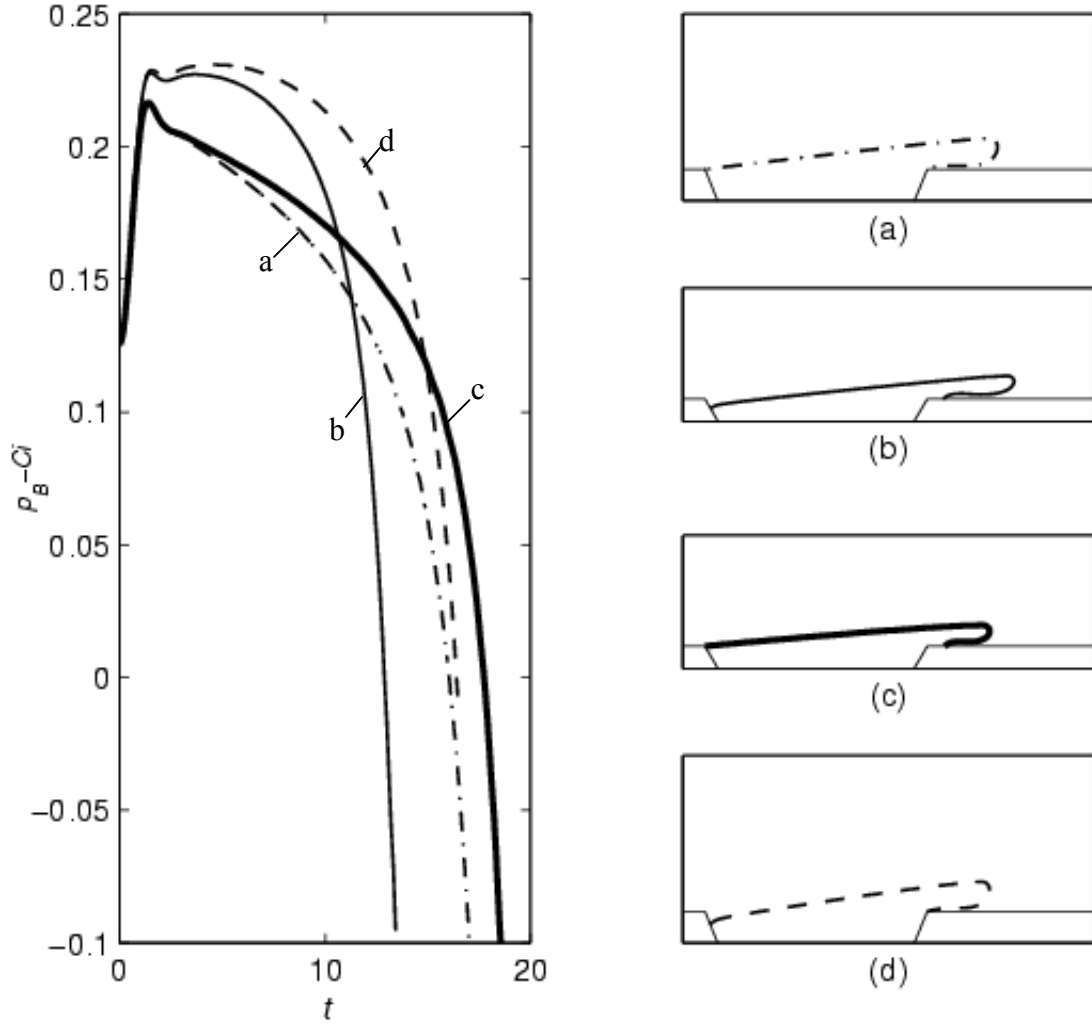
Figure 24. Plots demonstrating the effect of contact line motion on pinch-off. For all four simulations $Ci = 1$, $Ca_L = 80$, $\kappa_o = 10$, $W = 0.1$, $\theta_{CL} = \theta_{CR} = \pi/6$ and $A_C = 4.33 \times 10^{-4}$. The differences are in selection of advancing and receding contact angles: (a) dot-dash lines, pinned contact lines, $\theta_A = \pi$, $\theta_R = 0$; (b) thin lines, no hysteresis, $\theta_A = \pi/3$, $\theta_R = \pi/3$; (c) thick lines, non-wetting, $\theta_A = \pi$, $\theta_R = \pi/3$; (d) dashed lines, wetting, $\theta_A = \pi/3$, $\theta_R = 0$. The plots of interface position are for each case at $t = 7.5$.

Changing the applied pressure, as was done in the experiments, has several possible effects. If the pressure change is extreme then the properties of the liquid can change. If the pressurization is done with gas, then the concentration of dissolved gas in the liquid changes. The cavitation index, Ci, changes with the pressure for the same applied shear stress; this has effects already discussed. Finally, nuclei will respond mechanically to pressure changes; this mechanical response can include motion of the contact line into or out of the crevice (Atchley and Prosperetti 1989), and is the subject of section 3.6.

3.4   THEORY AND SIMULATION – PERSISTENCE OF NUCLEI

One of the more important conclusions drawn from the simulations of cavitation inception from wall-attached gas nuclei is that the cavitation nuclei have positive curvature (are convex toward the liquid). This is counter to the typically held view of such nuclei, which would permit a positive curvature only if the liquid were supersaturated with dissolved gas. Otherwise, the reasoning goes, the positive curvature would result in a Laplace pressure that would keep the bubble pressure above the liquid pressure. Thus diffusion would drive gas from the bubble until it had zero curvature, if the bulk liquid were saturated, or negative curvature if the bulk liquid were undersaturated. There are other theories that predict persistent nuclei with positive curvature. Mørch proposed that ambient vibrations lead to resonance in voids in local wall concavities, resulting in rectified diffusion and stable nuclei with positive curvature (Mørch 2000). Crum presented hypotheses of stabilization due to an ionic or surface-active skin on bubbles in water (Crum 1982). This section presents an analysis that relaxes the need for such explanations by greatly extending the time a nucleus would be

expected to persist with positive curvature. The analyses starts with a model for dissolution of a spherical bubble of initial radius $R^* = R_o$ in a viscous liquid.

3.4.a Dissolution of a spherical bubble in a viscous infinite medium

The problem of an expanding or contracting spherical gas bubble in a liquid has been addressed numerous times, starting apparently with Lord Rayleigh, and a thorough review of the literature was performed by Plesset and Prosperetti (Plesset and Prosperetti 1977). Assuming that the bubble is not translating, the resulting flow is irrotational and can be described in a spherical coordinate system with the origin at the bubble center, using a potential function ϕ such that the radial component of the velocity is $u_r^* = \dfrac{\partial \phi^*}{\partial r^*}$.

The solution corresponds to that for a point source or sink with time varying strength $m(t^*)$, and is one dimensional, $\mathbf{u}^* = \left(u_r^*, 0, 0\right)$. For unsteady irrotational flow, Bernoulli's equation is

$$\frac{\partial \phi^*}{\partial t^*} + \frac{1}{2}\left|\mathbf{u}^*\right|^2 + \frac{p^*}{\rho} - \mathbf{g} \cdot \mathbf{x}^* = c\left(t^*\right) \tag{3.80}$$

Substituting the velocity and corresponding potential for a point source into Eq. (3.80) on the bubble surface ($\mathbf{x}^* = R^*$) and as $\mathbf{x}^* \to \infty$, and neglecting body forces, yields

$$\frac{p^*\left(R^*\right) - p_\infty^*}{\rho} = \frac{3}{2}\dot{R}^{*2} + R^*\ddot{R}^* \tag{3.81}$$

The dynamic boundary condition on the bubble surface relates the pressure in the liquid to the pressure of the gas in the bubble

$$p_B^* = p^*\left(R^*\right) - 4\mu\frac{\dot{R}^*}{R^*} + 2\frac{\gamma}{R^*} \tag{3.82}$$

Combining Eqs . (3.81) and (3.82) produces a form of the Rayleigh equation

$$\frac{3}{2}\dot{R}^{*2} + R^*\ddot{R}^* + 4\nu\frac{\dot{R}^*}{R^*} = \frac{p_B^* - p_\infty^* - 2\frac{\gamma}{R^*}}{\rho} \tag{3.83}$$

The bubble pressure varies due to an equation of state, which we take to be the ideal gas equation of state

$$p_B^* = c_B^* R_u T \tag{3.84}$$

where generally the molar gas concentration in the bubble, c_B^*, and temperature, T, are found by solving species and energy conservation equations. It is assumed that the system will remain isothermal due to the slow rates of dissolution seen for bubbles in our experimental systems. Binary Fickian diffusion of a single dissolved gas species in the liquid is assumed, and, because velocities are expected to be small, advection is neglected:

$$\frac{\partial c^*}{\partial t^*} = \frac{D}{r^{*2}}\frac{\partial}{\partial r^*}\left(r^{*2}\frac{\partial c^*}{\partial r^*}\right) \tag{3.85}$$

The boundary conditions, assuming that far from the bubble the liquid is saturated with gas, are, from Henry's law,

$$c^*\left(R^*\right) = Hp_B^*$$
$$c^*\left(r^* \to \infty\right) = Hp_\infty^* \tag{3.86}$$

The solution to the mass conservation problem, Eqs. (3.85) and (3.86), is used to find the concentration gradient at the bubble surface, which is incorporated into a statement of species conservation for the bubble

$$\frac{4}{3}\pi\frac{d}{dt^*}\left(R^{*3}c_B^*\right) = 4\pi DR^{*2}\left.\frac{\partial c^*}{\partial r^*}\right|_{r^*=R^*} \tag{3.87}$$

The system requires initial conditions for completeness. The initial species concentration is taken to be everywhere saturated

$$c^*\left(t^* = 0\right) = Hp_\infty^* \tag{3.88}$$

The initial bubble size depends upon the situation of interest. The resulting system can be solved numerically, using, for instance, a finite difference method (Duda and Vrentas, 1969, and Kontopoulou and Vlachopoulos, 1999). Instead, a simplification is used that was first reported by Epstein and Plesset (Epstein and Plesset 1950). The simplification concerns the gas diffusion problem. By neglecting the motion of the bubble surface, the concentration gradient at the surface is found to be approximately

$$\left.\frac{\partial c^*}{\partial r^*}\right|_{R^*} \approx -H(p_B^* - p_\infty^*)\left(\frac{1}{R^*} + \frac{1}{\sqrt{\pi Dt^*}}\right) \tag{3.89}$$

so that Eq (3.87) becomes

$$3\dot{R}^* c_B^* + R^* \dot{c}_B^* \approx -3DH(p_B^* - p_\infty^*)\left(\frac{1}{R^*} + \frac{1}{\sqrt{\pi Dt^*}}\right) \tag{3.90}$$

The equation of state, Eq. (3.84), and its derivative with respect to time are used to replace c_B and its time derivative in Eq. (3.90)

$$\dot{p}_B^* \approx -3R_u THD\frac{(p_B^* - p_\infty^*)}{R^*}\left(\frac{1}{R^*} + \frac{1}{\sqrt{\pi Dt^*}}\right) - 3p_B^* \frac{\dot{R}^*}{R^*} \tag{3.91}$$

The model is made nondimensional with the following scales:

$$L_s = R_o,\ p_s = \frac{\gamma}{R_o},\ t_s = \frac{\mu R_o}{\gamma} \tag{3.92}$$

so that Eq. (3.83) becomes

$$\frac{3}{2}\dot{R}^2 + R\ddot{R} + \frac{\mu^2}{\rho\gamma R_o}\left(\frac{4\dot{R}}{R} - p_B + p_\infty + \frac{2}{R}\right) = 0 \tag{3.93}$$

where the nondimensional group in front of the parenthesis is the ratio of the capillary number to the Reynolds number and is much larger than one for bubble dissolution in a highly viscous liquid. Neglecting therefore the first two (inertial) terms in Eq. (3.93) and scaling also Eq. (3.91) one obtains the simplified dimensionless model of Eq. (3.94). It is

a dimensionless model for dissolution of a spherical bubble in a viscous liquid, neglecting

inertial effects, and approximating the concentration gradient at the bubble surface:

$$\dot{R} \approx \frac{p_B - p_\infty}{4} R - \frac{1}{2}$$

$$\dot{p}_B \approx -3\Pi_1 \frac{(p_B - p_\infty)}{R}\left(\frac{1}{R} + \frac{\Pi_2 t^{-\frac{1}{2}}}{\sqrt{\pi}}\right) - 3p_B \frac{\dot{R}}{R} \tag{3.94}$$

$$\Pi_1 = \frac{R_u THD\mu}{\gamma R_o}, \ \Pi_2 = \sqrt{\frac{R_o\gamma}{D\mu}}$$

The initial conditions

$$R(0) = 1$$
$$p_B(0) = p_\infty + 2 \tag{3.95}$$

are chosen so that the bubble is initially in mechanical equilibrium. The model depends

upon three parameters: p_∞, Π_1 and Π_2.

The system consists of a pair of coupled nonlinear ODEs that can easily be

numerically integrated provided that the singularity at $t = 0$ is avoided by starting at some

slightly positive time. In essence, this is assigning some large but finite concentration

gradient initially, instead of the artificial infinite gradient required by the initial

conditions of the model. The model is verified by plotting its results against the results of

a simple experiment in which bubble dissolution in PDMS was videotaped. The images

were used to obtain a plot of bubble radius versus time, shown in Figure 25 (a). After an

initial period in which the variation of bubble radius is affected by concentration

gradients resulting from the diffusion from surrounding bubbles, the model and data

show very good agreement. Data on diffusivity and solubility of air in polybutene could

not be found. To obtain estimates of these properties, the same bubble radius experiment

was performed on PB and then an optimization routine was used to find the values of H

and D that give the best fit to the data. These are the property values given in Table I for

PB. The surface tension and dynamic viscosities were provided by the manufacturer,

with viscosities verified in this lab. The diffusivity and Henry's constant for PDMS were

found using published data and an Arhenius type correlation for temperature correction

(Hirose *et al*. 1989). Figure 25 shows plots of the data against the model for PDMS (a)

and PB (b). The model can also be used to determine whether viscous effects are

important for a given bubble size. For PDMS, viscous effects are important, though not

dominant, for bubbles where $R_o < 10$ μm, while for PB viscous effects are not noticeable

unless $R_o < 1$ μm. When viscous effects are important, they always extend the bubble

dissolution time.

3.4.b Dissolution of crevice stabilized sphere-cap bubbles

The effect of locating the bubble on a solid wall on the rate of dissolution is

considered next. First it is noted that if the bubble were a hemisphere on a flat wall with

fixed contact angles of $\pi/2$ then the solution to the species conservation problem would

be the same as above due to symmetry. The flow would no longer be spherically

symmetric due to the no slip boundary condition at the wall. If instead the contact line is

pinned on a crevice then the problem loses its spherical symmetry completely, even if the

Table I. PB and PDMS Transport Properties				
	γ [N m^{-1}]	μ [Pa s]	D [m^{2}s^{-1}]	H [mol m^{-3} Pa^{-1}]
PDMS	0.020	1000	1.57 x 10^{-9}	7.34 x 10^{-5}
PB	0.034	1000	0.48 x 10^{-9}	0.55 x 10^{-5}
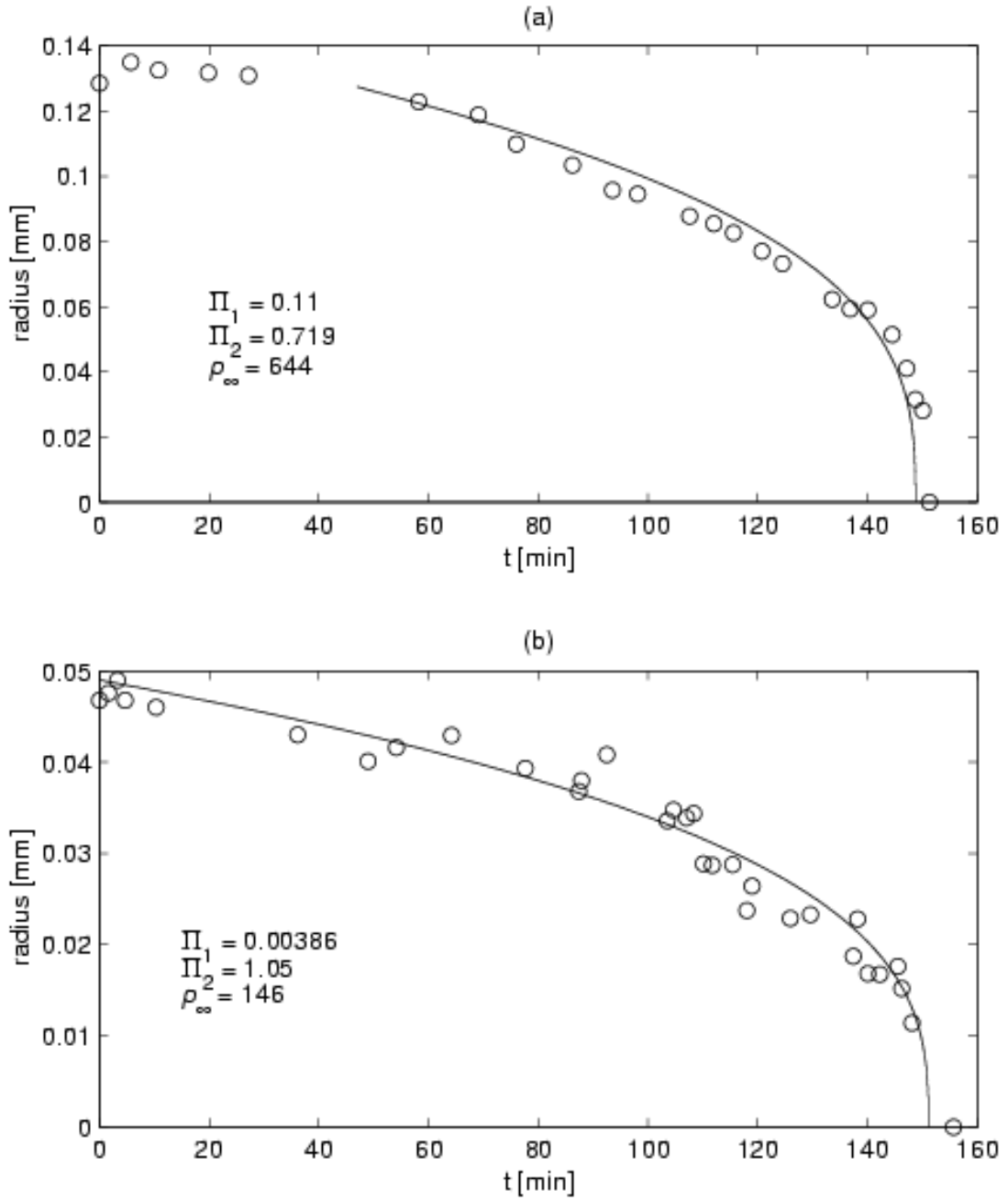
Figure 25. Bubbles in PDMS (a) and PB (b) were videotaped during dissolution. Plots of bubble radii vs. time for PDMS are plotted to validate the model of bubble dissolution, Eq. (3.94), while for PB the data are used to obtain estimates of the transport properties H and D.

crevice mouth is circular and the bubble surface is assumed to maintain the shape of a spherical cap. Such a case of a crevice with a circular mouth whose radius is equal to the initial bubble radius will be considered. The crevice is defined by its volume, V_C^*, and the initial bubble radius, R_0. The dissolution problem here is clearly quite different than in the case of a free bubble. The main difference is due to the fact that, as gas leaves the bubble and the bubble volume decreases, the curvature of the bubble surface decreases instead of increasing. Thus the pressure in the bubble decreases with time, reducing the driving force for diffusion. The bubble will asymptotically approach a steady solution of zero curvature. Note that this assumes the contact line does not move into the crevice as the contact angle increases.

In order to retain the simplicity of the solution developed for a free bubble, that problem is revisited with terms in that solution replaced with terms from the crevice stabilized problem. The resulting solution will provide order of magnitude estimates. First consider Eq. (3.89). The second term in parenthesis is essentially the inverse of the penetration depth for one-dimensional diffusion into an infinite medium, and is retained unaltered for the crevice stabilized bubble solution. The first term in parenthesis therefore accounts for the multidimensionality of the diffusion. In the case of spherical spreading this term becomes $1/R^*$. This effect is included in the non-spherically symmetric problem by approximating the bubble as a shrinking hemisphere. R^* is replaced with an equivalent radius

$$R_{eq}^* = \frac{A_B^*}{C_B^*}$$

(3.96)

85

where A_B^* is the area of the bubble surface and C_B^* is the arclength of the contact line. Note that for a hemisphere $R_{eq}^* = R^*$. A generalized version of Eq. (3.89) is used to calculate an average molar flux from the bubble

$$\overline{n}''^* \approx HD(p_B^* - p_\infty^*)\left(\frac{1}{R_{eq}^*} + \frac{1}{\sqrt{\pi Dt^*}}\right) \tag{3.97}$$

Species conservation for the bubble is

$$\frac{d}{dt^*}\left[(V_B^* + V_C^*)\frac{p_B^*}{R_u T}\right] = -HD(p_B^* - p_\infty^*)\left(\frac{1}{R_{eq}^*} + \frac{1}{\sqrt{\pi Dt^*}}\right)A_B^* \tag{3.98}$$

where V_B^* is the volume of the bubble outside of the crevice and V_C^* is the volume of the crevice. Upon rearrangement and nondimensionaliztion,

$$\frac{dp_B}{dt} = -\Pi_1\frac{(p_B - p_\infty)A_B}{(V_B + V_C)}\left(\frac{C_B}{A_B} + \Pi_2\frac{t^{-\frac{1}{2}}}{\sqrt{\pi}}\right) - \frac{dV_B}{dt}\frac{p_B}{(V_B + V_C)} \tag{3.99}$$

For a spherical cap the following formulae are from geometry (made dimensionless)

$$V_B = \frac{\pi h^2}{3}\left(\frac{3}{\kappa_m} - h\right)$$

$$A_B = 2\pi\frac{h}{\kappa_m}$$

$$C_B = 2\pi \tag{3.100}$$

$$h = \frac{1}{\kappa_m}\left(1 - \sqrt{1 - \kappa_m^2}\right)$$

which makes

$$\frac{dV_B}{dt} = -\pi\frac{\kappa_m^2 + 2\sqrt{1 - \kappa_m^2} - 2}{\kappa_m^4\sqrt{1 - \kappa_m^2}}\dot{\kappa}_m \tag{3.101}$$

Substituting into Eq. (3.99), yields, for the case of a pinned contact line, a circular crevice mouth, and a spherical cap bubble, a first order differential equation in time with dependent variables p_B and κ_m that one can write in the form

86

$$\dot{p}_B = f_1\left(p_B, \kappa_m, \dot{\kappa}_m, t; \Pi_1, \Pi_2, p_\infty\right) \tag{3.102}$$

For the fluid mechanics portion of the model one starts with Eq. (3.93) and again neglects the inertial terms. Twice the mean curvature, $2\kappa_m$, replaces $2/R$ in the last term in parenthesis, and the normal viscous stress term is treated in the same manner in which we the diffusion problem was manipulated, using the equivalent radius to capture effects due to changing geometry. This introduces the largest error of all of the approximations, as even in the case of a shrinking hemisphere this will not correctly model the effects of the wall. Nevertheless, it will provide a reasonable approximation of the contribution of normal viscous stresses. For the case of a pinned contact line, a circular crevice mouth, and spherical cap bubble the resulting equation is

$$\frac{d}{dt}\left(\frac{h}{\kappa_m}\right) = \left(\frac{p_B - p_\infty}{4\kappa_m} - \frac{1}{2}\right)h \tag{3.103}$$

Upon substitution of the definition of h from Eq. (3.100), Eq. (3.103) can be rearranged

$$\dot{\kappa}_m = f_2\left(\kappa_m, p_B; p_\infty\right) \tag{3.104}$$

Therefore the problem requires the solution of two, coupled, nonlinear first order ordinary differential equations. Once again, consideration is limited to initial conditions of a hemispherical bubble in mechanical equilibrium:

$$\begin{aligned}
\kappa_m(0) &= 1 \\
p_B(0) &= p_\infty + 2
\end{aligned} \tag{3.105}$$

3.4.c Dissolution of two dimensional bubbles

The limiting case of a bubble that is distorted so that it is long in one direction is an infinite cylindrical bubble, which can be used to approximate the case of a bubble where variations in the long direction are small. Thus a polar coordinate system can be

used to model a bubble stabilized on a long, narrow, scratch-like crevice. A free cylindrical bubble is not physically realistic but is the starting point for the analysis.

For the case of a two-dimensional (cylindrical) bubble the potential flow solution method cannot be applied in a straightforward manner, because the potential does not vanish at infinity; however, the spherical bubble analysis suggests that the effect of the viscous stress will not be important for the experimental liquids, and, therefore it is neglected. The dynamic boundary condition for a cylindrical bubble becomes

$$\left(p_B^* - p_\infty^*\right) = \frac{\gamma}{R^*} \tag{3.106}$$

Because small velocities are expected, advection is neglected again, so, for the one dimensional cylindrical system,

$$\frac{\partial c^*}{\partial t^*} = \frac{D}{r^*} \frac{\partial}{\partial r^*}\left(r^* \frac{\partial c^*}{\partial r^*}\right) \tag{3.107}$$

In cylindrical coordinates, neglecting the motion of the bubble surface, and applying the same boundary and initial conditions as before, Eqs. (3.86) and (3.88), yields the concentration gradient at the surface

$$\left.\frac{\partial c^*}{\partial r^*}\right|_{R^*} \approx -4 \frac{H(p_B^* - p_\infty^*)}{\pi^2 R^*} \int_0^\infty \frac{\exp\left(-Dt^*\big/_{R^{*2}} \tau^2\right)}{\tau\left[J_0^2(\tau) + Y_0^2(\tau)\right]} d\tau \tag{3.108}$$

where Eq. (3.108) is found by Laplace transform, J_0 and Y_0 are Bessels functions, and Eq. (3.108) must be numerically evaluated (Carslaw and Jaeger 1959).

Species conservation for the bubble requires at the bubble surface

$$\frac{d}{dt^*}\left(R^{*2} c_B^*\right) = 2R^* D \left.\frac{\partial c^*}{\partial r^*}\right|_{R^*} \tag{3.109}$$

so that Eqs. (3.108) and (3.109) are combined to get

$$2\dot{R}^{*}Rc_{B}^{*} + R^{*2}\dot{c}_{B}^{*} = -\frac{8}{\pi^{2}}DH(p_{B}^{*} - p_{\infty}^{*})\int_{0}^{\infty}\frac{\exp\left(-Dt^{*}/R^{*2}\,\tau^{2}\right)}{\tau\left[J_{0}^{2}(\tau) + Y_{0}^{2}(\tau)\right]}d\tau \qquad (3.110)$$

Combining Eq. (3.110) with the equation of state and its time derivative to eliminate bubble gas concentration terms, and with the dynamic boundary condition and its time derivative to eliminate bubble pressure terms, rearranging, and nondimensionalizing as before,

$$\dot{R} = -\frac{8}{\pi^{2}}\frac{\Pi_{1}}{R(2p_{\infty}R + 1)}\int_{0}^{\infty}\frac{\exp\left(-\dfrac{t}{\Pi_{2}^{2}R^{2}}\,\tau^{2}\right)}{\tau\left[J_{0}^{2}(\tau) + Y_{0}^{2}(\tau)\right]}d\tau \qquad (3.111)$$

with initial condition

$$R(0) = 1 \qquad (3.112)$$

Note that the problem depends on the same three parameters as the previous cases.

Following the method used to extend the free spherical bubble to the sphere cap/ crevice bubble, Eq. (3.106) is rewritten as

$$(p_{B} - p_{\infty}) = \kappa, \qquad (3.113)$$

and Eq. (3.108) as

$$\bar{n}'' \approx 4\frac{HD(p_{B} - p_{\infty})}{\pi^{2}R_{eq}}\int_{0}^{\infty}\frac{\exp\left(-Dt/R_{eq}^{2}\,\tau^{2}\right)}{\tau\left[J_{0}^{2}(\tau) + Y_{0}^{2}(\tau)\right]}d\tau \qquad (3.114)$$

where now R_{eq} is defined as the average distance from the center of the crevice mouth to the bubble surface, which is expressed nondimensionally as

$$R_{eq} = \frac{\int_{-\sin^{-1}(\kappa)}^{\sin^{-1}(\kappa)}\sqrt{2 - \kappa^{2} - 2\cos(\theta)\sqrt{1 - \kappa^{2}}}\,d\theta}{2\kappa\sin^{-1}(\kappa)} \qquad (3.115)$$

Note that R_{eq} goes from unity when $\kappa = 1$, to ½ as κ approaches zero, just as the sphere cap equivalent radius does.

For the crevice topped with a circular section bubble,

$$\frac{d}{dt^*}\left[\left(A_B^* + A_C^*\right)c_B^*\right] = -\bar{n}''^* S_B^*$$ (3.116)

A_B^* is the cross sectional area of the bubble outside the crevice, A_C^* is the cross sectional area of the crevice, and S_B^* is the arclength of the surface of the bubble cross section. Nondimensionalized with R_o one has

$$\theta = 2\sin^{-1}(\kappa)$$
$$A_B = \frac{\theta - \sin\theta}{2\kappa^2}$$ (3.117)
$$S_B = \frac{\theta}{\kappa}$$

Equation (3.116) becomes Eq. (3.118), which is a model for dissolution of a bubble in a long surface scratch:

$$\dot{\kappa} = -\frac{8}{\pi^2}\Pi_1 \frac{\sin^{-1}(\kappa)}{R_{eq}\left(\psi + A_B + A_C\right)} \int_0^\infty \frac{\exp\left(-\frac{t}{\Pi_2^2 R_{eq}^2}\tau^2\right)}{\tau\left[J_0^2(\tau) + Y_0^2(\tau)\right]}d\tau$$ (3.118)

where

$$\psi = \frac{2\kappa\left(p_\infty + \kappa\right)\left(1 - \cos\left(2\sin^{-1}\kappa\right)\right) + \left(2p_\infty + \kappa\right)\left(\sin\left(2\sin^{-1}\kappa\right) - 2\sin^{-1}\kappa\sqrt{1-\kappa^2}\right)}{2\kappa^3\sqrt{1-\kappa^2}}$$ (3.119)

3.4.d Far wall effects on dissolution

The presence of walls increases nuclei persistence in ways other than just providing a crevice. Walls will hinder diffusion, which will allow even free bubbles near the wall to persist for longer times. To get an idea of how much of an effect this will have on bubble life the following rough approximation is used. Consider a crevice stabilized cylindrical bubble on one of two parallel walls separated by a distance d^*.

When the diffusion penetration depth, $\delta = (\pi D t^*)^{1/2}$, has not reached the other wall, the solution is still the solution to the bubble diffusing into a semi-infinite domain, so Eq. (3.118) applies for times less than t_δ, where

$$t_\delta = \frac{\Pi_2^2 (d-h)^2}{\pi}$$

(3.120)

and h, the distance from the plane of the wall to the furthest point on the bubble, is

$$h = \frac{1 - \sqrt{1-\kappa^2}}{\kappa}$$

(3.121)

For times sufficiently greater than t_δ the components of the concentration gradients at the bubble surface in the direction perpendicular to the walls will essentially vanish. A conservative approach to including this effect is to say that for $t \gg t_\delta$, the effective arclength for diffusion from the bubble is reduced from S_B to the projection of S_B perpendicular to the walls. This results in replacing S_B in Eq. (3.116) with $2h$

$$\dot{\kappa} = -\frac{8}{\pi^2} \Pi_1 \kappa \frac{1-\sqrt{1-\kappa^2}}{R_{eq}(\psi + A_B + A_C)} \int_0^\infty \frac{\exp\left(-\dfrac{t}{\Pi_2^2 R_{eq}^2} \tau^2\right)}{\tau \left[J_0^2(\tau) + Y_0^2(\tau)\right]} d\tau$$

(3.122)

This approach is conservative because it neglects the effective reduction in cylindrical "spreading" due to the presence of the wall. The incorporation of this effect in modeling the dissolution of a cylindrical crevice stabilized bubble into a bounded domain was accomplished by replacing Eq. (3.118) with Eq. (3.122) for $t > 10 \, t_\delta$.

3.4.e Results of bubble dissolution analysis

Figure 26 and Figure 27 compare nondimensional R or κ for free or crevice bound bubbles respectively as functions of dimensional time for the four categories of bubbles in PDMS and PB, with dimensional $R_o = 10 \ \mu m$ and $p_\infty = 101$ kPa. The crevice volume
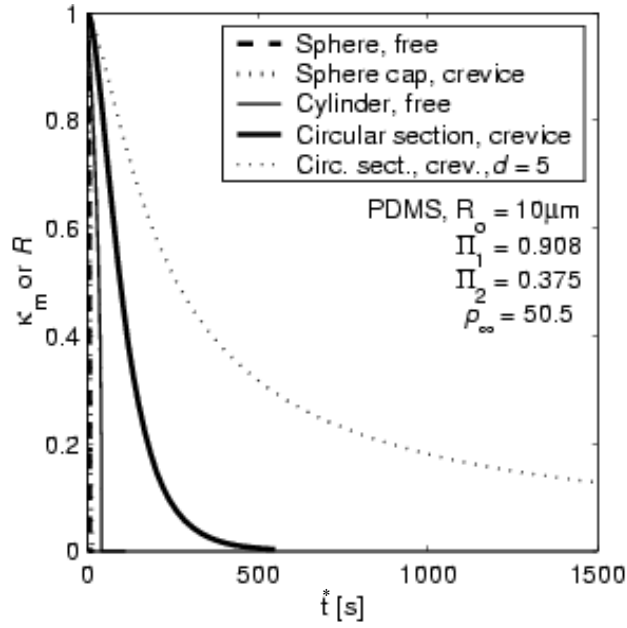
Figure 26. Plot comparing bubble dissolution in PDMS. The vertical axis is the nondimensional radius ($R = R^*/R_o$) or curvature $\kappa_m = \kappa_m^* R_o$, while the horizontal axis is the dimensional time.
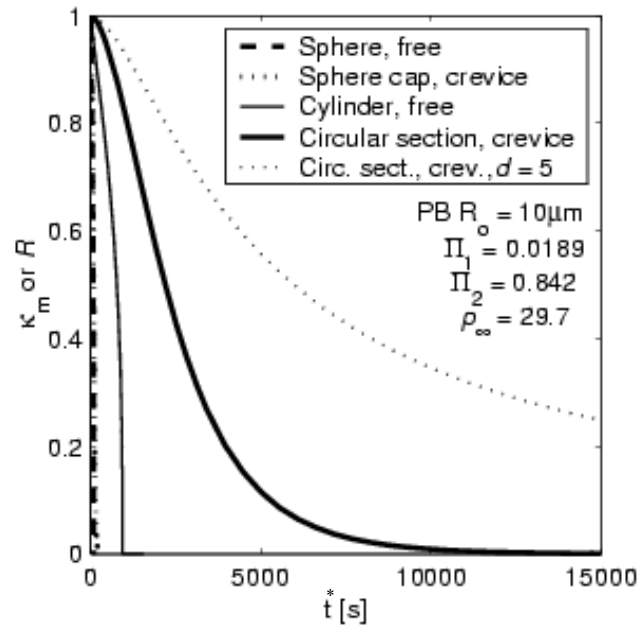
Figure 27. Plot comparing bubble dissolution in PB. The vertical axis is the nondimensional radius ($R = R^*/R_o$) or curvature $\kappa_m = \kappa_m^* R_o$, while the horizontal axis is the dimensional time.

and area are calculated assuming a cone or triangle with base angle of $\pi/2$. For the case of a bounded domain, $d = 5$. The liquid properties used in the figures are in Table I.

The conclusion drawn from the analyses is that wall-crevice stabilized gas nuclei with positive curvature can persist for long periods of time provided they form in scratch-like crevices. Confinement of the liquid to a gap whose thickness is not too much greater than the crevice width greatly retards the rate of curvature decrease.

3.5   THEORY AND SIMULATION - MIGRATION AND GROWTH

Once a bubble has detached from a nucleation site, its fate can be considered the result of the linked processes of migration, deformation, and advection/diffusion controlled growth or dissolution. Bubble shedding is necessary but not sufficient for cavitation inception; it must be followed by subsequent growth.

The lateral motion of a droplet or bubble in the presence of a shear flow near a wall has been studied analytically (Leal 1980), numerically (Uijttewaal *et al*. 1993), and experimentally (Smart and Leighton 1991), with the general result being that deformable droplets move laterally away from a wall in shear flow. A recent work looks at higher order solutions and finds a range of viscosity ratios for which the direction of migration can change (Magnaudet *et al*. 2003); however, the inviscid bubble is well outside this range. As droplet deformation increases (i.e., at higher Ca) the rate of lateral migration increases. Also, most of the studies report that the rate of migration decreases as the square of separation distance between the wall and droplet increases. Therefore, it is to be expected that shed bubbles will move away from the wall towards the center of the shear flow.

An approximate model for bubble growth accurate for bubbles that have migrated far from the wall and whose cross-stream dimensions are small as compared to L is a bubble in an infinite shear flow. Crowdy developed a model for the transient deformation of a compressible bubble in infinite shear with an arbitrary time dependent bubble pressure (Crowdy 2003). The model is an extension of the work of Richardson, who transformed the steady state problem into a boundary value problem in analytic function theory (Richardson 1968), and the work of Tanveer and Vasconcelos, who developed a class of exact solutions applicable to bubble pressures of zero (Tanveer and Vasconcelos 1995). Although the variation of bubble pressure in Crowdy's model is ostensibly for investigation of effects of the gas equation of state, it is an ideal formulation for linking the fluid mechanics model to a mass transfer model, by varying the bubble pressure due to changes in both area and mass. Crowdy's model yields a time dependent conformal mapping from the unit circle in the complex plane to the free bubble surface

$$z\left(\zeta, a(t), b(t)\right) = \frac{a(t)}{\zeta} + b(t)\zeta \tag{3.123}$$

The mapping is found by numerically solving a pair of coupled ordinary differential equations, Eqs. (3.9) and (3.10) in Crowdy's paper, repeated here for convenience

$$\dot{a} = -aI\left(0, a, b\right) - \left(\frac{p_\infty^C - p_b^C}{2}\right)a \tag{3.124}$$

$$\dot{b} = -bI\left(0, a, b\right) + \left(\frac{p_\infty^C - p_b^C}{2}\right)b + ik\left(a - b\right) \tag{3.125}$$

with

$$I\left(0, a, b\right) = \frac{1}{4\pi i} \oint_{|\zeta|=1} \frac{d\zeta}{\zeta} \frac{1}{\left|z_\zeta\left(\zeta, a, b\right)\right|} \tag{3.126}$$

Mass transfer is incorporated by including a third equation for the bubble pressure, obtained by differentiating the equation of state with respect to time. Scaled, this gives

$$\dot{p}_B^C = HR_u T p_\infty^C \left(-N_B^C \frac{\dot{A}_B^C}{A_B^{C2}} + \frac{\dot{N}_b^C}{A_B^C} \right) \tag{3.127}$$

The superscript C emphasizes that the scaling is done in accordance with Crowdy's scales: the length scale is the original bubble radius; the pressure scale is the associated Laplace pressure; the time scale is the dynamic viscosity divided by the pressure scale; and the velocity scale is the length scale divided by the time scale. In Eq. (3.127) N_B^C, the number of moles of gas per unit depth, is scaled consistently ($N_s = Hp_\infty R_o^2 L^2$), R_o is the initial (equivalent) bubble radius scaled by L, $Ca_L R_o$ is the same as Crowdy's k, and Ci and Crowdy's p_∞^C are related by $p_\infty^C = Ci Ca_L R_o$. If the initial bubble is not a circle with $p_B^C = p_\infty^C + 1$ then we define the scaled initial equivalent radius R_o to be

$$R_o = \sqrt{\frac{p_B^C(t=0)}{\pi\left(p_\infty^C + 1\right)}} \tag{3.128}$$

or equivalently

$$R_o = \sqrt{\frac{1}{Ci^2 Ca_L^2} + 4\frac{p_B}{\pi Ci} + \frac{1}{Ci Ca_L}} \tag{3.129}$$

$R_o L$ is the radius of a circular bubble with the same number of moles of gas per unit depth as the bubble being simulated, but at mechanical equilibrium in a quiescent liquid.

The determination of the rate of change of the number of moles of gas (per unit depth) in the bubble depends upon the mass transfer model. If the system has a sufficiently high Peclet number then once again a good model is the "penetration model" in which the mass transfer is calculated based upon the assumption that a quasisteady

concentration boundary layer surrounds the bubble (Bird *et al.*, 2002). For such a case, in terms of Crowy's scaling, Eq. (3.31) becomes

$$\dot{N} = 2F \left(\frac{k}{\text{Pe}_L} \right)^{\frac{1}{2}} \left(1 - \frac{p_B^C}{p_\infty^C} \right) \left(u_{\max}^C S_B^C \right)^{\frac{1}{2}}$$ (3.130)

Again F is set to unity for calculations. The factor of two accounts for the presence of two boundary layers for a free bubble, and S_B is now half the bubble circumference. A scaling analysis of bubble growth and dissolution in shear performed by Favelukis *et al.* looked at the same model, in essence, in the asymptotic limits of Ca → 0 and Ca → ∞ for three-dimensional bubbles (Favelukis *et al.* 1995). Note that the requirement of a high Peclet number is not met for all shed bubbles in the simulations, the relevant definition of Peclet number being $u_{\max} S_B / D$. Using Crowdy's model without any mass transfer, Peclet numbers fall into the range of 1 – 1000, with higher Peclet numbers occurring later in time and for higher Ca. Nevertheless, consideration is limited to either the penetration model for mass transfer, or to the impermeable liquid limit.

It is helpful to first consider the response of a bubble to shear in the absence of mass transfer (Pozrikidis 2001b; Crowdy 2003). Two-dimensional bubbles that are initially circular deform through a series of elliptical shapes. If a bubble is initially in mechanical equilibrium, $p_B^C(0) = p_\infty^C + 1$, it will first be compressed, and then it will expand; the final pressure is always less than the initial pressure. The reduction in pressure is greater for bubbles with higher k (=$\text{Ca}_L R_o$) and lower p_∞^C (=$Ci\text{Ca}_L R_o$).

One can use Crowdy's model without mass transfer (isothermal ideal gas equation of state) to consider the fate of shed bubbles in the impermeable liquid case. The simulation of bubble shedding in an impermeable liquid depicted in Figure 16 is used as a

basis for the initial conditions for the demonstrative example depicted in Figure 28. The shed bubble increases in apparent length, max (x_1)-min(x_1), by almost an order of magnitude; therefore the full event from bubble shedding through shed bubble deformation can be considered a cavitation inception event. The final bubble shape is sheet like, which agrees with experimental observations.

It can be deduced that a bubble must eventually dissolve if at steady state

$$p_B^C > p_\infty^C c_\infty^C \qquad (3.131)$$

where the concentration far from the bubble, c_∞, has been scaled by Hp_∞: c_∞ is one for a gas saturated system, less than one for an under saturated system, and greater than one for a supersaturated system. It is found through solution of Crowdy's model that for two-dimensional bubbles, for all combinations of k, p_∞^C, and $p_B^C(0)$, $p_B^C > p_\infty^C$ ($p_B > Ci$) at steady state. For instance, in the case depicted in Figure 28, $p_B \to 1.125Ci$ $\left(p_B^C \to 1.125 p_\infty^C\right)$. It seems that dissolution must eventually occur for shed bubbles unless the liquid is supersaturated with gas.

In order to implement the penetration model for mass transfer, it is necessary to calculate the tangential velocity on the bubble surface to determine u_{max}. The means by which this is done, within the framework of Crowdy's method to determine the bubble deformation, is not immediately apparent.

In deriving Eqs. (3.123)-(3.126), Crowdy begins by expressing the velocities in terms of analytic Goursat functions f and g

$$\begin{aligned}
u_1(z) &= \mathrm{Re}\left(-f(z,t) + z\overline{f}'(\overline{z},t) + \overline{g}'(\overline{z},t)\right) \\
u_2(z) &= \mathrm{Im}\left(-f(z,t) + z\overline{f}'(\overline{z},t) + \overline{g}'(\overline{z},t)\right) \\
z &= x_1 + ix_2
\end{aligned} \qquad (3.132)$$
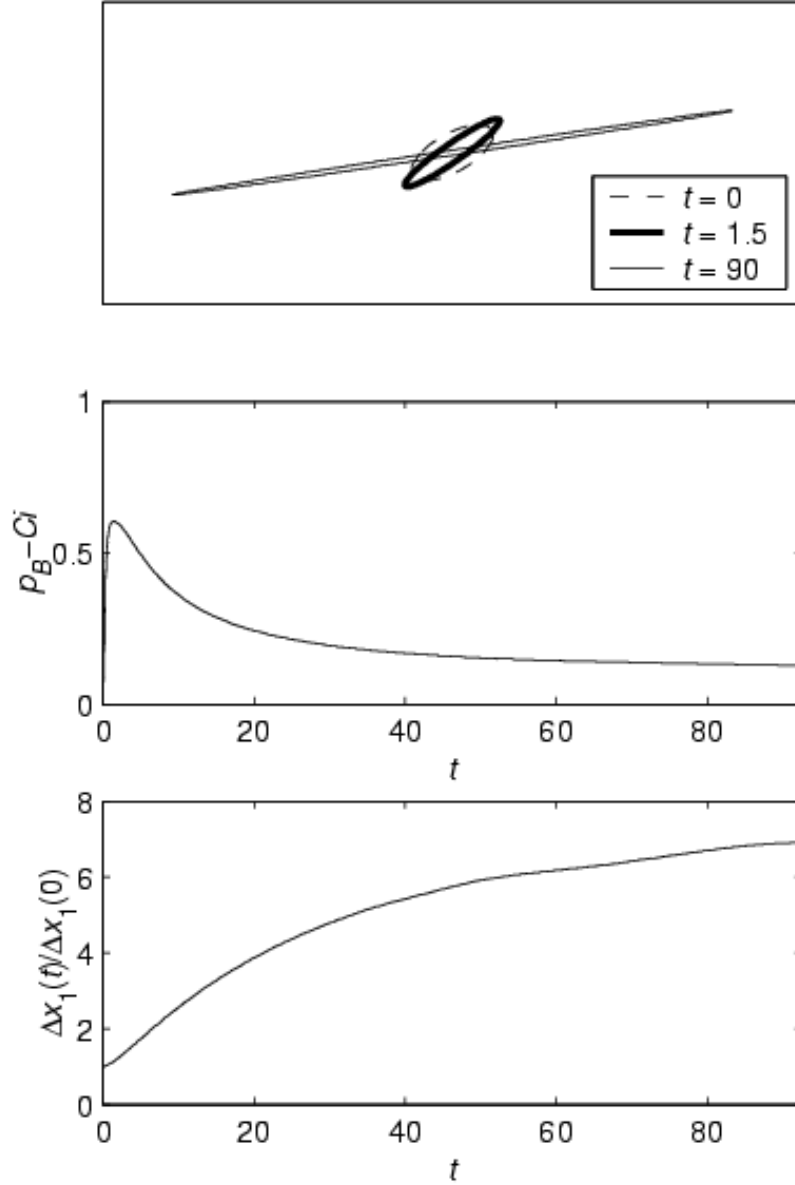
Figure 28. Bubble deformation in an impermeable liquid, Ca$_L$ = 100, *Ci* = 1. The initial conditions are based on the simulation depicted in Figure 16. The initial pressure is the pressure in the void at pinch-off in that simulation (*t* = 4.3) and the initial shape is an ellipse with the same area as the area that was detached from the crevice stabilized void (shown in the last frame of Figure 16). The top frame shows the bubble shape at three times *t*: the initial shape (dashed line), the shape at the time of maximum compression *t* = 1.5 (thick line), and the steady state shape (thin line). The middle frame shows the variation of bubble pressure with time: $p_B - Ci$ approaches 0.125. The bottom frame shows the evolution of apparent bubble length to an observer looking down from the x_2 direction. The apparent bubble length increases by almost an order of magnitude due to deformation.

These expressions can be simplified using the expression of the stress boundary condition in terms of the Goursat functions

$$f(z,t) + z\overline{f}'(\overline{z},t) + \overline{g}'(\overline{z},t) = -i\frac{z_s}{2} + \frac{p_B(t)}{2} \tag{3.133}$$

where subscript s indicates on the bubble surface. The simplified expression for the velocity on the bubble surface, written in a more succinct manner, is

$$u_1(z_s) + iu_2(z_s) = -2f(z_s,t) - i\frac{z_s}{2} + \frac{p_B(t)}{2} \tag{3.134}$$

During the solution process, the bubble pressure will be known at each time; therefore, to find the velocity on the bubble surface, two values must be determined: z_s and $f(z_s,t)$. The first is simple, as Crowdy has already derived an expression

$$z_s = \frac{i\zeta z_\zeta}{|z_\zeta|} \quad \text{on } |\zeta| = 1 \tag{3.135}$$

Recall that the mapped bubble surface in the complex plane is the curve of $|\zeta| = 1$. The derivative of the conformal mapping, Eq.(3.123), is used to obtain

$$z_\zeta(\zeta, a(t), b(t)) = -\frac{a(t)}{\zeta^2} + b(t) \tag{3.136}$$

So it is only necessary to find f based on the values found during the solution process: a, b, and p_B and their time derivatives. By working backwards through Crowdy's derivation, the sought after relationship can be shown to be

$$f(z,t) = \frac{1}{2}\left(\frac{p_B(t)z}{2} - \frac{\dot{a}}{\zeta} - \dot{b}\zeta + \left(b\zeta - \frac{a}{\zeta} \right)\left[I(\zeta,t) - i\frac{k}{2} \right] \right) \tag{3.137}$$

where I is the complex contour integral

$$I(\zeta,t) = \frac{1}{4\pi i}\oint\limits_{|\zeta|=1} \frac{d\zeta'}{\zeta'}\left[\frac{\zeta'+\zeta}{\zeta'-\zeta} \right]\frac{1}{|z_\zeta(\zeta,t)|} \tag{3.138}$$

To find the maximum tangential component of the velocity on the bubble surface at a given time t, the parametric description of the conformally mapped bubble surface in the

99

complex plane is used, $\zeta = e^{i\phi}, 0 \le \phi \le 2\pi$. The parametric interval is discretized into 1024 intervals and the velocity is found on half (due to symmetry) of them using Eq. (3.134)-(3.138). The tangential components of the velocities are compared to determine u_{max}. The difficulty arises because the integral in Eq. (3.138) is singular for points on the bubble surface, and therefore must be handled carefully, as follows (Crowdy 2004).

The Plemelj formula for Cauchy type integrals of the form,

$$J(\zeta) = \frac{1}{2\pi i} \oint_C \frac{h(\zeta',\zeta)}{\zeta'-\zeta} d\zeta' \qquad (3.139)$$

is

$$J(\zeta) = \frac{h(\zeta;\zeta)}{2} + \frac{1}{2\pi i} \oint_C^{PV} \frac{h(\zeta';\zeta)}{\zeta'-\zeta} d\zeta' \qquad (3.140)$$

where now the integral is interpreted in the principal value sense. The corresponding form of Eq. (3.138) is

$$I(\zeta,t) = \frac{1}{2|z_\zeta(\zeta,t)|} + \frac{1}{4\pi i} \oint_C^{PV} \frac{d\zeta'}{\zeta} \left[\frac{\zeta'+\zeta}{\zeta'-\zeta} \right] \frac{1}{|z_\zeta(\zeta,t)|} \qquad (3.141)$$

To numerically determine the principal value of the singular contour integral the alternate trapezoidal method is used due to its spectral accuracy (Shelly 1992).

Typical rates of dissolution are found using the same initial conditions used for the simulation shown in Figure 28, but incorporating the penetration model. For these examples, shown in Figure 29, the liquid is assumed to be gas saturated, $c_\infty = 1$, and the transport properties of PB and PDMS (Table I) with the experimental value $L = 50$ μm are the basis for choosing $HR_uT = 0.015$ and $Pe_L = 400$ (PB) and $HR_uT = 0.2$ and $Pe_L = 60$ (PDMS). Note that the simulations using the PDMS values for H and D are not simulations of PDMS as the fluid mechanics model assumed Newtonian constitutive

behavior. The results using the transport properties of PB show that for $t < 50$ there is little difference between the impermeable model and penetration model results; a reduction of the mass in the bubble by 20% has occurred by $t = 90$. The greater diffusivity and higher Henry's constant of PDMS result in enhanced mass transfer. When using those transport properties, the bubble shrinks more rapidly. By $t = 9$ the bubble modeled using PDMS properties has reached a maximum apparent length, and by $t = 17$ it has lost sufficient mass that its pressure begins increasing. The pressure increase occurs as the capillary number based on equivalent radius R_o decreases and the shear flow loses its ability to deform the bubble. The bubble returns to a more circular shape and as it loses mass, and its curvature increases, resulting in higher bubble pressures and greater driving gradient for mass transfer. The mass transfer is higher than it would be in a quiescent liquid due to advection effects, and once the pressure begins to increase, the bubble quickly disappears.

If the liquid is supersaturated, $c_\infty > 1$, then the bubble may grow. Recall that the bubble shedding example using the penetration model, Figure 17, used a supersaturated liquid, $c_\infty = 1.16$ and $Pe_L = 1000$. The ellipse shown in the final frame of Figure 17, and the pressure at the pinch-off time for the simulation used to generate Figure 17 were used as the initial conditions for a simulation of bubble deformation and growth in a supersaturated solution, $c_\infty = 1.16$. The results of the simulation, shown in Figure 30, are an example of bubble deformation leading to unstable growth. At $t = 16$, the bubble pressure is equal to the far field pressure times the degree of saturation c_∞, and the number of moles of gas per unit depth is at a global minimum. For all times $t > 16$ the mass flux will be into the bubble, increasing its capillary number based on equivalent
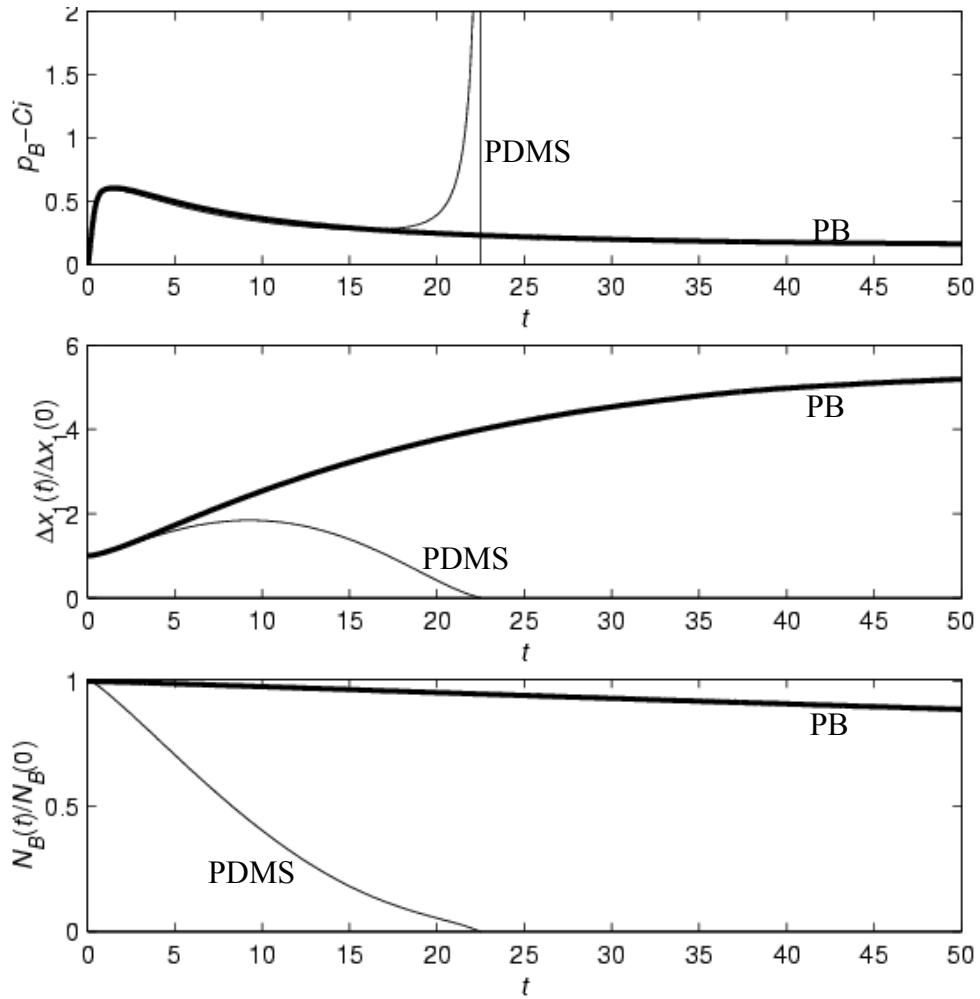
Figure 29. Bubble deformation using the penetration model, Ca$_L$ = 100, *Ci* = 1, c_∞=1. The initial conditions are based on the simulation depicted in Figure 16. The initial pressure is the pressure in the void at pinch-off in that simulation (*t* = 4.3) and the initial shape is an ellipse with the same area as the area that was detached from the crevice stabilized void (shown in the last frame of Figure 16). Two cases are shown, one using PB transport properties (thick lines) and the other using PDMS properties (thin lines). The top frame shows the variation of bubble pressure with time; the middle frame the evolution of apparent bubble length to an observer looking down from the x_2 direction, and the bottom frame the variation of the number of moles of gas per unit depth in the bubble with time. The simulation using PB properties is very close to the impermeable liquid model (Figure 28) for the time range shown, although it will eventually dissolve. The bubble simulated using PDMS properties dissolves rapidly.
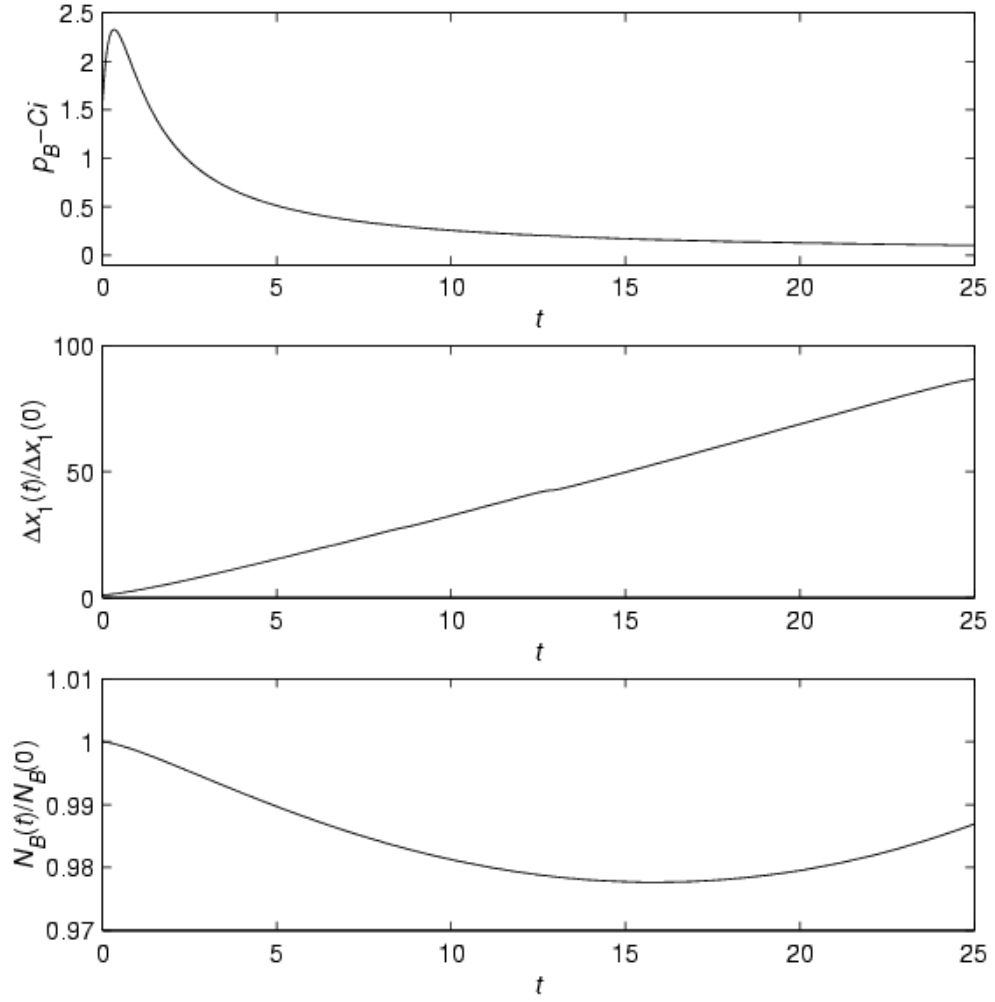
Figure 30. Deformation and growth of a shed bubble in a gas supersaturated liquid. Initial conditions are based on the inception simulation using the penetration model and leading to a shed bubble (Figure 17). The parameters for the simulation of bubble growth and deformation using the penetration model are Pe_L=1000, $HR_uT = 0.025$, $Ci = 1$, and $Ca_L = 100$. After $t = 16$ the mass transfer is into the bubble, resulting in ever increasing apparent bubble length.

radius, and hence lowering the pressure that the bubble would reach at steady state in the absence of mass transfer. This results in a positive feedback loop, where mass flux into the bubble increases the driving gradient for mass transfer. The apparent bubble length increases enormously. Physically, this cycle would be ended by depletion of the dissolved gas in solution in the liquid.

3.6   MECHANICAL RESPONSE - THE LINK TO THE PNSCC

The mechanical response of wall stabilized nuclei to pressure changes, neglecting contact line motion, sheds considerable light on the linkage between the simulations and experimental results. Increases in pressure result in a reduction of the height of the bubble above the wall, h, and if h for a given site is driven below zero then the site will be deactivated, i.e., it will not shed a bubble regardless of the shear stress is applied. Similarly, sites that would not have shed bubbles can be activated through pressure reduction. The mechanical response of a nucleation site depends upon the initial bubble volume, the crevice geometry, and the contact line dynamics, θ_A and θ_R.

Consider a bubble with positive curvature and pinned contact lines. The length scale is still the channel cross section, L. The bubble initially has a dimensionless height h_o and is above a crevice of dimensionless width W and cross sectional area A_C. The dimensionless curvature of the bubble κ is given by

$$\kappa = \frac{8h}{W^2 + 4h^2} \qquad (3.142)$$

The pressure in the bubble, scaled by γ/L, is

$$p = p_\infty + \kappa \qquad (3.143)$$

The total cross sectional area of the bubble A_B is given by

$$A_B = A_C + A_B' \qquad (3.144)$$

if $h < 1/\kappa$, and by

$$A_B = A_C + \frac{\pi}{\kappa^2} - A'_B$$ (3.145)

if $h > 1/\kappa$, where

$$A'_B = \frac{\omega - \sin\omega}{2\kappa^2}$$ (3.146)

and

$$\omega = 2\arcsin(\kappa)$$ (3.147)

The isothermal mechanical response of the bubble to a pressure change from p_o to p_f is governed by the ideal gas equation of state expressed as

$$p_f A_{B,f} = p_o A_{B,o}$$ (3.148)

and by the requirement that Eqs. (3.142) to (3.147) hold for the bubble in its initial and final state.

Recalling that smaller crevice volumes promote pinch-off it seems likely that the cavitation events observed experimentally originated from shallow crevices. In general, the smaller the bubble volume, the less it will respond to pressure increases. The experimental results with PB are replotted as h vs p by assuming that the observed inception of cavitation occurred at $Ca_L h = 0.64$ (Figure 31). Using the data points at $p = 100$ kPa to set a reference $h(p=100 \text{ kPa}) = h_o$, curves can be generated for a given A_C and W showing the mechanical response of a bubble to pressure changes. The curves in Figure 31 are for $W = 0.1$ and $W = 0.025$.in the limit of crevice cross sectional area $A_C = 0$, and for $W = 0.1$ with $A_C = 10^{-4}$. The PB data, which supported a PNSCC with critical stress σ_c of zero, lies close to the curve for $W = 0.1$, $A_C = 0$.

3.7 DISCUSSION AND CONCLUSIONS

In this chapter a theoretically consistent picture has been presented, backed by simulation results, of cavitation inception from wall stabilized nuclei. Inception is subdivided into three separate events: nucleation site stabilization; bubble shedding; and shed bubble migration, deformation and growth. It is useful to tie these events and simulations into a coherent picture by summarizing and reconsidering the previous sections, and to ensure the limitations of the analysis are apparent.

The simulations of shear deformation of wall stabilized gas nuclei bring out several important concepts tempered by a number of significant assumptions. The most important assumption is that the two-dimensional model can capture the relevant physics. The two most important results are that nuclei must have positive curvature, i.e., be convex toward the liquid, for the deformation to lead to inception, and that within the realistic range of other parameters, deformation will lead to pinch-off when

$$\mathrm{Ca}_L h \sim 1 \tag{3.149}$$

Another result of the simulations is that, all other things being equal, the cavity with the smallest cross sectional area is most likely to deform to pinch-off. Considering, therefore, the mechanical response of sites with small A_C to pressure changes, one finds that in the range of pressures and crevice sizes considered, the height the bubble extends above the wall, h, is roughly inversely proportional to the applied pressure. Consequently, the criteria for pinch-off based on $\mathrm{Ca}_L h$ leads to a prediction that the shear stress needed for pinch-off is proportional to the pressure. If the proportionality constant is nearly unity then the PNSCC with $\sigma_c = 0$ is a good predictor of cavitation.
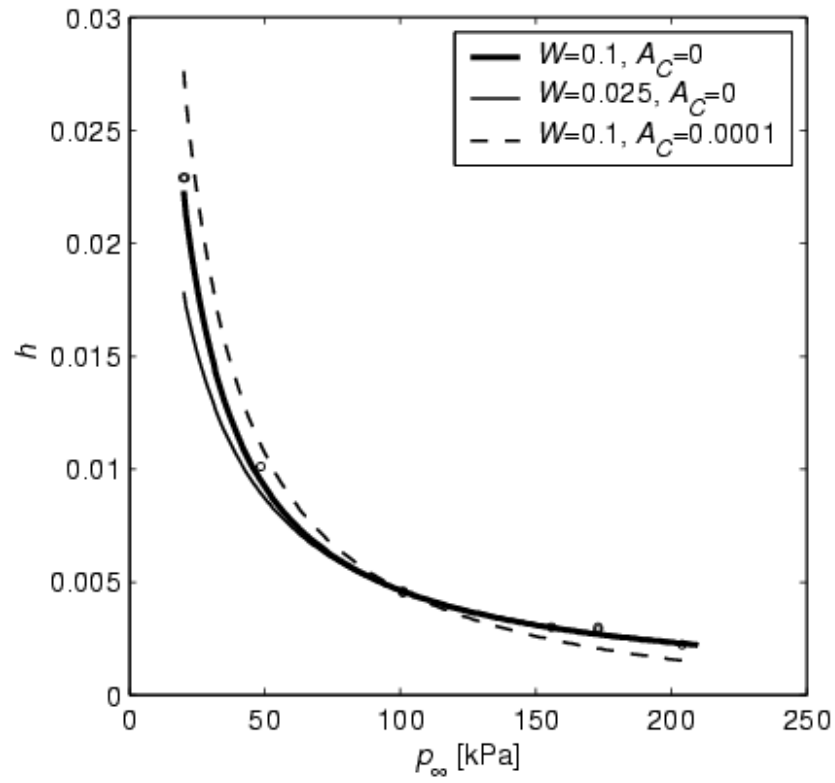
Figure 31. Mechanical response of critical void to pressure changes (lines) plotted against the (dimensionless) height that a given void would need to have based on experimental inception of cavitation, assuming inception occurs when Ca$_L$h = 0.64.

A final result of the bubble shedding simulations that is important to the overall picture is the role of mass transport. Three models were used, an impermeable liquid model, the quasisteady boundary layer, or penetration, model, and the infinitely fast diffusion model. The last is an extreme never closely approached physically, and therefore useful only in its elucidation of the role of diffusion. The first is quite frequently accurate as the bubble shedding process is relatively fast. The penetration model is appealing, but must be treated with caution, as its validity can only be tested with a more complete analysis. The effect of mass transport is to raise the required level of shear for pinch-off to occur, because mass transport will always mitigate the pressure rise during the initial compression of the bubble. If the liquid is supersaturated then mass transport can replenish a nucleation site after a bubble is shed. If the liquid is saturated then the simulations suggest that only a single shedding event will occur.

Next the persistence of nuclei with positive curvatures is considered, and, through an approximate analysis, it is found that it is likely for nuclei that approach the two-dimensional limit, especially when an opposing wall hinders diffusion. This provides an explanation for the type of voids typically seen in the experiments, and provides some support for the use of a two-dimensional model for inception.

The fate of shed bubbles is also considered. In this analysis a two-dimensional approximation is used yet again, which probably eliminates recognition of conditions for which the bubble would break up. The analysis uses the migration of deformable bubbles in shear away from walls, and the eventual slenderness of the deformed bubbles, as a justification for modeling the shed bubbles as deforming in an infinite shear flow. The analysis also considers diffusion only using the penetration model, which suffers once

again from the lack of a truly rigorous justification. Nevertheless, the results clearly demonstrate that shed bubbles deform considerably, becoming long and slender (sheet-like). The results also suggest that absent gas supersaturation, all shed bubbles will eventually disappear.

Despite the experimental investigation of both a Newtonian and a non-Newtonian liquid, the simulation results consider Newtonian behavior only. Further, the use of continuum theory for nucleation would not necessarily be valid for high molecular weight polymers even if the flow conditions would make a Newtonian assumption appropriate.

The modeling does not consider the initial creation of voids; however, this is not overly troubling as experimentally it is observed that voids are so prevalent as to be a major nuisance.

As a final caveat, although the demonstration of feasibility and consistency of our model that treats all major stages of bubble nucleation and agrees with experimental results is a convincing argument that this is a good theory, it is far from proof that this is the mechanism by which shear cavitation occurs, and other hypotheses could be argued as convincingly. There are further experiments that could be performed to test the validity of this model. In particular, it would be useful to see if degassing and pre-pressurizing the liquid prevents shear cavitation. Unfortunately, the experimental device described in the previous chapter was not designed with these operations in mind, and, in an attempt to implement such a series of experiments, the device was severely damaged.

CHAPTER 4

SHEAR CAVITATION – EXTRUSION DEFECT EXPERIMENT

During the extrusion of polymer melts, if the wall shear stress is high enough, the flow exhibits instabilities (Denn 2001). In general, the first sign of the onset of instability is a distortion of the extrudate surface. At higher shear stresses, the distortion becomes more pronounced, flow oscillation may occur, and the distortions may encompass the entire extrudate. Extrusion instabilities are described by various names, including shark-skin, loss-of-gloss, melt fracture, gross melt fracture, wall slip, stick slip, spurt flow, and elastic turbulence. The terminology is not used in an entirely consistent manner in the literature; however, melt fracture usually refers to a gross distortion of the extrudate while loss-of-gloss and shark-skin are surface defects. Stick slip refers to variations in flow rate for constant applied pressure, or in pressure drop for constant extrusion rate, while wall slip refers to an apparent breakdown of the no-slip condition.

The onset of stick slip places an upper limit on the shear stress for which rheological data can be measured using a capillary tube or similar type viscometer. The appearance of surface defects limits the rate of many polymer extrusion processes. Hence, there has been considerable research into the causes of extrusion instabilities with the goal of delaying or preventing their onset.

Although the causes of extrusion defects are still the subject of ongoing research, there are some areas of general agreement (Larson 1992). First, extrusion defects can be roughly categorized as either surface defects or gross defects. Gross defects, such as melt fracture, affect the entire flow, involve the entrance region, and appear to be due entirely to the constitutive behavior of the fluid. They occur at a critical level of molecular

orientation, i.e., a critical Weisenberg number, $Wi = \lambda\dot{\gamma} = \tau M/(\rho R_u T)$. Changes in the nature of the die surface do not seem to affect the onset of gross extrudate defects.

The onset of surface defects, on the other hand, does seem to depend upon the treatment of the die surface. A critical shear stress, usually reported to be about 0.1 MPa, is required, and the instability appears to initiate near the die exit (Hatzikiriakos 1994). The critical stress seems to be fairly constant over a wide range of temperatures and for many different liquids (Vinogradov *et al.* 1984). A loss of adhesion between the liquid and die wall is generally thought to be necessary for extrusion defect formation. If the loss of adhesion is accompanied, as seems likely, by the creation of a void between the liquid and the wall, then it is a form of cavitation.

Linking extrusion defects with cavitation is not an original concept. Simulations of the extrusion of PDMS using a finite element program have suggested that large negative pressures are generated near the die exit, which could lead to cavitation (Tremblay 1991). Vinogradov sought, with partial success, to halt extrusion defects by raising the hydrostatic pressure, an approach that would be suggested by an involvement of cavitation (Vinogradov 1967). Increased pressure stopped extrusion defects in cis-polyisoprene and cis-polybutadienes, but not in butyl rubber or sodium-butadiene rubber. Son and Migler obtained micrographs of apparent cavitation near the exit of transparent dies (Son and Migler 2002). They observed that for two linear low density polyethylenes (LLDPE) the onset of cavitation inside the capillary occurred at shear stresses nearly coincident with those for the onset of gross melt fracture, and higher than those for the onset of shark-skin defect. They consider, but reject, a role for shear stress in the

formation of the cavitation voids, concentrating instead on stresses imposed at the die entrance.

The role of cavitation in extrusion defects is not clear based upon current research. One possible hypothesis that would involve the PNSCC is that the loss of adhesion that is implicated in surface defects occurs near the exit and at a critical shear stress of about 0.1 MPa because that is where a principal normal stress would become tensile. The subsequent formation of a void at the wall would cause the adhesive failure thought to be necessary for surface defect formation. Because extrusion defects are only seen in non Newtonian liquids, normal stress differences would be expected to be involved; the pressure might be above atmospheric, based on the pressure gradient driving the flow. In this chapter, a strategy similar to that used to experimentally test the PNSCC is described. It is used to determine whether shear cavitation plays a role in extrusion surface defects. Instead of a variable pressure Couette viscometer and flow cell, a variable pressure capillary tube viscometer with video of the extrudate is used. The results suggest that cavitation is not necessary for surface defect formation during extrusion processes. Additionally, the capillary tube viscometer is used to obtain estimates of the first normal stress difference as a function of shear rate to ensure that the previously used model, Eq. (2.11), is reasonable.

4.1   APPARATUS AND METHODOLOGY

The experimental method is similar to that employed by Vinogradov; a capillary tube viscometer is used and observations of the extrudate are made for the same differential pressure across the capillary tube but different pressures in the exit chamber.
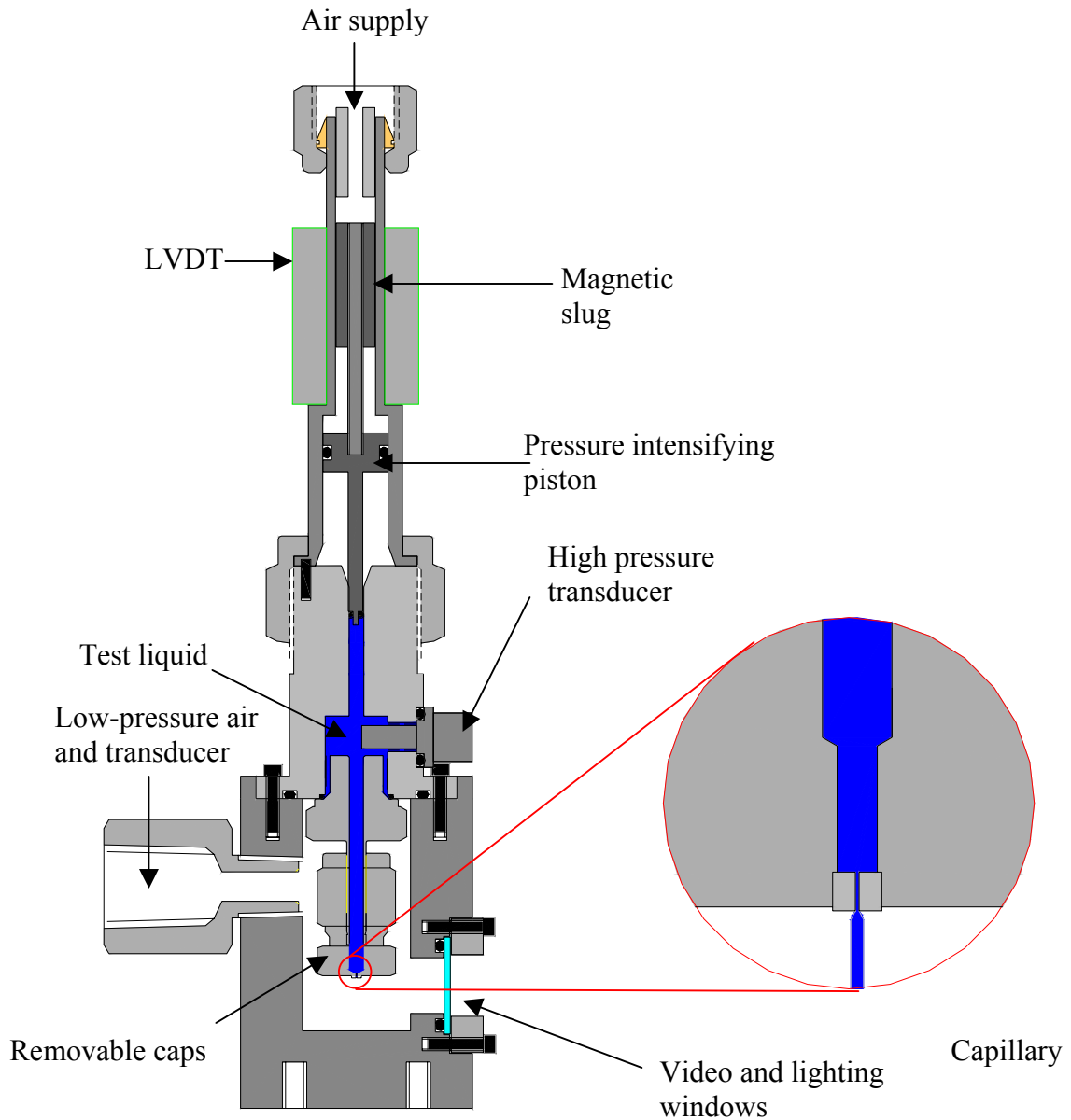
Figure 32. Extrusion defect experiment. An air driven piston raises test liquid pressure to a maximum of 20 MPa, forcing flow through a capillary. The flow rate is measured using an LVDT to determine the piston displacement. The pressure at the capillary outlet is varied between 8 and 275 kPa, and the pressures in the reservoir and outlet chamber are measured with transducers. Output is recorded with video images of the extrudate.

The capillary tube viscometer is of the controlled pressure type (Figure 32). Pressurized air is supplied to the large area side of a pressure-intensifying piston, which can produce pressures to 20 MPa in the liquid, measured by a high pressure transducer. The piston is linked mechanically to a magnetic slug whose position is detected by an LVDT, producing a signal that is differentiated with respect to time to obtain liquid flow rate. The pressure in the exit chamber is controlled using shop air or a vacuum pump and measured with a low pressure transducer; the absolute pressure range is 8 to 275 kPa. Sapphire windows allow lighting and imaging of the capillary exit. The fixtures containing the capillaries are exchangeable.

There were five stainless steel capillaries used with three test liquids. The polybutene (PB), H-1900, and polydimethylsiloxane (PDMS), DC-200-10^6, used in the Couette experiment were used, as was a solution of high molecular weight polyisobutylene supplied by BASF in decalin supplied by Fisher (PIB + dec). PB was used as a calibration fluid to determine capillary diameters (Novak 1968) whose characteristics are given in Table II.

The small diameters are necessary to avoid viscous heating, which affects the flow in a tube when the Nahme number,

$$Na = \frac{\beta \tau \dot{\gamma} D^2}{16k}$$

(4.1)

is greater than one (Macosko 1994) For the PB and PDMS for all experiments this

Table II. Capillary Dimensions [mm]					
	1	2	3	4	5
Length L	4.78	0.178	0.889	0.381	5.029
Diameter D	0.498	0.059	0.159	0.159	0.176
L/D	9.6	3.0	5.6	2.4	28.6

114

criterion is not exceeded. The thermal conductivity k and temperature coefficient of z

viscosity β were unknown for PIB+dec; to ensure that viscous heating did not affect the

flow, a flow curve was generated, using a method described shortly. Despite the short

capillary lengths, the flow entrance length, $L_E = 0.05\ D\ Re_D$, where Re_D is the Reynolds

number based on capillary diameter and mean velocity (Bejan 1993), is negligible for all

flow rates. In the experiments, the maximum L_E/L was 0.0005. The maximum Re_D was

0.025; therefore, the kinetic energy of the flow is negligible when calculating wall shear

stress, and the flow is clearly laminar.

Ideally the pressure difference, Δp_t, between the two transducers is the pressure

drop across the capillary, Δp_{act}, and given the ratio L/D for a given capillary, the wall

shear stress, τ_w, can be calculated from a simple force balance, yielding

$$\tau_w = \frac{\Delta p_{act}}{4(L/D)} \tag{4.2}$$

However, the pressure drop across the capillary could vary from the measured pressure

differences,

$$\Delta p_{act} = \Delta p_t - p_c \tag{4.3}$$

where the differential pressure must be corrected for pressure drop between the high

pressure transducer and the capillary entrance, pressure losses due to the convergent flow

from the reservoir to the capillary, and pressure at the exit of the capillary due to normal

stress differences (stored elastic energy) (Macosko 1994). An effective method to correct

for all of these is to obtain the required pressure drops to obtain a given flow rate Q for

two capillaries of different L/D (Novak 1968). Because the flow rates are the

same, the shear rates and therefore shear stresses are the same. Therefore, assuming that

the pressure correction is the same for the two capillaries,

$$\Delta p_t = \tau_w \left(4 \frac{L}{D} \right) + p_c \qquad (4.4)$$

The shear stress is the slope of a line through the two equal flow rate points plotted as Δp_t vs $4L/D$

$$\tau_w = \frac{\Delta p_{t1} - \Delta p_{t2}}{4 \left[\left(\dfrac{L}{D} \right)_1 - \left(\dfrac{L}{D} \right)_2 \right]} \qquad (4.5)$$

For a Newtonian liquid, the wall shear rate $\dot{\gamma}_{Nw}$ and the volumetric flow rate for laminar fully developed pressure driven flow through a tube, Poissuelle flow, are related by

$$\dot{\gamma}_{Nw} = \frac{32Q}{\pi D^3} \qquad (4.6)$$

For a non-Newtonian liquid, the Weissenberg-Rabinowitsch analysis is used to obtain the wall shear rate from the volumetric flow rate (Macosko 1994). Starting from the equation for the flow rate in fully developed pipe flow

$$Q = 2\pi \int_0^{D/2} u(r) r \, dr \qquad (4.7)$$

Integrating by parts, applying the no slip boundary condition and using the definition of the shear rate, $\dot{\gamma} = -\dfrac{\partial u}{\partial r}$, yields

$$Q = \pi \int_0^{D/2} \dot{\gamma} r^2 \, dr \qquad (4.8)$$

In fully developed Poisseulle flow the shear stress varies linearly with radial position

$$\frac{d\tau}{dr} = 2 \frac{\tau_w}{D} \qquad (4.9)$$

and this allows a change of variables in Eq. (4.8) to
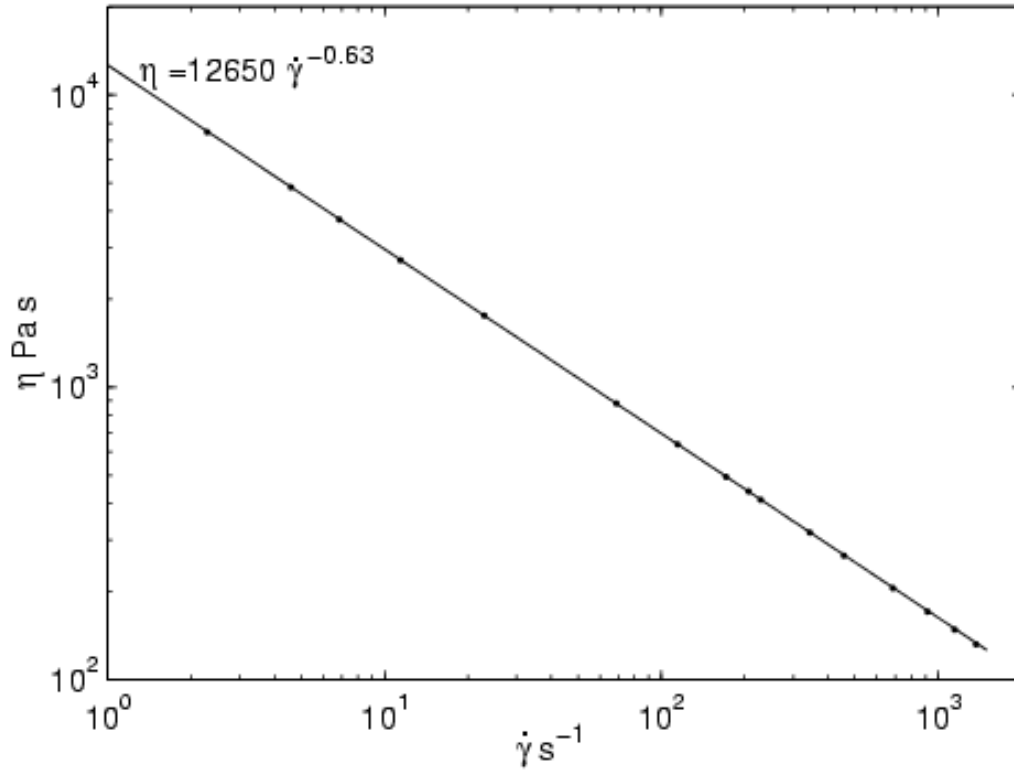
Figure 33. Flow curve for PIB+dec. The shear stress τ was obtained using Eq. (4.5), and the shear rate $\dot{\gamma}$ from Eq. (4.11). The apparent viscosity η is the ratio $\tau/\dot{\gamma}$. The data follows power law behavior, a good indicator that viscous heating is not affecting the results.

$$Q = \frac{\pi D^3}{8\tau_w^3} \int_0^{\tau_w} \dot{\gamma}\tau^2 d\tau \qquad (4.10)$$

Differentiation of Eq. (4.10) with respect to τ_w and rearrangement yields the Weissenberg-Rabinowitsch equation

$$\dot{\gamma}_w = \frac{\dot{\gamma}_{Nw}}{4}\left(3 + \frac{d \ln Q}{d \ln \tau_w}\right) \qquad (4.11)$$

The differential term in Eq. (4.11) is found by numerical differentiation of data.

Using capillaries 4 and 5 to obtain values of Δp_t for the same flow rate and different *L/D* to obtain τ_w using Eq. (4.5), and obtaining shear rates with Eq. (4.11), a flow curve was generated for PIB+dec (Figure 33). As can be seen, for all shear rates in the range available to this viscometer, the liquid is a power law liquid with *n* = 0.37 and shows no indications of viscosity reduction due to viscous heating.

The device was also used to generate viscosity data for PDMS, which is included on Figure 5. The close agreement with the Couette data is a good indicator that the calibration and analysis are correct.

4.2   RESULTS

In order to investigate the role of cavitation in extrusion defects, the test liquids were sheared while video of the extrudate is recorded. For shearing with the exit pressure at one atmosphere, a number of observations were made. For polybutene, no surface or gross defects were observed for any level of shear. For all liquids, bubbles were occasionally observed in the extrudate; however, they became less prevalent as the differential pressure increased, suggesting their origin is not cavitation (Figure 34).
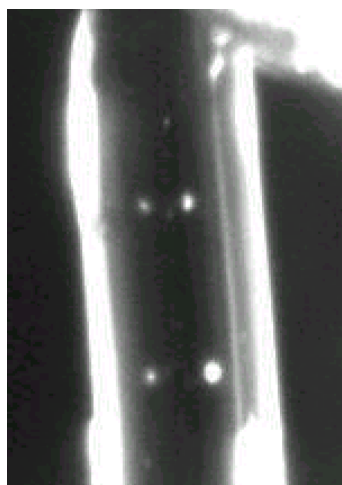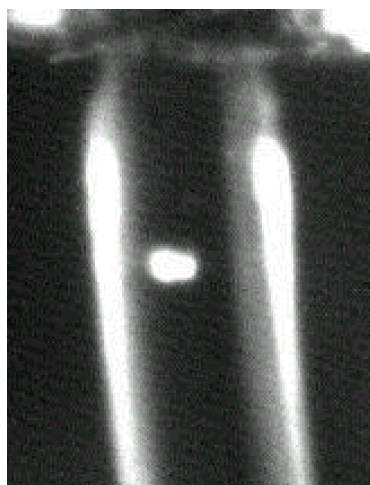
(a) τ = 15 kPa   (b) τ = 100 kPa

Figure 34. Bubbles observed in PB extrudate. The occurrence of bubbles is lower at higher differential pressure, suggesting that their origin is not cavitation.

For both PDMS and PIB+dec both surface defects and gross defects were observed (Figure 35 and Figure 36). For PDMS, the surface defect is a loss-of-gloss in which the extrudate surface becomes hazy and opaque. For PIB+dec the surface defect is a loss-of-gloss where the surface becomes dimpled in appearance. The onset of surface defects is gradual, and no critical stress can be given for its occurrence; however, it clearly occurs at a shear stress lower than the typically reported value of 0.1 MPa (see Figure 37 and Figure 38). Piau *et al.* reported similar results for lower viscosity silicone oils (Piau *et al.* 1990).

For both PDMS and PIB+dec, the gross defect is perhaps best described simply as a flow instability; it does not have the more chaotic appearance generally associated with melt fracture. The gross defects have a recognizable critical shear stress at which onset occurs or stops for increasing or decreasing shear stress respectively. The onset seems also to depend on capillary *L/D*. The instability did not appear for capillary 5, but was seen for capillary 4. For capillary 4 for PDMS the critical shear stress is 25 ± 3 kPa while for PIB+dec it is 15 ± 3 kPa. Based on the dependence of the flow instability on capillary length and the general consensus in the literature that gross instabilities are often due to stresses arising at the capillary inlet, it makes sense to compare liquid's residence time, $t_R = \pi L D^2 / 4Q$, to the liquid's characteristic relaxation time, λ, from Eq. (2.6). For PDMS λ is 0.07 s at 300 K while at the onset of the flow instability t_R is 0.025 s. At the same flow rate, for the longer capillary, t_R is 0.4 s. For PIB+dec, the predicted λ would need to be modified from Eq. (2.6) because the liquid is a solution, not a melt; however, the low shear viscosity, μ, needed for this calculation was not obtainable. All that can be said, using the highest viscosity observed, is that $\lambda > 4.8$ s. The residence time in the

120

| (a) No defects | (b) Loss-of-gloss | (c) Gross defect |
| $\tau = 5$ kPa | $\tau = 65$ kPa | $\tau = 25$ kPa |
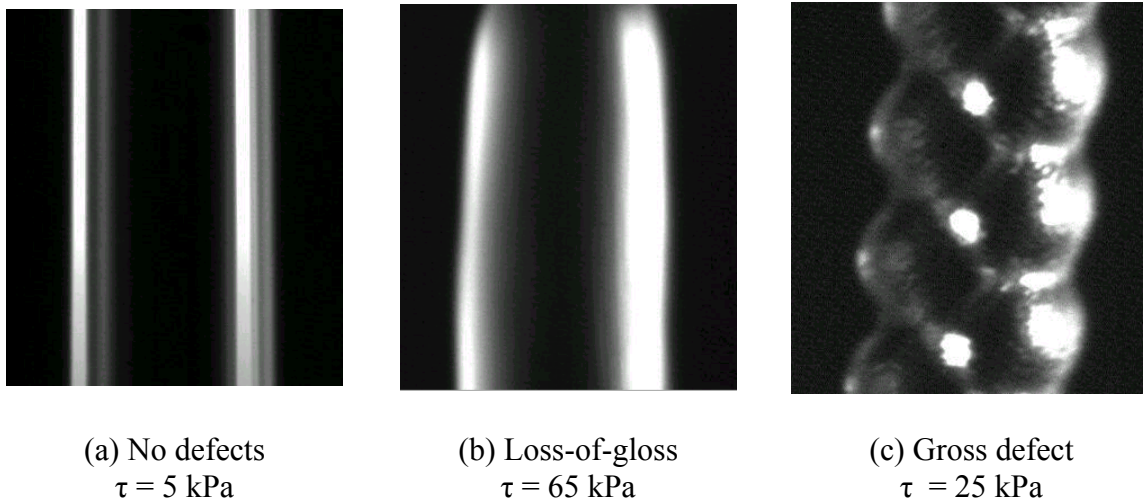
Figure 35. Extrudate defects observed for PDMS. The gross defect (c) was observed only from the shorter capillary, capillary 4, and not from capillary 5.

| (a) No defects | (b) Dimpling | (c) Gross defect |
| $\tau = 15$ kPa | $\tau = 36$ kPa | $\tau = 45$ kPa |
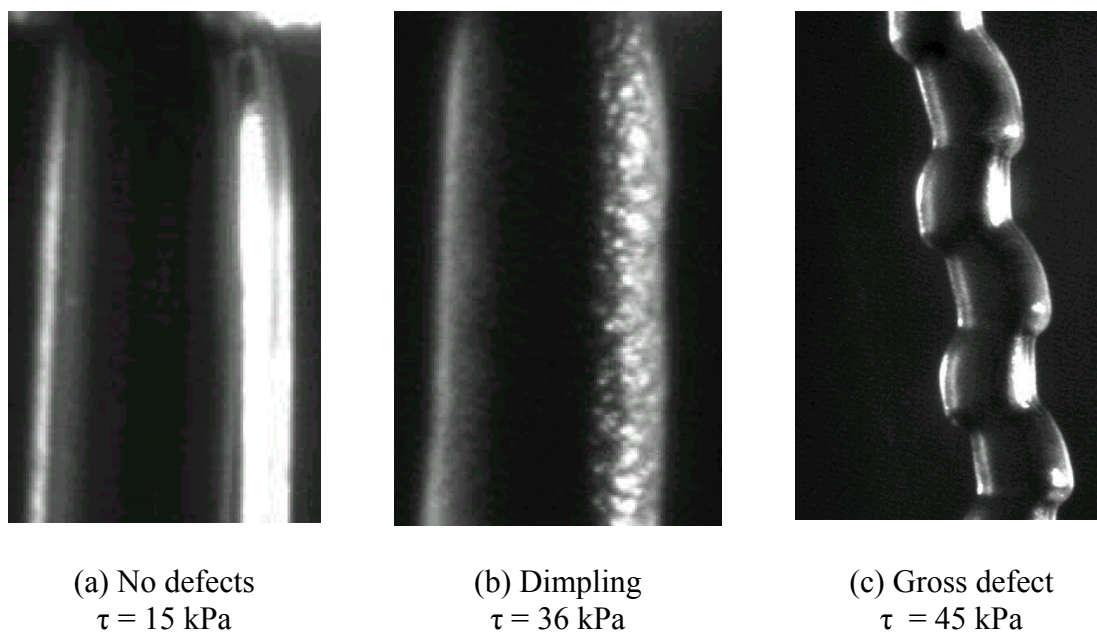
Figure 36. Extrudate defects observed for PIB+dec. The gross defect (c) was observed only from the shorter capillary, capillary 4, and not from capillary 5.

Table III. Comparison of Characteristic Times For Flow Instability Onset		
	PDMS	PIB+dec
τ_w at onset [kPa]	25 ± 3	15 ± 3
t_R (Capillary 4: Instability) [s]	0.025	0.6
t_R (Capillary 5: No Instability) [s]	0.4	9.6
λ [s]	0.07	> 4.8

short capillary at the onset of the instability is 0.6 s while the residence time in the long capillary at the same flow rate is 9.6 s. These values are all collected in Table III to allow quick comparison. For PDMS the flow instability occurs only when $t_R < \lambda$. The same is likely true for PIB+dec.

To investigate the possible role of cavitation in the onset of the flow defects, the liquids were sheared with the pressure in the exit chamber held at 15 kPa (vacuum) and 295 kPa (pressurized). No change in the onset of the gross defect, the flow instability, was seen as a result of the pressure change.

Close comparison of the extrudate from capillary 5, which exhibits the loss-of-gloss defect, suggests that pressure may affect the onset of this defect (Figure 37 and Figure 38). But the effect, which is subtle, is opposite that which would support our hypothesis. An increase in pressure appears to have had either no effect or to have reduced the shear stress necessary for the surface defect to occur. It is concluded that although extrusion defects occur at stress conditions similar to those for which the PNSCC predicts cavitation, cavitation is not necessary for these defects to occur.

τ = 24 kPa	τ = 34 kPa	τ = 37 kPa	τ = 41 kPa	τ = 46 kPa
$\dot{\gamma}$ = 230 s^{-1}	$\dot{\gamma}$ = 540 s^{-1}	$\dot{\gamma}$ = 680 s^{-1}	$\dot{\gamma}$ = 880 s^{-1}	$\dot{\gamma}$ = 1160 s^{-1}
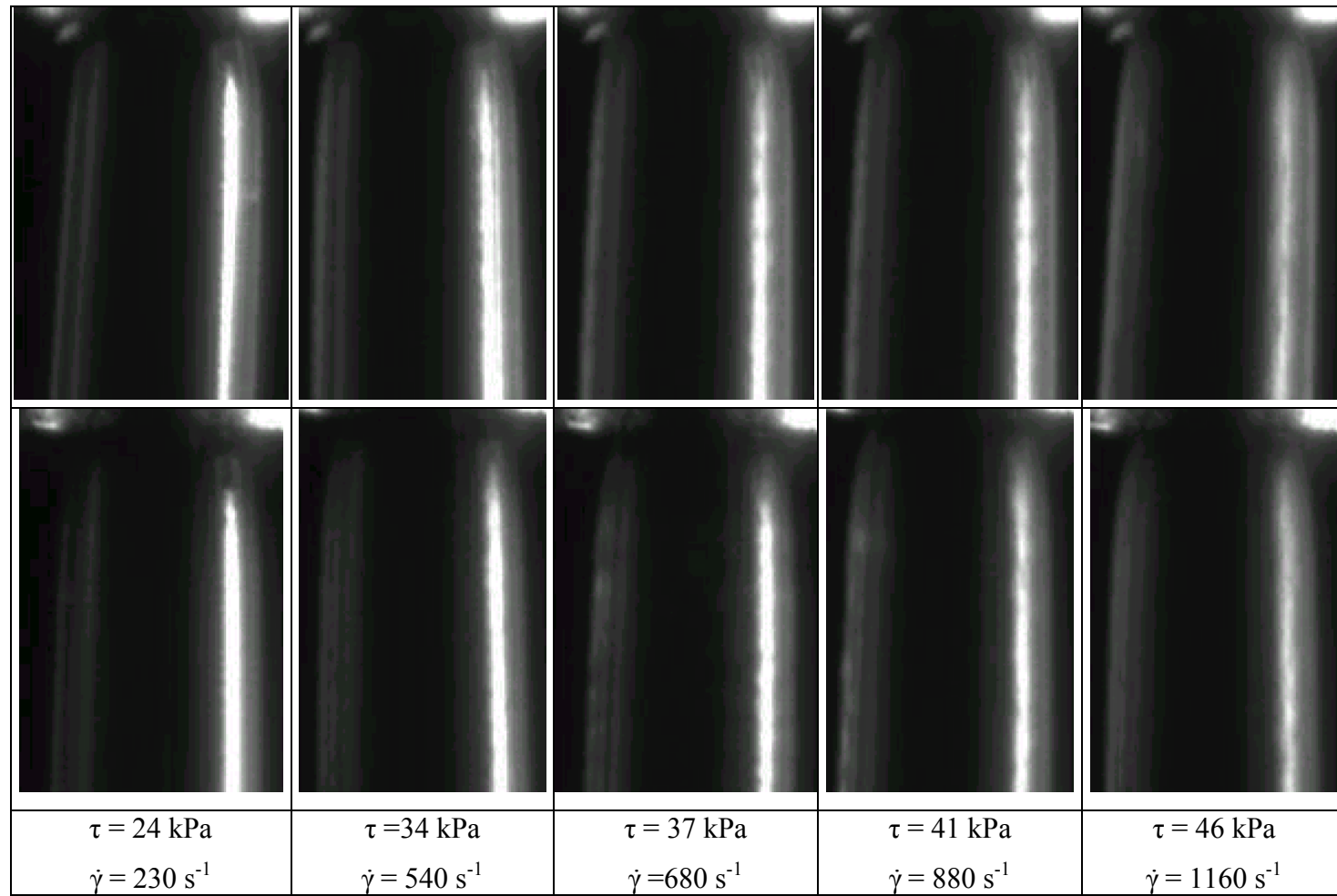
Figure 37. PDMS: top row p = 15 kPa (vacuum), bottom row p = 295 kPa (pressurized). The haziness seems to be slightly greater for a given shear stress in the pressurized extrudate than in the extrudate with vacuum. This is opposite the effect expected if cavitation plays a role in surface defect formation.

τ = 15 kPa	τ = 21 kPa	τ = 25 kPa	τ = 28 kPa	τ = 31 kPa
$\dot{\gamma}$ = 1.5 s^{-1}	$\dot{\gamma}$ = 4.1 s^{-1}	$\dot{\gamma}$ = 6.1 s^{-1}	$\dot{\gamma}$ = 8.5 s^{-1}	$\dot{\gamma}$ = 11.4 s^{-1}
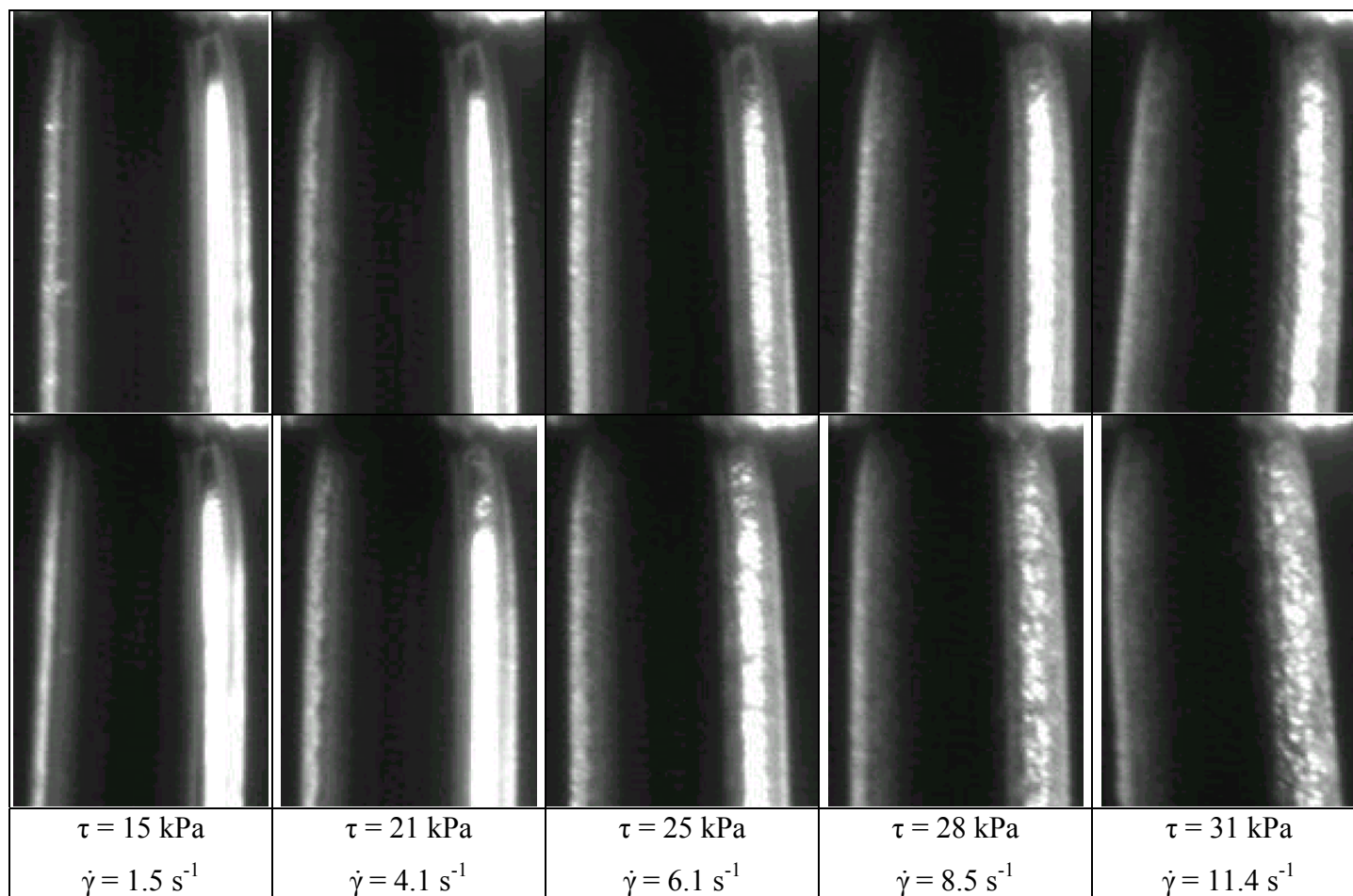
Figure 38. PIB + Decalene: top row p = 15 kPa (vacuum), bottom row p = 295 kPa (pressurized). The dimpling seems to be slightly greater for a given shear stress in the pressurized extrudate than in the extrudate with vacuum. This is opposite the effect expected if cavitation plays a role in surface defect formation.

4.3   ESTIMATING NORMAL STRESS DIFFERENCES

To compare the predictions of the PNSCC to experimental results for PDMS, normal stress differences have to be estimated, because the cavitation criterion is Eq. (1.10). Second normal stress differences, N_2, were assumed to be negligible, and first normal stress differences, N_1, were estimated.   The capillary experiment designed to investigate the role of cavitation in extrusion defects provides a means to check the model used to estimate N_1 as a function of τ, Eqs. (1.7), (2.6), (2.7) and (2.11).

Measurements of die swell provide an index of first normal stress differences (Tanner 2002).   Tanner assumed a KBKZ constitutive equation and calculated the equilibrium elastic swell of a circular jet neglecting inertia, surface tension, and thermal effects

$$B^e = \frac{D_{ex}^e}{D} = \left(1 + \frac{1}{8}\left(\frac{N_1}{\tau} \right)_w^2 \right)^{\frac{1}{6}}$$ (4.12)

The subscript w indicates values at the wall; the superscript e indicates that these values consider only the elastic effect. D_{ex} is the equilibrium extrudate diameter and D is still the capillary diameter. Stokes flow of a circular jet of Newtonian fluid swells such that

$$B^N = \frac{D_{ex}^N}{D} = 1.13$$ (4.13)

Assuming that the total swell is a combination of the Newtonian and elastic swell, the first normal stress difference at the wall can be calculated as a function of extrudate diameter, D_{ex}

$$N_{1w} = 2\tau_w \sqrt{2\left(\frac{D_{ex}}{D} - 0.13 \right)^6 - 2}$$ (4.14)

Although useful, this result has been found to produce large errors, yielding N_1 estimates two to three times measured values (Macosko 1994). Hence it must be used with caution.

The swell of PDMS extrudates from capillaries 4 and 5 was determined from video images. The resulting estimated values of N_1 are plotted against the previously used model in Figure 39. The values obtained from extrudate.swell are nearly always higher than the model, but never by more than a factor of two; based on the typical errors associated with extrudate swell estimates of normal stress differences, referred to in the previous paragraph, this constitutes good agreement.

4.4   CONCLUSIONS

The capillary tube viscometer results provide no link between the PNSCC and extrusion defects, gross or surface. Indeed, both the inability to observe extrusion defects in PB and the lack of any inhibiting effect of pressurization on defect onset are strong indications that cavitation is neither necessary nor sufficient for any of the typically observed defects. This does not mean that cavitation does not occur; it likely does, but it would be a third type of defect, an "internal defect." It appears to be purely coincidental that the stresses for the onset of surface defects, gross defects, and internal defects are typically all of the same order of magnitude.
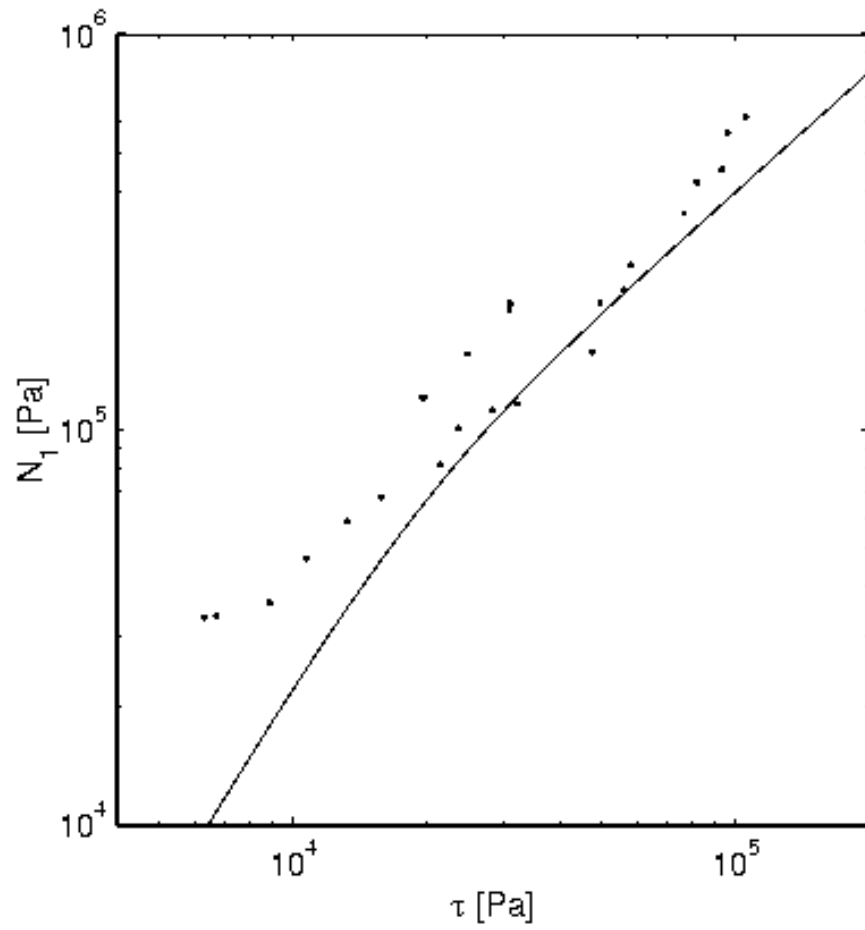
Figure 39. Plot of N_1 as a function of shear stress τ for PDMS using extrudate swell, Eq. (4.14), from capillaries 4 and 5 (dots) for validation of the previously used model, Eq. (2.11), plotted as the line.

CHAPTER 5

VISCOSITY AT NEGATIVE PRESSURE

5.1   BACKGROUND

The effect of pressure on lubricant viscosity is important in bearing analysis. The Barus equation is often used to describe variations of viscosity with pressure:

$$\mu = \mu_0 \exp(\alpha_o p) \tag{5.1}$$

The magnitude of the initial pressure viscosity coefficient α_o is usually 10 to 70 GPa^{-1} for lubricants. As a result, in general only the very high pressures generated in bearings are considered to have an important effect (Tanner 2000).   However, it is clear from examination of experimental data that the viscosity often does not obey Eq.(5.1), and the use of more accurate models or experimental data is necessary at high pressures (Bair *et al*. 2001).   Just as the Barus equation fails to adequately describe the variation of viscosity with pressure over wide pressure ranges, its accuracy at negative pressures is unknown. That bearings operate with lubricants experiencing tension has been shown experimentally for a journal bearing lubricated with mineral oil (Nakai and Okina 1976) and for a main engine bearing lubricated with engine oil (Mihara and Someya 2002). Without knowledge of the viscosity behavior at negative pressures, the accuracy of existing models and the importance of negative pressure viscosity behavior on bearing analysis cannot be assessed.

Although viscosity does not usually obey Eq. (5.1), the initial pressure viscosity coefficient α_o has been used in elastohydrodynamic (EHD) calculations (Bair 1993). Klaus and Bala argue that α_o is a key parameter in the calculation of elastohydrodynamic film thicknesses (Klaus and Bala 1993). Methods of determining α_o often apply a finite

difference approximation to $\mu(p)$ in the vicinity of zero pressure to find the slope of $\ln(\mu)$ versus p, and hence, the pressure viscosity coefficient at two pressures

$$\alpha(p) = \left(\frac{1}{\mu}\frac{\partial \mu}{\partial p}\right)\bigg|_p = \frac{\partial \ln \mu}{\partial p}\bigg|_p \tag{5.2}$$

For example, a linear variation of $\alpha(p)$ approximation would require that measurements of viscosity be made at atmospheric pressure and two different pressures, p_1 and p_2. For $p_1 < p_2$, the finite difference approximation is used to determine $\alpha(p)$ at the midpoint pressures between atmospheric pressure and p_1, and between p_1 and p_2. Then linear extrapolation is used to infer α_o. Two factors compete in determining the accuracy of this method. Larger pressure changes reduce inaccuracy due to experimental error, while smaller changes reduce inaccuracy due to the finite difference approximation and linear model. For a given pressure step size, if either p_1 or p_2 were negative, the estimation of α_o would be inherently more accurate (Bair and Qureshi 2002). Similarly, if the methods of measuring pressure and viscosity are accurate enough, then a small pressure change could be used, and the viscosity at atmospheric pressure and a slightly negative pressure could be measured. As long as $\alpha(p)$ is continuous across absolute zero pressure, it could be treated as constant in the vicinity of zero pressure and only two viscosity measurements would be needed to determine α_o.

The realization that bearings may operate with lubricants withstanding tension and the possibility of extending the pressure range over which $\alpha(p)$ can be measured make the development of a method of measuring viscosity of lubricants under tension of interest.

Two viscometers were constructed which use different methods to create tension. The first was based on the Berthelot method (Figure 40). The second uses an isothermal expansion method and is referred to as the bellows method (Figure 41). Both viscometers use the same valve/manifold assembly and sinker.

5.2   VISCOMETRY

Both viscometers are identical with respect to viscosity measurement methods. They are of the falling cylinder type, similar in construction and operation to those used by Bair to measure high pressure effects on limiting zero shear viscosity (Bair 1993). In this type of viscometer, the viscosity is proportional to the difference in densities of the sinker, ρ_{sinker}, and fluid, ρ_{fluid}, and inversely proportional to the rate of fall of the sinker. The viscometer is made of non-magnetic materials, while the sinker is made of a magnetic material. The viscometer is surrounded by a linear variable differential transformer, (LVDT), and the sinker movement produces a change in LVDT output voltage, ΔV, proportional to displacement, so that the viscosity can be measured as:

$$\mu = \frac{C\left(\rho_{sinker} - \rho_{fluid}\right)t}{\Delta V} \qquad (5.3)$$

where C is a calibration constant. For small magnitude pressure changes, the fluid can be considered incompressible.

Two different LVDTs were used. The Berthelot method apparatus uses a Schaevitz XS A-253, which has a nominal linear range of $\pm$ 12.7 mm, and a sensitivity of 30 mV/V RMS/ mm. The bellows method apparatus uses a Schaevitz HR 050, which has a nominal linear range of $\pm$ 1.27 mm, and a sensitivity of 230 mV/V RMS/ mm. This
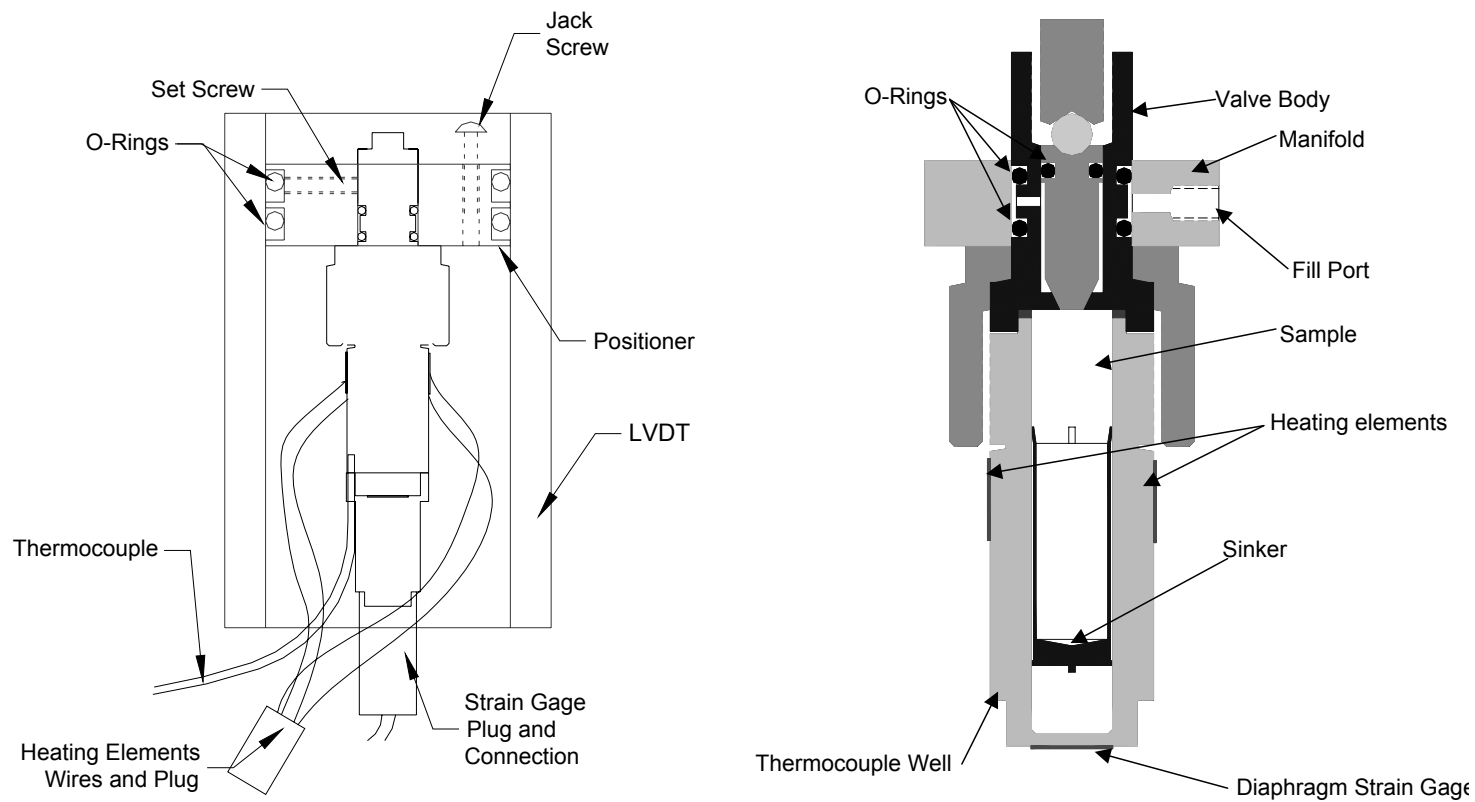
Figure 40. Falling cylinder viscometer using the Berthelot method to obtain hydrostatic tension in the test liquid.
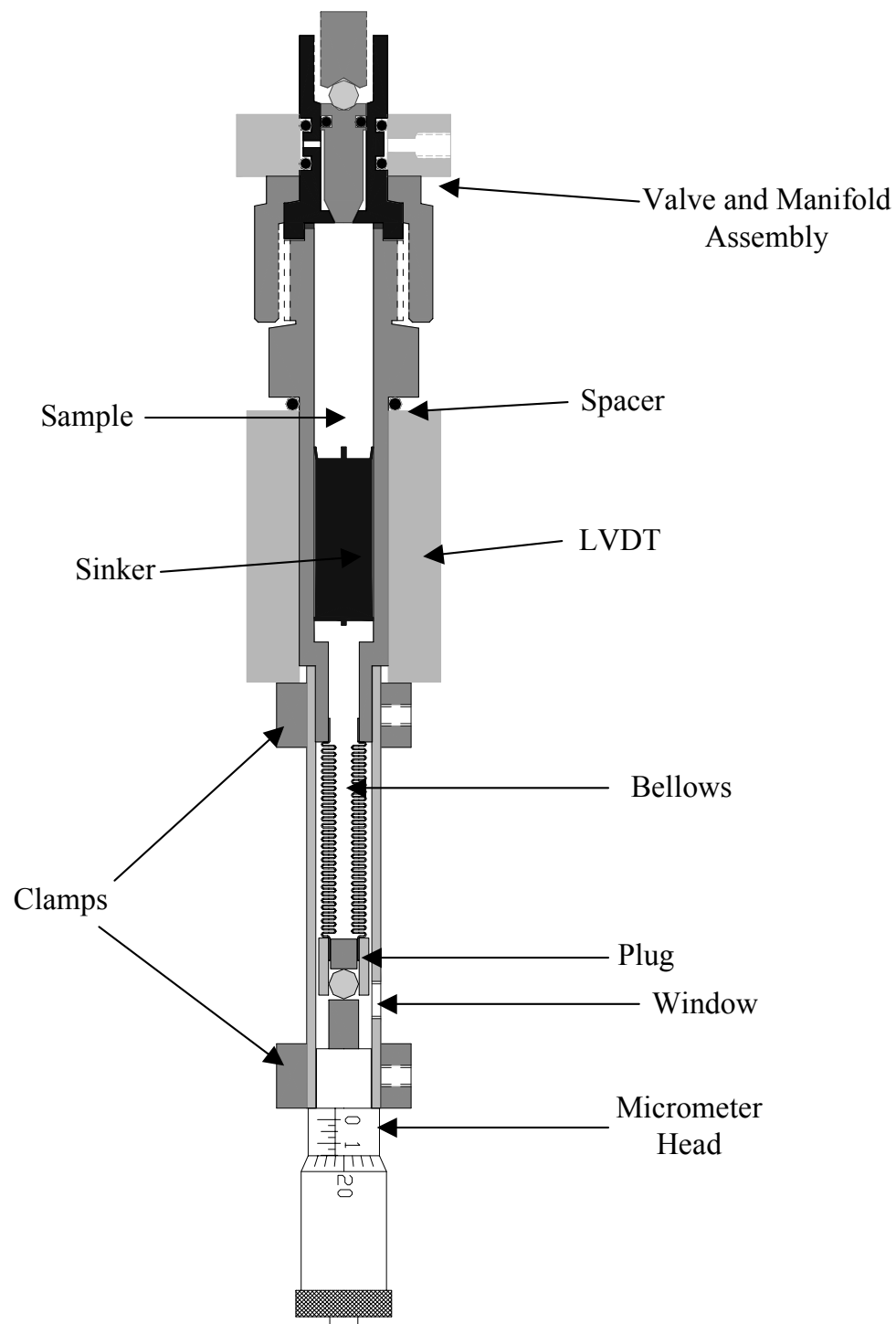
Figure 41. Falling cylinder viscometer using the bellows method to obtain hydrostatic tension in the test liquid. The valve and manifold assembly for this apparatus are identical to those used for the Berthelot method apparatus and are not shown.

smaller, more sensitive LVDT could be used with the bellows method apparatus because of the lack temperature monitoring or control, which reduced the viscometer diameter. LVDT output was recorded on an oscilloscope. Calibration was performed with a commercial viscosity standard. The sinker was repositioned by inverting the viscometer.

5.2.a Berthelot method

The viscometer cavity was filled with the liquid sample and the viscometer sinker is dropped into the cavity. Then the valve body and manifold are attached. The manifold allows undissolved gases to be removed and replaced by more liquid sample. It also allows a liquid seal to be maintained when the valve is opened, and permits connection of a vacuum pump or pressurized gas source. A thermocouple measures pressure vessel temperature. A diaphragm strain gage is calibrated to indicate pressure. The calibration was performed at positive pressure against a high accuracy Heise gage and assumed to be accurate for negative pressures. The position of the viscometer can be varied with respect to the LVDT by changing the location of an adjustable positioner that holds the viscometer within the LVDT. This allows locating the viscometer so that the sinker falls in the linear portion of LVDT output. The temperature of the viscometer is controlled by two miniature electrical resistance heaters connected to a variable power supply.

To achieve hydrostatic tension, the viscometer is filled and sealed. Then it is heated. The presence of gaseous bubbles is obvious during heating because the response of pressure to temperature rise is slow. Once all bubbles present have been collapsed, the pressure rises rapidly for small temperature increases. The rate of increase can be fairly well predicted by the ratio of thermal expansion coefficient and coefficient of compressibility for the liquid. When the heating is stopped the liquid cools. If all

133

bubbles have been eliminated, then the liquid pressure drops below zero, becoming increasingly negative until the liquid audibly fractures and the pressure instantaneously jumps to a value slightly above zero. Temperature control is not fine enough to allow the pressure drop to b stopped and a steady value of tension to be maintained.

In order to obtain repeatable and meaningful results, it is necessary to coordinate the fall of the sinker and the pressure decrease so that the sinker is falling through the linear range of the LVDT while the liquid is under tension.

5.2.b Bellows method

The valve and manifold for the bellows method apparatus are identical to those for the Berthelot method. The viscometer body has a thinner wall and fits snuggly inside a smaller LVDT than that used for the Berthelot viscometer. Spacers allow adjustment of the relative positions of the viscometer body and the LVDT to ensure the linear portion of LVDT response is used. The end of the viscometer body is bored through and silver-soldered to a phosphor bronze bellows, the free end of which is plugged.   The compression of the bellows is effected and measured by a micrometer head accurate to 25 μm. The elasticity of the bellows produces the tension in these experiments. The bellows spring constant in compression was measured with a dial indicator and force gage and was found to be 11.7 N/mm. The bellows effective area is 14.2 mm^2. Therefore, if the liquid is restraining the bellows in a compressed position, the pressure in the liquid is

$$p = p_{atm} - K\Delta L \tag{5.4}$$

where K has a value of 824 kPa/mm. The accuracy of this method of determining pressure was verified against a Heise gage by applying low positive pressures from a pressurized gas source and measuring bellows deflection.

Once the viscometer is filled and sealed, the liquid volume is compressed using the micrometer head. The possibility of bubbles present at atmospheric pressure makes calculation of the resulting positive pressure due to compression impossible, but high pressure can be verified both by the resistance to compression and the resulting higher viscosity of the test liquid. Another qualitative indication of pressure is bellows squirm. Squirm is a phenomenon similar to buckling, which occurs when a bellows with restrained ends is pressurized above a critical value. In this case the manufacturer reported that the critical squirm pressure is 3.1 MPa. Therefore, this was the maximum pressure obtainable in compression.

After compressing the liquid to eliminate bubbles, the valve is opened to restore pressure to atmospheric. Before cycling the valve, the manifold is filled with test liquid to maintain a liquid seal. The bellows compression is adjusted while the valve is open so that the magnitude of tension is unambiguously known when the bellows is released. The valve is shut, and atmospheric pressure fall time is recorded. Because there is no provision for measuring liquid temperature, all measurements must be performed in a short time span and without handling the viscometer body. This prevents temperature effects on viscosity from obscuring pressure effects, and ensures that the pressure is atmospheric prior to bellows release. The sinker is positioned for a negative pressure measurement, and allowed to begin falling. During the fall the micrometer head is released from holding the bellows in compression, resulting in hydrostatic tension in the liquid. The presence of hydrostatic tension is verified by lack of bellows movement. When the liquid fails, the bellows expands. One drawback of this method of achieving

tension is the requirement to open the valve and replace a small amount of test liquid between measurements.

5.2.c Experimental liquids

Tension effects on viscosity were measured for a branched perfluorinated polyether (143AZ) and for a cyclic phosphazene lubricant (X1P). The temperature and positive pressure viscosity behavior of 143AZ was characterized to relatively high pressures in this lab using previously described methods and fitted to the Yasutomi model (Yasutomi *et al*. 1984).

Tension was also achieved in several silicone oils (two grades of PDMS supplied by Dow Corning, and octamethyl trisiloxane), squalane supplied by Sigma Aldrich, a mineral oil (Canon viscosity standard HT150), tap water, and acetone supplied by Fisher Scientific. Manufacturer supplied properties of the143AZ, X1P, silicone oils, and squalane are given in Table IV.

Table IV. Liquid Properties for Tension Viscometry Experiments		
	ρ [kg/m^3]	ν [mm^2/s]
143AZ (20 °C)	1860	137
X1P (20 °C)	1480	1826
PDMS1 (25 °C)	957	100
PDMS2 (25 °C)	957	1000
Squalane (20 °C)	810	Not Provided
Mineral Oil (100 °C)	795	4.65

5.3   RESULTS AND DISCUSSION

The effect of hydrostatic tension (negative pressure) on the viscosity of 143AZ and X1P was measured in the bellows apparatus. All measurements are performed at room temperature, 20°C. For each measurement, four fall times were recorded at atmospheric pressure producing an average value, and then the negative pressure fall time was recorded. The calculation of α_o was performed by taking the natural logarithm of Eq. (5.2) differentiating with respect to pressure and applying a two point finite difference approximation.

Results from negative pressure measurement were compared to positive pressure results using Bair's previously described viscometer (Bair *et al*. 2001). For 143AZ these results were fitted to the Yasutomi free volume model, which describes the pressure and temperature viscosity behavior of liquids (Yasutomi *et al*. 1984):

$$\mu = \mu_g \exp\left[\frac{-2.3 C_1 \left(T - T_g\right) F}{C_2 + \left(T - T_g\right) F}\right]$$ (5.5)

$$T_g = T_{g_O} + A_1 \ln\left(1 + A_2 p\right)$$ (5.6)

$$F = 1 - B_1 \ln\left(1 + B_2 p\right)$$ (5.7)

The Yasutomi parameters for 143AZ, obtained by nonliear regression of viscosity data, are provided in Table V.

Table V. Yasutomi Parameters for 143AZ			
$\underline{\mu_g}$[Pa s]	$\underline{T_{go}}$[°C]	$\underline{A_1}$[°C]	$\underline{A_2}$[Pa^{-1}]
10^{12}	-145.4	220.0	1.987
$\underline{B_1}$	$\underline{B_2}$[Pa^{-1}]	$\underline{C_1}$	$\underline{C_2}$[°C]
0.1591	21.014	16.829	46.272

For 143AZ, seven measurements were taken at a hydrostatic tension of 620 kPa. The resulting measured change in viscosity due to a change in pressure from atmospheric pressure to an absolute pressure of –620 kPa was –1.7%±1.2%. The resulting value for α_o is 24±15 GPa^{-1}. The Yasutomi model predicts a change in viscosity of –2.8%. The measurements used to fit the Yasutomi model were used to obtain α_o by applying the model of linear variation of $\alpha(p)$ and extrapolating. The pressures used were atmospheric, 5 MPa and 10 MPa. The resulting value was 36±12 GPa^{-1}.

For X1P a total of seven measurements were taken at tensions of 550, 620, and 770 kPa. The resulting value of α_o is 64±30 GPa^{-1}. A calculation using measurements made with the high pressure viscometer at atmospheric pressure and 5 MPa yields a value for α_o of 46±14 GPa^{-1}.

The uncertainties in the changes in viscosity and values of α_o are significant and a result of several factors described in the next section.

The high pressure measurements are taken at a minimum pressure interval of 5 MPa based on the accuracy of the pressure transducer. Because this interval is almost 10 times that between atmospheric and negative pressure measurements, there is no advantage gained by using a model of linear variation of $\alpha(p)$ and data obtained above and below zero pressure.

The key element to obtaining a relatively large tension appeared to be removal of all gas bubbles. Several methods were devised for this, and the combination of all of them produced the best results. After filling the vessel, the liquid was degassed by applying a vacuum and heat simultaneously. The liquid was then held at an elevated

pressure to force remaining bubbles into solution. In the Berthelot method apparatus the elevated pressure was achieved by heating with the vessel sealed. The pressure was allowed to peak between 5.5 and 6.9 MPa. In the bellows apparatus the elevated pressure was achieved through compression of the bellows, limiting it to 3.1 MPa. However, this pressure was held for longer periods of time (12-48 hours). Tension was consistently obtained for samples of kinematic viscosity at room temperature of the order of 10 mm^2/s or less by following one or more degassing periods of 30 minutes at 50°C and 15 kPa absolute pressure with pressurization.

In the bellows viscometer, X1P and 143AZ were able to withstand tensions of greater than 500 kPa for periods of time exceeding one minute. For this range of tensions, the failure of the liquid usually did not occur until there was some mechanical agitation such as the sinker reaching the bottom of the viscometric tube. However, no matter how stable the tensile state appeared at values up to 770 kPa, tensions greater than this were never maintained in the bellows viscometer for more than a fraction of a second.

Tension was achieved in the Berthelot viscometer for eight different liquids. The maximum value achieved for each liquid is given in Table VI. These tensions were

Table VI. Maximum tension observed before liquid failure, Bethelot method [kPa]			
143 AZ	Octamethyl Trisiloxane	PDMS1 ($v = 100$ mm^2/s)	PDMS2 ($v = 1000$ mm^2/s)
1720	2065	1585	290
Squalane	Mineral Oil	Acetone	Tap Water
2165	2340	1685	1030

Table VII. Comparison of tensions achieved by various methods in mineral oil [kPa]	
Method	Maximum reported tension [kPa]
Berthelot Method (present work)	2340
Expansion with Bellows (Nakai and Okino 1976)	431
Expansion with Bellows (Nakai 1987)	578
Expansion with Piston (Washio *et al*. 2001)	210
Journal Bearing (Nakai and Okino 1976)	70

achieved during temperature transients, and therefore not held for any length of time.

The variation of the apparent tensile strength with experimental method is emphasized in Table VII by comparing values obtained for mineral oil via the Berthelot method, bellows expansion (Nakai and Okino 1976; Nakai 1987), and piston expansion (Washio *et al*. 2001), as well as in a journal bearing (Nakai and Okino 1976). In general it appears that the failure of the liquid to withstand tension does not occur when the tension reaches the theoretical tensile strength but at some lower value that depends also upon the method in which the tension is applied.

Greater values of tension were obtainable via the Berthelot method than the bellows method. Thus greater effects on viscosity would be expected to be apparent. However, viscosity measurements from the Berthelot viscometer were not repeatable. The lack of repeatability is believed to be due to the reliance on temperature to affect pressure. The location and precision of the thermocouple result in inaccuracies in temperature measurements that have a greater effect on viscosity than the pressure

variations. The inability to maintain a steady temperature while the liquid was under tension exacerbated this problem.

It was found that tension is more easily obtained in lower viscosity samples for lubricants. This is consistent with the findings of Nakai and Okino (Nakai and Okino 1976; Nakai 1987).

In the bellows viscometer, larger tensions were generated in X1P than 143AZ, despite X1P's higher viscosity. X1P has a high sensitivity of viscosity to temperature, and was heated prior to deaeration, so the deaeration was performed at low viscosity. It was tentatively concluded that the limiting factor in achieving tension was often the presence of gas bubbles in crevices, which could provide a nucleation site for fracture.

5.4   UNCERTAINTY OF RESULTS

The uncertainties of viscosity changes and α_o reported in the results and discussion appear rather large. In fact, an honest appraisal of many values of α_o available in the literature would reveal that this parameter is not generally accurately known. In this section the methods used in this work to arrive at the reported uncertainties are detailed. In addition, an example of the misleading nature of many apparently less uncertain initial pressure viscosity coefficients is provided.

In the case of the change of viscosity and the initial pressure viscosity coefficient measured using the bellows method apparatus, the uncertainty is statistical. For each measurement, values of fall time and LVDT output voltage change at positive and negative pressure are recorded. It is assumed that during the short time of the measurement (about 30 seconds) the temperature of the liquid did not change and therefore the difference in rates of voltage change, and thus viscosity, is entirely due to

141

the difference in pressure. The percent change in the viscosity is the percent change of the rate of voltage change. The magnitude of viscosity change due to pressure is of the same order as the change due to variations in ambient temperature over longer periods of time. Therefore this percent change is reported, rather than the viscosity values determined from the fall times. The rates of voltage change and the known imposed pressure change also allow calculation of α_o from each measurement. The uncertainty, δ, reported for the percent viscosity changes and values of α_o is

$$\delta = \frac{SSD}{\sqrt{N}}$$ (5.8)

where SSD is the sample standard deviation and N is the number of samples (seven in both cases).

In the case of the uncertainty reported for α_o determined from positive pressure measurements, the uncertainty is a result of estimation of uncertainties in measurement of viscosity and pressure. There is an additional uncertainty involved in the extrapolation of this data to zero pressure, but because of the already conservative nature of the estimation of uncertainty, the extrapolation uncertainty is not also included. The viscometer used for the positive pressure measurements has an estimated maximum inaccuracy of 2%. The pressure transducer used for the positive pressure measurement is used for measurements of pressures up to 900 MPa, and has an accuracy of ± 1 MPa. The small pressure step size used, 5 MPa, combined with the inaccuracy of the pressure transducer, leads to the large uncertainty reported for α_o calculated from positive pressure measurements of viscosity.   In general, more accurate determination of α_o using a high-pressure viscometer would not justify the expense of a pressure transducer with greater accuracy at relatively low pressures.

In the literature there a large number of models used to describe the variation of viscosity with pressure. In general, tribologists investigating pressure effects on viscosity have chosen one of these models and used regression to fit the model to viscosity data at different pressures, obtaining a function, $\mu_m(p)$, that is meant to describe the variation of viscosity with pressure. Values of α_o thus obtained are

$$\alpha_0 = \frac{1}{\mu_m(p=0)} \frac{\partial \mu_m}{\partial p}\bigg|_{p=0} \tag{5.9}$$

and are given to apparently high accuracy. For instance, Sharma *et al* performed measurements of viscosity of one of the liquids investigated in this report, Krytox 143AZ, and fitted Roelands equation,

$$\mu_m = \mu_o \left(\frac{\mu_\infty}{\mu_o}\right)^{\left[1-\left(1+\frac{p}{c_p}\right)^Z\right]} \tag{5.10}$$

to the data (Sharma *et al*. 1995). Their results, obtained at five different temperatures, and at pressures up to 850 MPa, are reproduced as the insert in Figure 42. Applying Eq. (5.9) to Eq. (5.10) yields the expression for the initial pressure viscosity coefficient these results would suggest,

$$\alpha_0 = \frac{Z}{c_p} \ln\left(\frac{\mu_o}{\mu_\infty}\right) \tag{5.11}$$

which is called the "pressure viscosity coefficient" in their work, and reported to five significant digits with no uncertainty reported. Figure 42 shows the lower pressure data with fitted curves for the three highest temperatures so that the inaccuracy in determining α_o in this manner is obvious. The data were obtained by picking them off a reproduction of the same data on a larger scale (Gupta 1995). Values of α_o obtained using the first
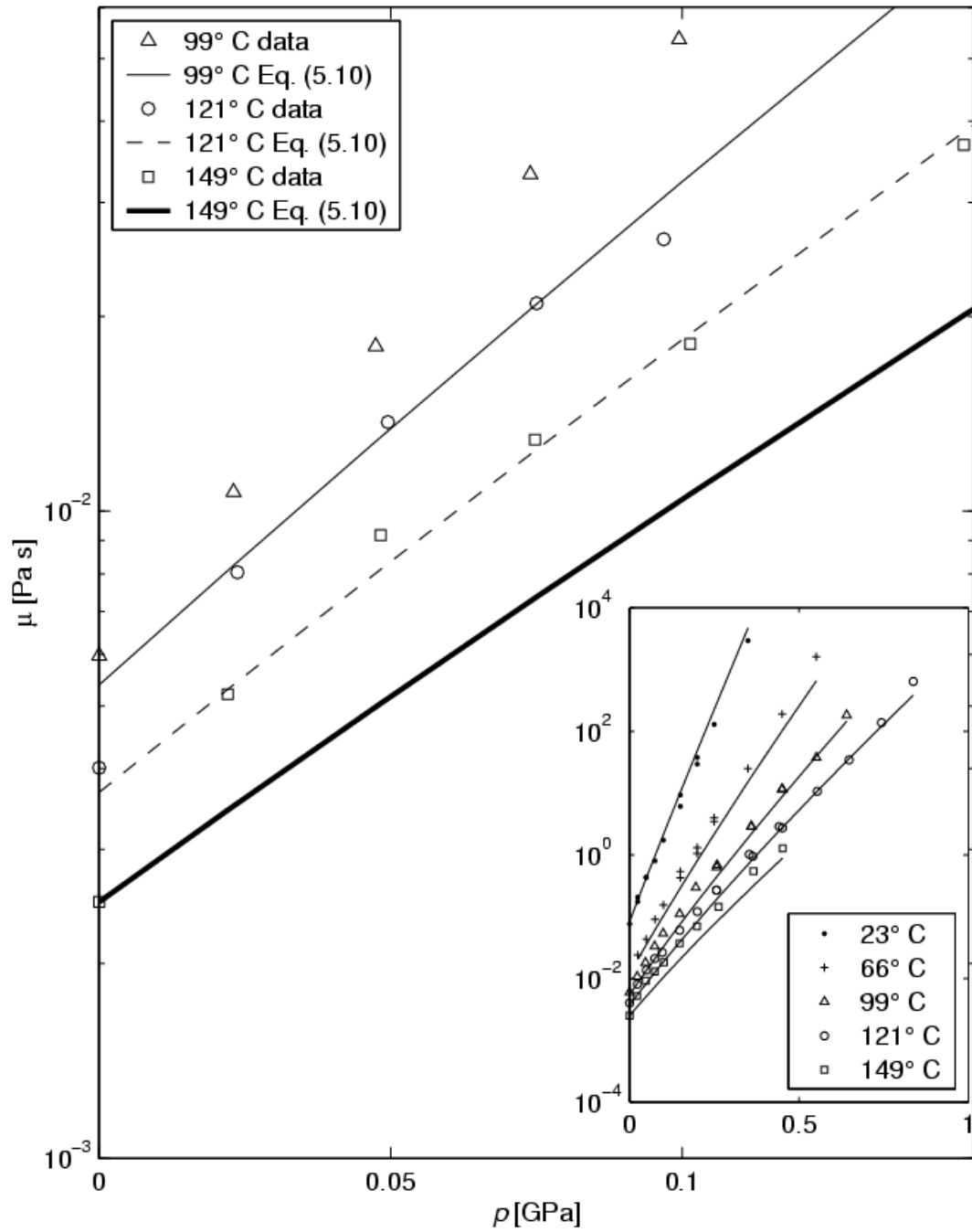
Figure 42. Pressure viscosity data for 143AZ fitted to Eq. (5.10) from (Sharma *et al*. 1995). The lower pressure data with fitted curves are reproduced for the three highest temperatures to demonstrate the unsuitability of using such curve fits to obtain α_0.

144

	Table VIII. Comparison of α_o	
	α_o [GPa^{-1}]	α_o [GPa^{-1}]
T [°C]	Finite Difference and Linear Extrapolation	Curve fit, Eq. (5.11) (Gupta 1995)
98.9	27	18.941
121.1	33	17.225
148.9	39	16.139

three data points for each of these temperatures and the finite difference and linear extrapolation method described in section 5.1 are compared with the values of α_o suggested by Sharma *et al*. in Table VIII. Although the values obtained through the method recommended here match the viscosity data better than those obtained using the curve fit of Sharma *et al*., they are still subject to uncertainty due to instrument accuracy and extrapolation uncertainty.

5.5   CONCLUSIONS

The agreement between α_o as calculated using viscosity obtained at pressures greater than and less than absolute zero demonstrates continuity in the magnitude of $\alpha(p)$ for these lubricants from a state of hydrostatic compression to hydrostatic tension. Therefore, for liquids that behave similarly to the lubricants studied, effects of tension on viscosity are not dramatic. These liquids were picked for their high sensitivity of viscosity to pressure. It would not be expected that other liquids would display more extreme behavior.

The agreement also demonstrates the validity of the use of viscosity data from pressures at and above atmospheric to determine α_0. For the magnitudes of tension

attainable in these experiments, the use of α_o determined by positive pressure measurements will describe the viscosity behavior as well as results determined experimentally at negative pressures. This is due to the experimental inaccuracies that dominate the effect for pressure changes of the magnitude achievable in the realm of hydrostatic tension. To successfully use negative pressures to more accurately determine α_o, a method of attaining much greater tension during the viscosity measurement would be needed.

The magnitudes of hydrostatic tension attainable tend to be relatively small, and are transient. Therefore in most applications, tensile effects can be ignored. If they are to be taken into account, models such as the Barus equation and the Yasutomi model describe negative pressure viscosity behavior adequately using data from positive pressure measurements. Because the magnitude of tension achieved depends considerably upon the method of generation, it cannot be said with certainty that situations with greater tension than seen in this study do not occur, but it seems unlikely.

The measures necessary to achieve tension for viscosity measurement have implications for the portions of this work pertaining to cavitation. Pressurization was essential prior to successfully sustaining a negative pressure in the liquid. This supports the idea that the failure to sustain tension in these polymer melts occurs due to the growth of preexisting nuclei.

CHAPTER 6

CONCLUDING REMARKS

In this work aspects of the role of tension in simple shear flows that are frequently used to measure rheological properties have been considered. The interest is in the possibility that such flows could lead to cavitation when the shear stress is sufficiently large (of the order of the pressure). There is very little prior research into this idea. The problem is considered from two different viewpoints.

The first method of investigation is an experimental test of a principal normal stress cavitation criterion. The PNSCC is attractive because of its simplicity, its appeal to physical intuition, and the large number of cases in the literature of some sort of apparent strong rheological change at shear stresses near atmospheric pressure in magnitude. The experiments constitute the first direct test of the PNSCC, and the PNSCC accurately predicts cavitation in a Newtonian liquid (PB). However, its performance is a little less satisfactory for the non-Newtonian test liquid (PDMS). Finally, it is difficult to reconcile the idea of failure of a liquid in shear with no apparent tensile strength to the fact that liquids exhibit an ability to withstand large tensions in the absence of cavitation nucleation sites. And if the presence of such nucleation sites is assumed, then the PNSCC seems overly simplistic.

Consequently, the second method of investigation is an analysis, for the case of a Newtonian liquid, of cavitation inception in shear from wall stabilized gas nuclei. The goal is to determine if the proposed continuum model of gaseous cavitation from preexisting, crevice-stabilized, wall nuclei is consistent with the experimental observations. Three stages of inception were considered, with original contributions in

each. These include an analysis of wall stabilized nucleus dissolution, boundary element method simulations of crevice stabilized, inviscid, compressible bubble deformation in a bounded shear flow with mass transfer, and an analysis of the deformation and dissolution or growth of an inviscid compressible bubble deformation in infinite shear with mass transfer. The simulations of bubble deformations in shear flow use a two dimensional model. This was suggested by experimental observations. The dissolution analysis confirms that long scratch like crevices are most likely to persist as nuclei capable of serving as cavitation inception sites. In fact, the analysis of the behavior of such nucleation sites proved to be very consistent with the results observed in the experiments with the Newtonian liquid, PB.

Much research has been done in the area of extrusion defects. The onset of such defects at shear stresses near atmospheric lead us to hypothesize a role of for cavitation in formation of extrusion defects, especially those classified as surface defects. An experiment to investigate this idea, however, argues strongly against any role for cavitation in defect formation. Firstly, although cavitation was observed experimentally for the Newtonian liquid, PB, extrusion defects were not. Cavitation therefore does not seem to be sufficient for extrusion defect formation. Secondly, in non-Newtonian liquids for which extrusion defects were observed, raising the ambient pressure did not inhibit their formation at all. The conclusion is that cavitation does not seem to be necessary for extrusion defect formation.

The final original contribution of this work is the first reported measurement of viscosity at absolute pressures below zero.

The work on cavitation inception in shear leaves open many further areas of inquiry. These include, but are not limited to, the following. Having gained insight into expected behavior of the critical shear stress for cavitation inception based on simulations, a return to experimental work to see if the model predictions are correct is needed before alternate theories of cavitation in shear are abandoned. Similarly, more involved simulations could be used to validate some of the assumptions used in this work, in particular the two dimensional model and the penetration model. Such simulations would, however, be computationally expensive.

Frequently when shear stresses are of the magnitudes considered here, they are due to rates of deformation that lead to non-Newtonian constitutive behavior for many liquids. Modeling shear cavitation inception for non-Newtonian liquids is a topic that would prove very interesting, though challenging.

Finally, satisfied that a clear picture of cavitation in shear is emerging, the understanding of this phenomenon should be applied to enhance or inhibit cavitation as desired. Liquid treatment (degassing or pre-pressurizing), surface coating, the use of surfactants, and surface etching and polishing could all be used to alter the cavitation behavior.

REFERENCES

Ait-Kadi, A., Choplin, L. and Carreau, P.J., 1989, "On Correlations of Primary Normal Stresses in Polymer Solutions", Polymer Engineering and Science, 29 (18), pp 1265-1272.

Albalak, R. J. ed., 1996, *Polymer Devolatilization*, Marcel Dekker, Inc.

Apfel, R.E., 1970, "The Role of Impurities in Cavitation-Threshold Determination," Journal of the Acoustics Society of America, 48, pp. 1179-1186.

Archer, L.A., Ternet, D. and Larson, R.G., 1997, "'Fracture' phenomena in shearing flow of viscous liquids," Rheologica Acta, 36, pp. 579-584.

Atchley, A.A. and Prosperetti, A, 1989, "The crevice model of bubble nucleation," Journal of the Acoustical Society of America, 86, pp. 1065-1084.

Bair, S. and Winer, W., 1987, "Influence of Ambient Pressure on the Apparent Shear Thinning of Liquid Lubricants – An Overlooked Phenomena," Institution of Mechanical Engineers Conference Publications 1987-5, 1, pp. 395-398.

Bair, S. and Winer, W., 1992, "The High Pressure High Shear Stress Rheology of Liquid Lubricant," Journal of Tribology, 114, pp. 1-9.

Bair, S., 1993, "An Experimental Verification of the Significance of the Reciprocal Isoviscous Pressure," STLE Tribology Transactions, 36, pp. 153-160.

Bair, S., Jarzynski, J. and Winer, W., 2001, "The Temperature, Pressure and Time Dependence of Lubricant Viscosity," Tribology International, 34, pp. 461-468.

Bair, S. and Qureshi, F., 2002, "Accurate Measurements of Pressure-Viscosity Behavior in Lubricants," STLE Tribology Transactions, 45 (3), pp. 390-396.

Barry, A.J., 1946, "Viscometric investigation of Dimethylsiloxane Polymers," Journal of Applied Physics, 17, pp. 1020-1024.

Bejan, A., 1993, *Heat Transfer*, John Wiley and Sons.

Bird, R.B., Armstrong, R.C. and Hassager, O., 1987, *Dynamics of Polymeric Liquids Volume 1 Fluid Mechanics, 2nd Ed.*, John Wiley and Sons.

Bird, R.B., Stewart, W.E. and Lightfoot, E.N., 2002, *Transport Phenomena, 2nd Ed.*, John Wiley and Sons.

Blake, T.D. and Haynes, J.M., 1977, "Kinetics of Liquid/ Liquid Displacement," Journal of Colloid and Interface Science, 30, pp. 421-423.

Blander, M., 1979, "Bubble nucleation in liquids," Advances in Colloid and Interface Science, 10, pp. 1-32.

Carslaw, H.S. and Jaeger, J.C., 1959, *The Conduction of Heat in Solids*, Clarendon Press.

Cogswell, F.N., 1973, "The influence of pressure on the viscosity of polymer melts," Plastics and Polymers, 14, pp. 39-43.

Cox, R.G., 1986, "The dynamics of the spreading of liquids on a solid surface. Part 1. Viscous flow," Journal of Fluid Mechanics, 168, pp. 169-194.

Crowdy, D.G., 2003, "Compressible bubbles in Stokes flow," Journal of Fluid Mechanics, 476, pp. 345-356.

Crowdy, D.G., 2004, Personal correspondence.

Crum, L.A., 1982, "Nucleation and stabilization of mirobubbles in liquids," Applied Scientific Research, 38, pp. 101-115.

de Bruijn, R.A., 1993, "Tipstreaming of drops in simple shear flow," Chemical Engineering Science, 48, pp. 277-284.

de Genes, P.G., 1985, "Wetting: statics and dynamics," Reviews of Modern Physics, 57 (3) Part I, pp. 827-863.

de Kee, D. and Stastna, J., 1986, "Primary Normal Stress Coefficient Predictions," Journal of Rheology, 30 (1), pp 207-230.

Denn, M.M., 2001, "Extrusion Instabilities and Wall Slip," Annual Review of Fluid Mechanics, 33, pp. 265-287.

Dimitrakopoulos, P. and Higdon, J.J.L., 1997, "Displacement of fluid droplets from solid surfaces in low-Reynolds-number shear flows," Journal of Fluid Mechanics, 336, pp. 351-378.

Duda, J.L. and Vrentas, J.S., 1969, "Perturbation Solutions of diffusion-controlled moving boundary value problems," Chemical Engineering Science, 24, pp. 461-470.

Epstein, P.S. and Plesset, M.S., 1950, "On the stability of Gas Bubbles in Liquid-Gas solutions," The Journal of Chemical Physics, 18, pp. 1505-1509.

Fan, T.H., 2003, "Fluid Membranes and Bio-Transport Phenomena in Imaging of Biological Membranes Using AFM-Integrated Microelectrode," Ph. D. Dissertation, Georgia Institute of Technology.

Favelukis, M., Tadmor, Z. and Semiat, R., 1999, "Bubble growth in a viscous liquid in simple shear," AIChE Journal, 45 (5), pp. 691-695.

Favelukis, M., Tadmor, Z. and Yeshayahu, T., 1995, "Bubble Dissolution in Viscous Liquids in Simple Shear Flow," AIChE Journal, 41 (12), pp. 2637-2641.

Feng J. and Basaran, O., 1994, "Shear flow over a translationally symmetric cylindrical bubble pinned over a slot in a plane wall," Journal of Fluid Mechanics, 275, pp. 351-378.

Gleiβle, W., 1982, "Stresses in polymer melts at the beginning of flow instabilities (melt fracture) in cylindrical capillaries," Rheologica Acta, 21, pp. 484-487.

Gruntfest, I.J., 1965, "Apparent Departures from Newtonian Behavior in Liquids Caused by Viscous Heating," Transactions of the Society of Rheology, 9 (1), pp. 425-441.

Harvey, E., Barnes, K., McElroy, W., Whitely, A., Pease, D. and Cooper K., 1944, "Bubble Formation in Animals, I. Physical Factors," Journal of Cellular and Comparative Physiology, 25, pp. 1-22.

Hirose, T., Kamiya, Y. and Mizoguchi, K., 1989, "Gas Transport in Poly-[bis(trifluuoroethhoxy)phosphazene]," Journal of Applied Polymer Science, 38, pp. 809-820.

Hoffman, R.L., 1975, "A Study of the Advancing Interface I. Interface Shape in Liquid-Gas Systems," Journal of Colloid and Interface Science, 50, pp. 228-241.

Huh, C. and Scriven, L.E. 1971, "Hydrodynamic Model of Steady Movement of a Solid/ Liquid/ Fluid Contact Line," Journal of Colloid and Interface Science, 35, pp. 85-101.

Jiang, T., Oh, S. and Slattery, J.C. 1979, "Correlation for dynamic contact angle," Journal of Colloid and Interface Science, 69, pp. 74-77.

Joseph, D.D., 1998, "Cavitation and the State of Stress in a flowing liquid," Journal of Fluid Mechanics, 366, pp. 367-378

Kell, G., 1983, "Early Observations of Negative Pressures in Liquids," American Journal of Physics, 51, pp. 1038-1041.

Klaus, E. and Bala, V., 1993, Discussion on "An Experimental Verification of the Significance of the Reciprocal Isoviscous Pressure," STLE Tribology Transactions, 36, pp. 160-161.

Kontopoulou, M. and Vlachopoulos, J. 2001, "Bubble Dissolution in Molten Polymers and its Role in Rotational Molding," Polymer Engineering and Science, 39(7), pp. 1189-1198.

Kottke, P.A., Bair, S. and Winer, W.O, 2003, "The Measurement of Viscosity of Liquids under Tension," Journal of Tribology, 125, pp. 260-266.

Kropinski, M.C.A., 2001, "An Efficient Numerical Method for Studying Interfacial Motion in Two-Dimensional Creeping Flows," Journal of Computational Physics, 171, pp. 479-508.

Larson, R.G., 1992, "Instabilities in viscoelastic flows," Rheologica Acta, 31, pp. 21-263.

Leal, L.G., 1980, "Particle motions in a viscous fluid," Annual Review of Fluid Mechanics, 12, pp. 435-476.

Longuet-Higgins, M.S. and Cokelet, E.D., 1976,"The deformation of steep surface waves on water. I. A numerical method of computation," Proceedings of the Royal Society of London. Series A, Mathematical and Physical Sciences, 350, pp. 1-26.

Macosko, C.W., 1994, *Rheology: Principles, Measurements and Applications*, VCH.

Magnaudet, J., Takagi, S. and Legendre, D, 2002, "Drag, deformation and lateral migration of a buoyant drop moving near a wall," Journal of Fluid Mechanics, 476, pp. 115-157.

Mihara, Y. and Someya, T., 2002, "Measurement of Oil-Film Pressure in Engine Bearings Using a Thin-Film Sensor," Lubrication Engineering, 58 (5), pp. 10-19.

Mørch, K.A., 2000, "Cavitation nuclei and bubble formation – a dynamic liquid-solid interface problem," Journal of Fluids Engineering, 122, pp. 494-498.

Nakai, M. and Okino, M., 1976, "Tensile Stress in Journal Bearings," Wear, 39, pp. 151-159.

Nakai, M., 1987, "A Study of Hysteresis on Attitude-Eccentricity Loci in Journal Bearings," Journal of Tribology, 109, pp. 684-690.

Novak, J.D., 1968, "An Experimental Investigation of the Combined Effects of Pressure, Temperature, and Shear Stress upon Viscosity," Ph. D. Dissertation, University of Michigan.

Pereira, A., McGrath, G. and Joseph, D.D., 2001, "Flow and Stress Induced Cavitation in a Journal Bearing with Axial Throughput," Journal of Tribology, 123, pp. 742-754.

Plesset, M. and Prosperetti, A., 1977, "Bubble dynamics and cavitation," Annual Review of Fluid Mechanics, 9, pp. 145-185.

Power, H., and Wrobel, L.C., 1995, Boundary Integral Methods in Fluid Mechanics, Computational Mechanics Publications.

Pozrikidis, C., 2001, "Interfacial Dynamics for Stokes Flow," Journal of Computational Physics, 169, pp. 250-301.

Pozrikidis, C., 2001, "Expansion of a compressible gas bubble in Stokes flow," Journal of Fluid Mechanics, 442, pp. 171-189.

Pozrikidis, C., 2002, *A Practical Guide to Boundary Element Methods*, Chapman and Hall/ CRC.

Pozrikidis, C., 2003, "Computation of the pressure inside bubbles and pores in Stokes flow," Journal of Fluid Mechanics, 474, pp. 319-337.

Prausnitz, J. M., Rüdiger, L. N. and de Azevedo, E. G., 1999, *Molecular Thermodynamics of Fluid-Phase Equilibria, 3rd Ed.*, Prentice Hall PTR.

Rallison, J.M., 1984, "The deformation of small viscous drops and bubbles in shear flows," Annual Review of Fluid Mechanics, 16, pp. 45-66.

Richardson, S., 1968, "Two dimensional bubble in slow viscous flow," Journal of Fluid Mechanics, 33, pp. 476-493.

Schleizer, A. and Bonnecaze, R., 1999, "Displacement of a two-dimensional immiscible droplet adhering to a wall in shear and pressure-driven flows," Journal of Fluid Mechanics, 383, pp. 29-54.

Sharma, S., Hoglund, E. and Hamrock, B., 1995, "Rheology of Perfluorpolyalkylether Fluids in Elastohydrodynamic Lubrication," STLE Tribology Transaction, 38(4), pp. 769-780.

Shelley, M.J., 1992, "A study of singularity formation in vortex-sheet motion by a spectrally accurate vortex method," Journal of Fluid Mechanics, 244, pp. 493-526.

Smart, J.R. and Leighton, D.T., 1991, "Measurement of the drift of a droplet due to the presence of a plane," Physics of Fluids A, 91(3), pp. 21-28.

Smith, M. K., 1995, 'Thermocapillary migration of a two-dimensional liquid droplet on a solid surface," Journal of Fluid Mechanics, 294, pp. 209-230.

Son, Y. and Migler, K.B., 2002, "Cavitation of Polyethylene during Extrusion Processing Instabilities," Journal of Polymer Science: Part B: Polymer Physic, 40, pp. 2791-2799.

Strasberg, M., 1959, "Onset of Ultrasonic Cavitation in Tap Water," Journal of the Acoustical Society of America, 31(2), pp. 163-176.

Stoer, J. and Bulirsch, R., 1992, *Introduction to Numerical Analysis, 2nd Ed.*, Springer-Verlag.

Stroud, A. H. and Secrest, Don., 1966, Gaussian Quadrature Formulas. Prentice-Hall.

Tanner, R., 2000, *Engineering Rheology, 2nd Ed*. Oxford University Press.

Tanveer, S. and Vasconcelos, G.L., 1995, "Time-evolving bubbles in two-dimensional Stokes flow," Journal of Fluid Mechanics, 301, pp 325-344.

Tremblay, B., 1991, "Sharkskin defects of polymer melts: The role of cohesion and adhesion," Journal of Rheology, 35(6), pp. 985-998.

Trevena, D., 1986, "Theoretical Values for the Tensile Strength of Certain Liquids," Journal of Physics D: Applied Physics, 8, pp. L144-L147.

Uijttewaal, W.S.J., Nijhof E. and Heethaar, R.M., 1993, "Droplet migration, deformation and orientation in the presence of a plane wall: A numerical study compared with analytical theories," Physics of Fluids A, 5, pp. 819-825.

Vinogradov, G.V., 1967, "Wall Slippage and Elastic Turbulence of Polymers in the Rubbery State," Rheologica Acta, 7, pp. 243-254.

Vinogradov, G.V., 1975, "Viscoelasticity and fracture phenomenon in uniaxial extension of high-molecular polymers," Rheologica Acta, 14, pp 942-954.

Vinogradov, G.V., Protasov, V.P. and Dreval, V.E., 1984, "The rheological behavior of flexible-chain polymers in the region of high shear rates and stresses, the critical process of spurting, and supercritical conditions of their movement at $T>T_g$," Rheologica Acta, 23, pp. 46-61.

Washio, S., Takahashi, S., Uda, Y. and Sunahara, T., 2001, "Study on Cavitation Inception in Hydraulic Oil Flow Through a Long Two-Dimensional Constriction," Proceedings of the Institution of Mechanical Engineers, 215 Part J, pp. 373-386.

Winterton, R.H.S., 1972, "Sizes of bubbles produced by dissolved gas coming out of solution on the walls of pipes in flowing systems," Chemical Engineering Science, 27, pp. 1223-1230.

Yasutomi, S., Bair, S. and Winer W., 1984, "An Application of a Free Volume Model to Lubricant Rheology," ASME Journal of Tribology, 106, pp. 291-303

Young, F. R., 1999, *Cavitation*, Imperial College Press.

Wagner, M.H, 1977, "Prediction of primary normal stress difference from shear viscosity data using a single integral constitutive equation," Rheologica Acta, 16, pp. 43-50.